New lab-on-a-chip strategies for enantio-selective and non-diffusion-limited biosensing

Jose García Guirado

Supervisor: Prof. Romain Quidant

Plasmon Nano-Optics group

This dissertation is submitted for the degree of
Philosophy Doctor

UPC-PMT, Castelldefels October 2018

To my parents.

Declaration

I hereby declare that except where specific reference is made to the work of others, the contents of this dissertation are original and have not been submitted in whole or in part for consideration for any other degree or qualification in this, or any other university. This dissertation is my own work and contains nothing which is the outcome of work done in collaboration with others, except as specified in the text and Acknowledgements. Chapters 3 and 5 are based on papers in which I am the first author. The former is based on "Enantiomer-selective molecular sensing using racemic nanoplasmonic arrays" published in ACS NanoLetters and the other is based on "Overcoming diffusion-limited biosensing by electrothermoplasmonics" published in ACS Photonics.

Jose García Guirado
October 2018

Acknowledgements

I would like to acknowledge the people that have collaborated, helped or participated in my work or life during the years that I have been working in my PhD.

I want to thank my family, especially my parents, who have had to deal with me during many of these years and made my life easier.

I want to thank my friends, for being my friends and because they were able to see me whenever I had time.

I want to thank Mario Montes Usategi for being the first to trust me as a researcher and for motivating me to go towards the PhD. I also want to thank Artur Carnicer and Angel Dieguez for providing me with resources and participating in my development as experimentalist during my Physics and Engineering degrees. (This is pre-PhD but I thought was important)

I want to give aspecial thanks to Romain Quidant as my thesis supervisor and for being such a nice person. I think he is a very trusting and tolerant person that always stays positive and nicely pushes you towards the goal. He has always given me his support and provided me with his expertise in all the work that I am presenting in this thesis. Romain is also one of the hardest working people that I know, and this inspires me.

I also want to thank Pau Turon from B.Braun Surgical S.A. who initially promoted the chiral project.

I want to especially thank Mikael Svedendahl as a nice collaborator. Together Mikael and I tackled the chirality problem in the last years. Despite many long discussions that ended up in terrible headaches, we finally managed to move the necessary step forward to make the project work. The COMSOL simulations and artwork in chapter 3 and appendix A1 are his work.

I also want to thank Joaquim Puigdollers for collaborating with us in the sample fabrication of chapter 3, and for always willing to discuss what is going on with the experiments.

I want to thank Raul Rica for being a nice collaborator, with whom we developed the concept of electrothermoplasmonic biosensing , and who was committed from the beginning until the publication of work shown in chapter 5. I also want to thank Emilio Ruiz-Reina who collaborated in the work related to chapter 5 and who is the author of COMSOL simulations.

I want to thank Jaime Ortega for always willing to help in the lab or discuss whatever. He has been very helpful during the writing of the electrothermoplasmonic paper. He made the image processing for particle tracking of the mentioned paper.

I want to thank Jan Renger, Srdjan Acimovic, Mark Kreuzer and Johann Berthelot, former postdocs in the group, for helping with my integration into the group and for the many valuable scientific discussions. A special mention goes to Jan, who showed me optics and nanofabrication, and to Srdjan who showed me microfabrication. From Johann I have learned how to be very hard working and lots of optics' lab stuff.

I would also like to thank Esteban Bermudez because he was my office mate most of the time and because he still continues to answer almost all my messages. He is also always willing to discuss everything.

I also want to thank Ozlem Yavas because she made me test my patience and tolerance and certainly made them to grow, although in detriment of rigour and accuracy.

I thank Ignacio de Miguel for always helping if he could and for always being happy. I thank Luis Miguel Fidalgo because he is a very motivating and rigorous person who cares about what he does. I also thank Vanesa Sanz, who developed the biochemistry protocols and is a hard working person. And I also thank Judith Medina, a former Master student, who participated in the preliminary electrothermoplasmonics experiments by recording the videos, which frames are shown in chapter 5 and appendix A2.

I also want to thank the rest of the current and former Plasmon Nano-Optics group members for sharing discussions and time together. I want to thank the technicians from the nano-fabrication-lab and the post-processing-lab, Javi Luis, Cristina, Johann Osmond, and Vittoria Finazzi, especially the latter two for their valuable help in some fabrication processes.

I also want to thank the ICFO administration departments: human resources, maintenance, logistics, purchasing and frontdesk, for making things easy. I want to acknowledge the electronic and mechanical workshops, for working hard and completing my requests on time.

Additionally, I want to thank Gavin Lucas and Thepapermill team for helping me polish the thesis.

Finally, I want to thank all the people that I may have forgotten to include that also helped me in some way or another during this time.

I am super happy to write this.

Abstract

The race for fast and small that drives nowadays society has also reached the field of biosensing. Looking for efficient and cost effective biosensors for applications including screening and treatment monitoring, biomolecular engineering, drug design and food industry; plasmonics and microfluidics technologies have synergistically grown to offer the most attractive solutions. The recent progress in nano-optics has paved the route toward the development of highly sensitive and label-free optical transducers using the localized surface plasmon resonance (LSPR). Additionally, LSPR offer high-end miniaturization and high degree of tunability of both sensors' spatial and spectral responses. These unique properties have recently been interfaced with microfluidics towards lab-on-a-chip (LOC) functional platforms which offer reduced sample volumes and multi-tasking operations on a single chip.

Combining nano-optics, microfluidics and biochemical sensing makes this PhD project highly multidisciplinary. This blend aims at pushing the limits of LSPR sensing by addressing two significant problems in the biosensing community.

On one hand, we went through chiral plasmonic sensing. Chiral molecules exhibit signatures in the ultraviolet frequency region. They are typically characterized by circular dichroism (CD), which suffers of low sensitivity and the need of big sample volumes and concentrations. Plasmonic nanostructures have the potential to enhance the sensitivity of chiral detection and translate the molecular signatures to the visible spectral range. However, to date, it remains unclear which properties plasmonic sensors should exhibit to maximize this effect and apply it to reliable enantiomer discrimination. As a consequence, a collection of results of difficult interpretation

and cross comparison can be found in the literature. Here, we bring further insight into this complex problem and present a chiral plasmonic sensor composed of a racemic mixture of gammadions that enables us to directly differentiate enantiomers. We also present a plasmo-fluidic sensing platform, which allows the systematic study of chiral biomolecules by enabling multiple sensing assays on a single chip.

On the other hand, we addressed one of the major challenges of plasmonic sensing in microfluidics environments; the transport of the analyte to the sensor surface, which due to the laminar flow that rules in micro-channels, is limited by Brownian diffusion. Hence, dictates the total duration of the sensing assay. Here, we use the electrothermoplasmonic (ETP) effect to overcome this limit through opto-electrical fluid convective flow generation. To this end, we designed a LSPR sensing chip that integrates ETP operation into state-of-the-art microfluidics. Our results demonstrate that ETP-LSPR has improved performances over standard LSPR.

Table of contents

List of figures

List of tables

Introduction

Abstract. This thesis focuses on novel plasmonic sensing schemes that combine nano-optics, microfluidics technology and surface chemistry, with a special emphasis on enantio-selective biosensing. I also present a study aimed at improving biosensing performance by overcoming diffusion-limited transport in microfluidics-channels. In this introductory chapter, I will introduce the background and the justification for our work and describe the structure of the manuscript.

The race towards "being faster, getting smaller" that currently pervades our society has also reached the biosensing community. There is an ongoing search for efficient, cost effective technologies using biosensors because of their potential applications in several fields, including clinical diagnosis, biomolecular engineering, drug design, the food industry, and point-of-care healthcare devices. In this context, plasmonics and microfluidics technologies have grown together in synergy to offer the most attractive solutions.

A biosensor is a device that comprises a biological recognition layer and a physical transducer that can translate biochemical interactions into quantifiable signals. Recent progress in plasmonic sensors, -including a high sensitivity and label-free detection scheme within an optical readout- has made them very attractive for the bio-sensing community. In particular, plasmonic sensors based on localised surface plasmon resonances (LSPR) offer high-end miniaturization and are highly tuneable in their spectral response, which ranges from the visible range to the near-infrared spectral range. These outstanding properties of plasmonics, in combination with a

microfluidic interface -in what is known as lab-on-a-chip (LOC) technology- offer excellent functionality while requiring lower sample volumes and offering multi-task operations in a single chip. Based on polydimethylsiloxane (PDMS), microfluidic technology offers miniaturization for high throughput assays. The existence of well-established surface chemistry for gold, as well as its higher chemical stability than silver, has made gold the preferred plasmonic material, thus conferring an additional target selectivity property for LSPR systems. Researchers have been testing these technologies since the first plasmo-fluidic integration was achieved, giving rise to rapid progress and ramification from novel to enriched biosensing scenarios, such as droplet microfluidics, the photothermal effect, plasmo-fluidic trapping or chemical synthesis.

In recent years, the plasmonics field has developed an interest in chirality as part of its search for a candidate to overcome classical sensing limitations. Chirality -a symmetry property that measures the similarity between mirror images of an object- is a property of the essential molecular building blocks for life, such as amino acids, sugars or nucleotides. Single-handedness of naturally-occurring molecules continues to be one of the biggest mysteries in science. In the middle of the last century, the subject gained special attention following the discovery, in drug synthesis processes, of enantiomer-related toxicity (an enantiomer, in terms of chirality, is the counterpart of a chiral molecule). Molecular enantiomers are indistinguishable to most currently available molecular characterization techniques, but they do show slightly different sensitivity to handedness of circularly polarized (CP) light. Circular Dichroism (CD), the differential absorption of left and right CP light, is the most common technique used to distinguish between chiral molecules, but due to the low magnitude of the effect, large sample volumes and high concentrations are required. Chiro-plasmonic research has devoted considerable effort to understanding chiral phenomena by manufacturing plasmonic structures that mimic molecular chirality. Such structures are built using a variety of techniques, ranging from top-down fabrications to bottom-up syntheses. The ultimate goal is to develop an enhanced chiral discrimination technique. Despite the colourful results of chiro-plasmonic research, there is no consensus in the community regarding the most appropriate experimental biosensing procedures. Consequently, a collection of results have been

published that are hard to interpret and even harder to compare. One of the most controversial issues involves deciding whether chiral sensors are suitable for chiral detection, or if achiral sensors should be used. Another issue in such experiments is the use of more massive but deficient molecular models (molecules lacking a mirror image) to mitigate the low signal of truly chiral molecular models. The major drawback of such systems is that it is impossible to validate the chiral origin of measurements. In this work, we propose a sensing platform based on a plasmo-fluidic device, along with experimental protocols that facilitate the systematic study of sensing biomolecules using plasmonics structures. We also designed a special type of sensor that merges the good properties of chiral and achiral sensors, facilitating enantiomer discrimination.

To take maximum advantage of LSPR sensing in microfluidics channels, in addition to our chirality experiments, we have developed and tested a novel three-layer chip architecture and experimental platform that merges electrothermoplasmonics (ETP) and microfluidics for biosensing applications. One of the major challenges of plasmonic sensing in microfluidics environments is the delivery of molecules to the sensor. Because of the highly laminar flow that occurs in micro-channels, diffusion dynamics limits the transport of molecules in the transverse direction (towards the wall, where sensors are typically located). Recently, the ETP effect has been used to improve the span and speed of plasmon-assisted particle trapping. The combination of a thermal gradient generated by laser-heating the plasmonic structures and two plano-parallel electrodes driven by an AC electric field can be used to generate vortices within the micro-channel. These vortices can modify flow dynamics, thus allowing faster transportation of molecules towards the sensors.

This PhD project is an example of highly multidisciplinary research project, in which different scientific disciplines are combined to tackle a complex problem and/or to develop new applications. While all fields involved are mature in their own right, combining them has represented a very challenging task, both technically and in terms of language and communication.

The current PhD project tackles the question of understanding plasmonic sensing systems in order to improve enantio-selective biosensing. We progressively explored

different techniques to study the interaction between nanoparticles and molecules from evaporated coatings to microfluidics solutions. We also analysed several ways to transduce optical signals into molecular signatures. Additionally, the issue of diffusion-limited transport in micro-channels is addressed by using the electrothermoplasmonics effect. Such a transversal issue is intrinsically interesting for improving any microfluidics plasmon-based sensing system.

Chapter 1 introduces the main concepts involved in the present work. Basic aspects of plasmonics are introduced, mostly focused on LSPR and its sensing applications, followed by the fundamentals of microfluidics as applied to a lab-on-a-chip system. I then provide a brief summary of the main surface chemistry methods used in the project, and introduce chirality and circular dichroism, as well as the electrothermoplasmonic effect.

Chapter 2 describes the main experimental techniques used in manufacturing and optical interrogation of the sensors. The overall experimental flow is presented, along with a summary of the cleanroom and surface chemistry protocols. In addition, the home-made experimental setups for CD and ETP-enhanced LSPR are presented.

Chapter 3 focuses on “enantiomer-selective molecular sensing using racemic nanoplasmonic arrays”. In this study, I present the first experimental application and show enantioselective detection using gammadion plasmonic arrays distributed in a racemic arrangement (50% of each type of handedness). By doing so, we isolate the weak chiral signal from the analyte by suppressing the strong CD of the sensors.

Chapter 4 introduces the concept of chiral sensing in a microfluidic environment. We explore the effects of annealing to unprotected gold nano-structures, and the consequences for this kind of experiments. We propose to tackle this issue by using sensor functionalization and a more sophisticated surface chemistry protocol. We were ultimately able to discriminate enantiomers under flowing conditions by using racemic gammadion sensors.

Chapter 5 is focuses on “overcoming diffusion-limited biosensing by electrothermoplasmonics”. This work presents the experimental generation of an LSPR mi-

crofluidic system with ETP integration that overcomes diffusion-limited transport in micro-channels. The new system shows faster sensing dynamics than those of classical diffusion limited sensing.

1

Scientific background

Abstract. In this chapter I will introduce the foundations of each of the concepts and fields involved in my PhD project. I will start with plasmonics, and introduce simple concepts and models to help understand localised surface plasmon resonances (LSPR) and how these can be used for sensing applications. I will then introduce key concepts in microfluidics, focusing on their application to sensing LSPR systems. Next, I will briefly explain the main surface chemistry protocols I have used to make the sensors functional. I will continue with an introduction to chirality and circular dichroism (CD). Finally, I will introduce the concept of electrothermoplasmonics (ETP), and discuss how it could be used to overcome the molecular diffusion limit in integrated biosensors.

1.1 LSPR sensors

Plasmons are free electron oscillations within a metal. They can be pictured as mechanical oscillations of the electron gas in the presence of an external electric field that pushes electrons away from their ionic cores. Plasmons can be excited either in bulk material using light (volume plasmons), or superficially in what is called surface

plasmon polariton (SPP), a hybrid light-electron wave that can propagate over the metal's surface. Special types of plasmons are generated when the size of the metallic particle is similar to the wavelength of the excitation light. In such a case, electrons that were initially pushed away remain confined in the boundaries of the particle, and are known as localized surface plasmons (LSP). Surface plasmon excitation requires specific light-matching conditions for the plasmon to generate and propagate. However, LSP resonances (LSPR) can be excited directly, in a similar fashion to that of dipoles in a dielectric material. When the size of the particle is smaller than the wavelength, the electron cloud is shifted away from its neutral position by the light's electric field, thus creating opposed charged areas: a dipole (see figure 1.1a).

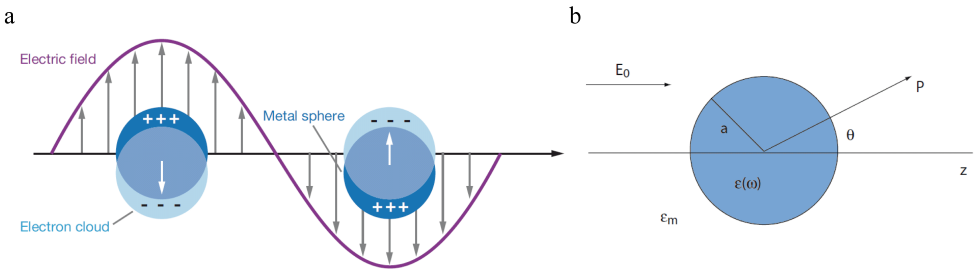

Fig. 1.1 a) Schematic illustration of a localized surface plasmon in metal particles (reprinted from K.Willets et al[1]). b) Sketch of a metallic sphere placed into an electrostatic field (reprinted from S.A.Maier[2]).

To develop further insight into the process, we can study a simple case: a sphere under the influence of an electric field. A simple model geometry depiction of the system (see figure 1.1b) would include a homogeneous, isotropic sphere of radius a and dielectric constant $\varepsilon = \varepsilon(w)$, located in a uniform static electric field $E = E_0 z$, surrounded by an isotropic and non-absorbing medium with dielectric constant ε_m. The electric field distribution inside and outside the sphere can be calculated as[2, 3] follows:

$$E_{in} = \frac{3\varepsilon_m}{\varepsilon + 2\varepsilon_m} E_0 \tag{1.1}$$

$$E_{out} = E_0 + \frac{3n(n \cdot p) - p}{4\pi\varepsilon_0\varepsilon_m} \frac{1}{r^3} \tag{1.2}$$

where n represents the unit vector pointing to point P, r the distance to the centre of the sphere and $p = \varepsilon_0 \varepsilon_m \alpha E_0$ the dipole moment of the particle. With α as the polarizability, the following equation may be applied:

$$\alpha = 4\pi a^3 \frac{\varepsilon - \varepsilon_m}{\varepsilon + 2\varepsilon_m} \tag{1.3}$$

By doing so, we can see that the external electric field is distorted by the action of the dipole, with polarizability showing a resonant behaviour when $\varepsilon + 2\varepsilon_m$ reaches a minimum value. This result indicates how resonance depends on environmental changes. If we now consider the time-varying dependence and plane wave illumination, $E(r,t) = E_0 e^{-iwt}$, of the external electric field, where w represents the angular frequency, we can see that an oscillating dipole will be induced, $p(t) = \varepsilon_0 \varepsilon_m \alpha E_0 e^{-iwt}$, in which radiation leads to absorption and scattering of the plane wave. Their cross-sections can be calculated and written as follows[4]:

$$C_{abs} = k\,\mathrm{Im}\left[\alpha\right] = 4\pi k a^3 \left| \frac{\varepsilon - \varepsilon_m}{\varepsilon + 2\varepsilon_m} \right| \tag{1.4}$$

$$C_{sca} = \frac{k4}{6\pi} \left|\alpha^2\right| = \frac{8\pi}{3} k4a^6 \left| \frac{\varepsilon - \varepsilon_m}{\varepsilon + 2\varepsilon_m} \right|^2 \tag{1.5}$$

where $k = 2\pi/\lambda$ (λ = wavelength). We can see that for small particles (where $a << lambda$), the efficiency of absorption increases with a^3 and predominates over scattering efficiency, which increases with a^6. Due to the rapid increase in scattering cross-section, picking up a small object from a background of several larger ones will be very difficult. These results also show that absorption and scattering, and thus extinction ($C_{ext} = C_{abs} + C_{sca}$), are resonant at the particle dipole resonance, and therefore are also dependent on the dielectric properties of the medium. This is an important result in terms of optics, since noble metals like gold and silver exhibit their resonances in the visible range. A sensing scheme could be devised in which resonance is defined by sensor morphology and material properties, which will change according to environmental variations.

This is a simple model approach, but more complex models, beyond spherical particle shapes, have been developed to explain multipolar resonances and polarization effects, among others[5, 6, 2]. Nevertheless, while such models provide good approaches to help understand the phenomena involved, in practice they are too simplistic to describe real sensing systems, which typically do not fulfil the constraints of these models. Numerical methods are commonly used to calculate the optical properties of the plasmonic particles, typically by looking for high field enhancements in the near field and tailoring their far-field[7]. Another option is to parametrically fabricate and experimentally measure their optical properties and sensing capabilities. Figure 1.2 shows the extinction of nano-rods of different lengths and gammadions of different sizes, both distributed within an array. Depending on a given nano-particle geometry, the corresponding resonance profile could be associated with fundamental modes that are mostly related to particle shape. In addition, the interaction between close particles in more complex systems could result in near field interactions[8, 9], and organized arrangements of particles could result in far-field effects[10].

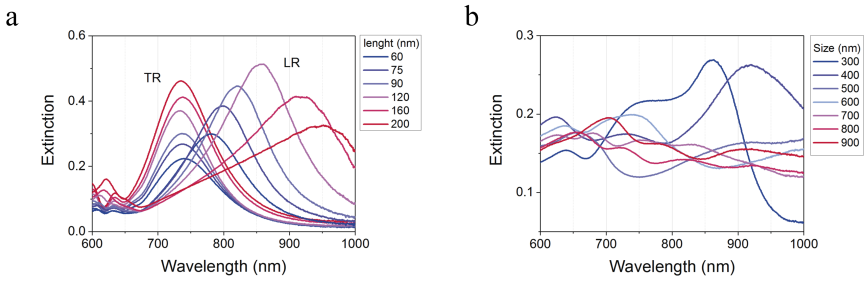

Fig. 1.2 Experimental extinction spectra of different plasmonic geometries. a) Gold nano-rods of different lengths and fixed width and height. b) Gold gammadions of different size with scaled periodicity and fixed height.

An LSPR sensing system can also be optimized through iterative experimental measurements of practical parameters and figures of merit[11]. Refractive index sensitivity is a widely used parameter in LSPR systems:

$$m = \frac{\Delta\lambda}{\Delta n} \tag{1.6}$$

where $\Delta\lambda$ represents the shift in peak wavelength due to Δn variation in the bulk refractive index (environment surrounding the nano-particle). Bio-sensing experiments not only involve bulk refractive index measurements, but also measurements of molecule adsorption on the nano-sensor's surface. If the bulk refractive index sensitivity is known, the peak shift can be calculated as follows[12]:

$$\Delta\lambda = m\Delta n\left(1 - e^{\frac{-2d}{l_d}}\right) \tag{1.7}$$

where d represents the thickness of the molecular layer and l_d stands for the electromagnetic-field-decay length[13]. In this case, Δn represents the change in refractive index induced by the adsorbed molecule.

These parameters provide a good way to optimize LSPR sensing. In general, when analysing data a resonance red shift is assumed to originate as a consequence of the increase in the bulk refractive index or as a consequence of molecule adsorption on the surface of plasmonic particles (or as a consequence of both). Conversely, a blue shift will be regarded as a reduction of the refractive index, or as desorption of molecules from the surface of the sensor.

Figure 1.3 shows a typical LRSR analysis curve. The position of the peak (shift) is monitored over time as changes in the sensor environment occur. Apart from peak shift, the peak centroid can be calculated in order to improve the signal-to-noise ratio[14]. The peak centroid may be calculated as follows:

$$\lambda_c = \frac{\int_{\lambda_1}^{\lambda_2}\left[E(\lambda) - E_b\right]\lambda\, d\lambda}{\int_{\lambda_1}^{\lambda_2}\left[E(\lambda) - E_b\right] d\lambda} \tag{1.8}$$

where $\lambda_2 - \lambda_1$ represents the span of calculation and E_b the extinction value matching $E_b = E(\lambda_2) = E(\lambda_1)$. However, using the centroid is advantageous in case of slightly noisy, well-behaved peaks. No real improvements (as compared to peak analysis) were found with peaks that were far from Lorentzian shape and had a significant noise level.

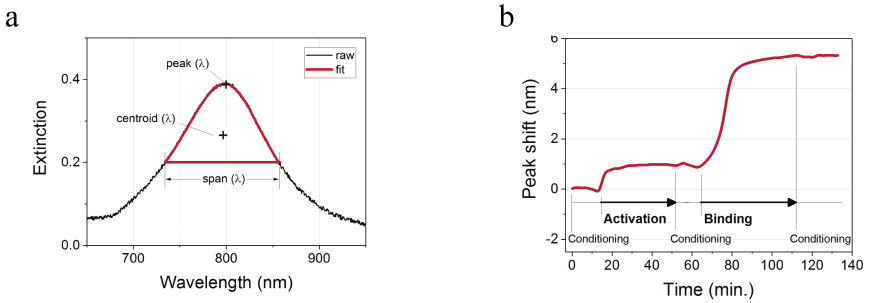

Fig. 1.3 Analysis of graphs obtained in LSPR sensing experiments. a) Fitting of the plasmonic resonance. The centroid is calculated for a given wavelength span. b) LSPR peak shift. The peak position in (a) is monitored over time during the successive steps of the sensing assay. In this specific example, a two-step detection scheme is shown: initially the sensor surface is activated so that the analyte/antibody may be captured; then, the analyte of interest is bound to the sensor surface. Conditioning includes minor preparation and washing steps.

In more complex sensing scenarios, several additional effects - such as chemical reactions between molecules and sensors, sensor annealing, heat, etc.[15–18] - could have different effects on plasmonic resonance, thus interfering with the sensing curve.

Overall, the following aspects need to be considered as a starting point when designing plasmonic sensors:

- Higher field enhancements in sensing volume.
- Field enhancement decreases exponentially as the distance from the surface of the nanoparticle increases; therefore, detection should take place as close to the surface as possible.
- For a given structure shape, the longer the wavelength used, the larger the shift obtained.
- Peak position and width can be engineered by selecting the material and tuning the size and shape of the particles.

1.2 Micro-fluidics

Microfluidics is a technology that allows us to control liquids in channels with transverse dimensions ranging from a few hundred microns to a few microns. At this scale, fluid properties that are commonly accepted at the macro level no longer apply. Laminar flow governs fluid dynamics in the micro-channels, and the interaction between the fluid and the substrate surface becomes relevant. While in turbulent flow, fluid elements can chaotically change their speed and direction along the overall fluid motion, laminar flow motion occurs in ordered, parallel layers of well-defined velocities (see Figure 1.4). The fluids's distribution across the channel exhibits the characteristic profile features (parabolic) related to Poseuille flow. An important consequence of laminar flow conditions is that no perpendicular fluid motion occurs[19].

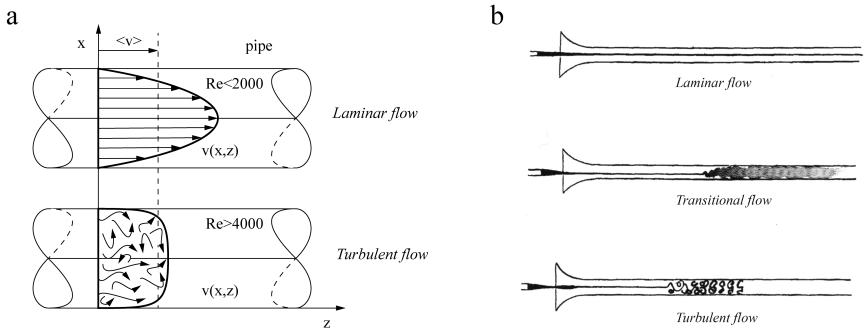

Fig. 1.4 a) Flow speed profile $v(x,z)$ inside a macroscopic pipe under laminar (top) and turbulent (bottom) flow conditions. b) Laminar (top), transitional (middle) and turbulent flow (bottom) representations in a pipe (reprinted from O. Reynolds[20]).

Fluid dynamics can be modelled using Navier-Stokes equations; however, analytical flow calculation's for complex channel shapes is not trivial. Practical parameters describing the fluid's properties in specific cases are commonly used for Newtonian fluids; for example, the Reynolds number defines the degree of laminarity or turbulence of the fluid flow inside a microchannel, which can be derived as follows[21]:

$$Re = \frac{inertial\,forces}{viscous\,forces} = \frac{\rho v^2 D_h}{\mu v} = \frac{\rho v D_h}{\mu} \tag{1.9}$$

where ρ represents fluid density, v its velocity, μ its viscosity, $D_h = 4A/P_w$ the hydraulic diameter of the micro-channel (with A being its cross-sectional area and P_w the wetted perimeter). A turbulent regime is considered for Reynolds numbers above 4000, and a laminar regime is considered for values below 2000; values 2000<Re<4000 are considered to be in a transition region. However, this transition has been found to shift towards lower numbers in micro-channels. In fact, turbulence can be found at Re>2000, while laminarity would be ensured below 100 for pipe diameters about 100 μm or smaller[22]. Nevertheless, such values[23] would also be slightly different in different channel geometries.

1.2.1 Molecular transport in micro-channels

Molecular transport in micro-channels is an important issue in sensing-related matters. In this regard, the Péclet number is the ratio between diffusion and advection transport times. This number compares the transport rate due to bulk movement and the mass diffusivity due to molecule concentration gradients. It can be expressed as follows[21]:

$$Pe = \frac{t_{diffusion}}{t_{advection}} = \frac{L^2}{Dv}\frac{v}{L} = \frac{Lv}{D} \tag{1.10}$$

where L represents the characteristic length at which transport will be compared, v the fluid velocity, and D the diffusion coefficient. If $Pe >> 1$, the transport will be dominated by advection; when $Pe << 1$, transport will be dominated by diffusion. Given that current conditions are laminar flow conditions, and because of the specific properties related to flow in a micro channel, a high velocity is expected along the channel, while none is expected towards the walls (where LSPR sensors are typically placed) Therefore, a large Péclet number is expected in a parallel direction to that of

the channels, while a small number is expected in a perpendicular direction to that of the channels. Hence, diffusion limits the transport of molecules towards the sensors.

For molecular sizes (subnanometric to a few nanometers), quite a uniform molecular concentration may be expected across the channel, tending to zero close to the walls[24, 25]. Molecular diffusion is predicted by Fick's first law as the flux of molecules $J = -DdC/dZ$ goes from high to low concentration[26]. Considering the concentration on the sensor surface to be zero at the beginning of the process, the sensor will quickly reach long transient to saturation regimes in very low concentration settings, since very few molecules would be expected in the surroundings of the sensors.

In terms of molecular transport, microfluidic systems have not yet reached optimal conditions because the constraints mentioned above limit speed detection and the minimum detectable quantity of analyte that can be measured by LSPR sensors in microfluidic channels.

1.2.2 Impedance in microfluidics networks

Microfluidic networks -in particular flow rate through channels, in terms of splits, joins and overall size- show analogous behaviour to that of electrical circuits. The hydraulic resistance, or impedance, experienced by a liquid in passing through the channels follows Hagen-Poiseuille's law, which is similar to Ohm's law (describing electric current passing through resistive elements). The above analogy is shown in Figure 1.5: pressure (P), flow rate (Q) and hydraulic resistance (R_h) are equivalent to voltage (V), current (I) and electric resistance (R_e), respectively. Therefore, we must account for the length, dimensions, shape, joints and splits of the channels in the chip, as well as those in the tubing of the microfluidic setup.

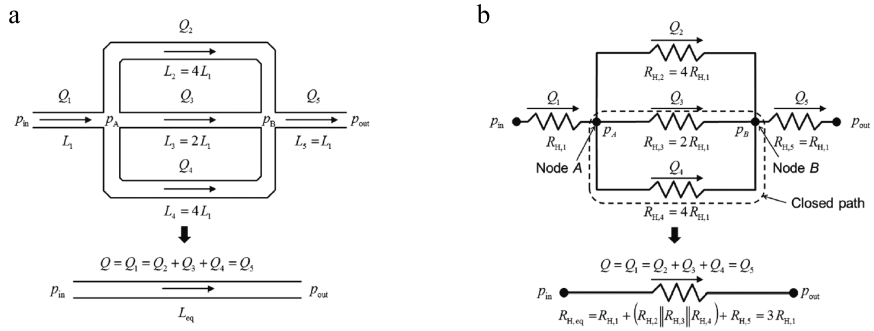

Fig. 1.5 Microfluidic-Electrical circuitry analogy. a) A simple microfluidic network connected with different channel lengths but with the same cross-sectional area and shape, and b) its equivalent electric circuit. Flow discharge (Q) is preserved in the closed path between PA and PB. An equivalent fluidic element can be calculated, as an equivalent resistor can be calculated between nodes A and B in the electrical analogy. (reprinted from K. W. Oh et al.[27])

1.2.3 Two-layer microfluidics

Apart from the design of flow channels, two-layer microfluidics implements flow regulation through a control layer; this makes the flow channels collapse into the flow layer (micro valve action), thus preventing fluid transfer[28]. Microfluidic chips are built using PDMS, a flexible and transparent polymer that is ideal for opto-fluidics and compatible with LSPR sensors. Sensors can be placed throughout the chip, and may be given different targets. Figure 1.6 shows a typical geometry of a LSPR microfluidics chip.

These are simple approximations to microfluidic chip design. Further needs in terms of sensing, sorting and reactor design push researchers into tackling challenging problems with non-trivial solutions, such as molecular transport inside microfluidic channels, liquid mixing, and the addition of thermal and electrical effects, to name a few.

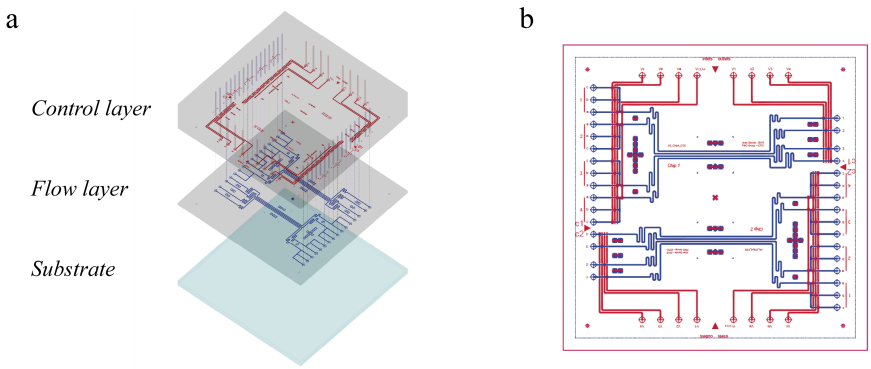

Fig. 1.6 Microfluidic chip design for 8 individual experiments. a) Layer composition of the microfluidic chip. b) Top view of the microfluidic network. The red lines represent the channels through the control layer, while the blue lines represent the channels through the flow layer.

1.3 Surface chemistry

Surface science studies the chemical and physical phenomena that take place at the interface between two different phases, and surface chemistry studies chemical changes at these interfaces. Molecule adsorption at a surface is a fundamental issue in surface chemistry, since it is a prerequisite for any surface-mediated chemical process. There are two principal modes of adsorption, physisorption and chemisorption, depending on whether the adsorbate and the adsorbent are held together by Van der Waal forces only (physisorption) or by a chemical bond (chemisorption)[29]. This section will focus on several concepts involving chemisorption of molecules on gold nanoparticles and PDMS oxidation.

Research into the surface chemistry of gold nano-particle develops techniques to modify their surface with functional purposes. I fabricated gold nano-particles by electron beam lithography, and studied how to link the corresponding molecule of interest to the particles. I mainly used two chemical reactions: (i) the adsorption of molecules containing thiol groups (HS), whereby a covalent $S-Au$ bond was created, leading to the formation of self-assembly monolayers (SAM) on gold (which could be used either with functional purposes or for direct detection of the molecule

of interest); (ii) I modified a functional carboxylic group (*COOH*) on the SAM using sulfo-NHS carbodiimide cross-linking to attach amine groups in my molecules of interest to the SAM trough amide bonds . Figure 1.7 shows the reaction schemes.

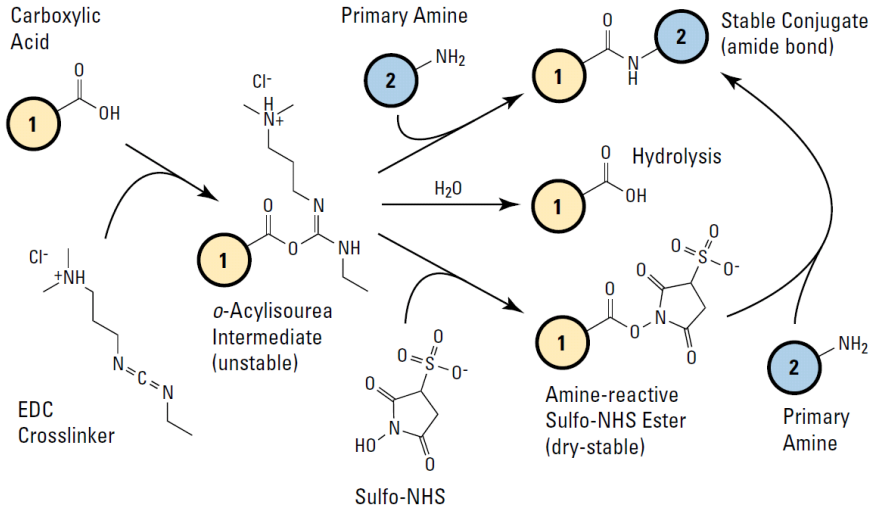

Fig. 1.7 Sulfo-NHS plus EDC (carbodiimide) cross-linking reaction scheme. The addition of Sulfo-NHS to EDC reactions (bottom-most pathway) increases the efficiency of Carboxyl-to-amine cross-linking. (reprinted from Thermoscientific[30])

Another common surface modification I used is PDMS oxidation. Methyl groups (CH_3) are oxidised to *OH* in the presence of an Oxygen plasma atmosphere or UV Ozone. After placing two oxidised surfaces together, the *OH* group reacts by forming permanent covalent oxygen bounds within a few minutes, thus sealing the PDMS layer. The same process can be used to bind PDMS to glass, (bonds may also be created by exposing glass to Oxygen plasma, but higher exposure times are required when working with glass). A gentle thermal process (1h at 80°*C*) helps settle the reaction. However, if gold sensors are functionalized with an organic SAM, the substrate cannot be exposed to plasma; therefore, weaker PDMS-glass bonds would be expected. Figure 1.8 shows the corresponding reaction schemes.

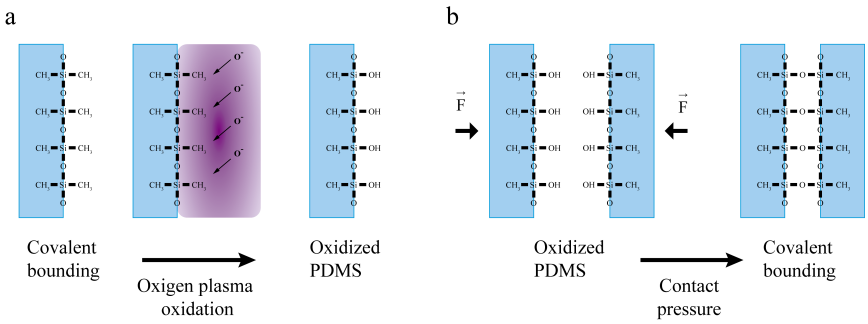

Fig. 1.8 PDMS binding schemes. a) Oxidation of PDMS surface by plasma oxygen. Oxygen ions react with methyl groups in order to create OH groups on the surface. b) Assembly of two PDMS layers. When placed in contact, OH groups reach to form a covalent $Si-O-Si$ bond.

1.4 Circular Dichroism

A state of circularly polarized light is achieved when a light beam propagates towards the z direction in such a way that the x and y direction components of the electric field oscillate with an equal magnitude and a $\pi/2$ phase difference (see Figure 1.9). An observer looking towards the source would see a helix rotating either left or right, depending on the sign of the phase difference. Electric fields rotating to the left will be called left circularly polarized (LCP), while those rotating to the right will be called right circularly polarized (RCP). Here, I used a "looking towards the source" convention, which is widely used in physics textbooks[31]; a "looking towards the receiver" convention is commonly used in engineering fields.

Circular dichroism (CD) represents the differential absorption of left- and right-circularly polarized light. It may be calculated as follows:

$$CD = A_{LCP} - A_{RCP} \tag{1.11}$$

This is the most widely used spectroscopy method for characterizing the chirality of molecules[33]. Enantiomers -molecules that are specular reflections of each other-

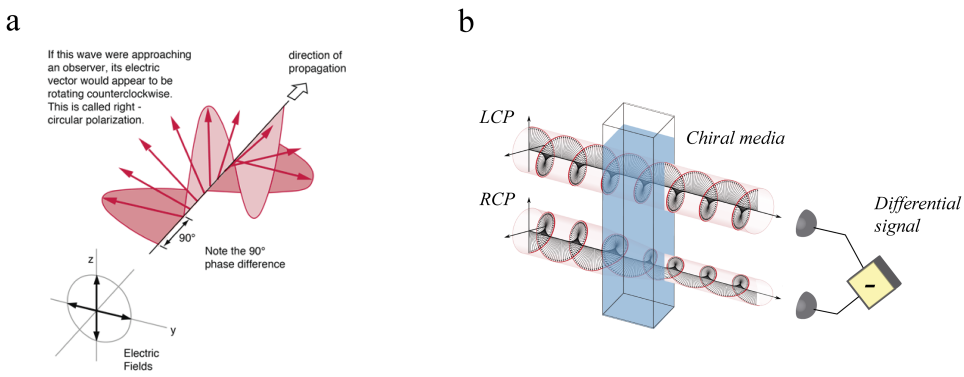

Fig. 1.9 a) Representation of circular polarization. An observer looking towards the source would see the electric field vector propagating as a helical shape rotating counter-clockwise, while in a fixed position the field will rotate clockwise (reprinted from Hyperphysics[32]). b) Circular Dichroism experimental scheme. Left circularly polarized (LCP) and right circularly polarized (RCP) beams are absorbed differently by chiral media; therefore, CD represents the differential signal for the relative signal of the two beams.

absorb both LCP and RCP, but while one species absorbs slightly more LCP, the other species absorbs slightly more RCP. This property is complementary, so their CD signals are of opposite sign, and the CD signal of their 50/50 mixture is zero. No signal would be obtained if we measure CD on a non-chiral molecule, or in a perfect mixture of two enantiomers (racemic mixture). Such CD features can mostly be detected within the UV range (see Figure 1.10c). Large molecules, such as proteins, could exhibit CD signals due to their secondary structure, but they lack enantiomer conformation. Chirality may also be characterized by other means, such as ORD (which measures the rotation of linear polarized light) and VCD, (which measures the dichroism of molecular vibration bonds); however, these methods often show poorer performance than that of CD[34, 35]. The figure 1.10 shows some examples of chiral molecular systems and CD.

Over the last decade, chiral plasmonic structures have been created (mainly in gold or silver) in order to mimic molecular properties in the visible-near infrared range. Such plasmonic structures are typically fabricated using lithography techniques, which allow good control of morphology. 2D structures with a chiroptical

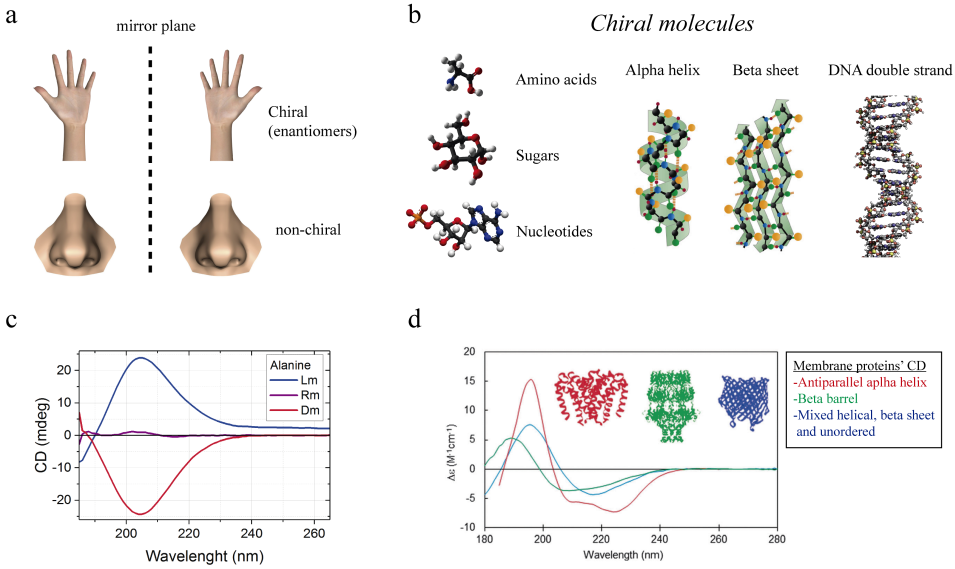

Fig. 1.10 a) Representation of chirality. Mirror images of a hand are chiral (and an enantiomer pair) since they cannot be brought to coincide. On the other hand, a nose is a non-chiral object, since the object and its mirror reflection may be superimposed. b) Chiral molecules. Amino acids, sugars and nucleotides are naturally-occurring chiral molecules, and they are the building blocks of proteins and DNA. Alpha-helixes and beta-sheets are secondary structures in proteins, and they possess chirality. The DNA double helix is another important chiral biostructure (reprinted form Wikipedia commons[36–39] and Dep. Bio. Penn State Uni.[40]). c) CD signal of alanine enantiomers (Lm and Dm) and that of their racemic mixture (Rm). Since L and D enantiomers are available, a mirrored CD can be measured, while proteins in d) would not have an opposite CD as they lack a mirror image (reprinted from A.J. Miles et al.[41]).

response are straightforward to manufacture, although complex 3D morphologies may also be obtained using lithography techniques[42, 43]. Figure 1.11a shows the CD response of a plasmonic structure with an enantiomer composition that has shifted from an entirely left-handed profile to an entirely right-handed one; in doing so, the racemic mixture was obtained, as shown by the CD profile gradually changing its sign through zero.

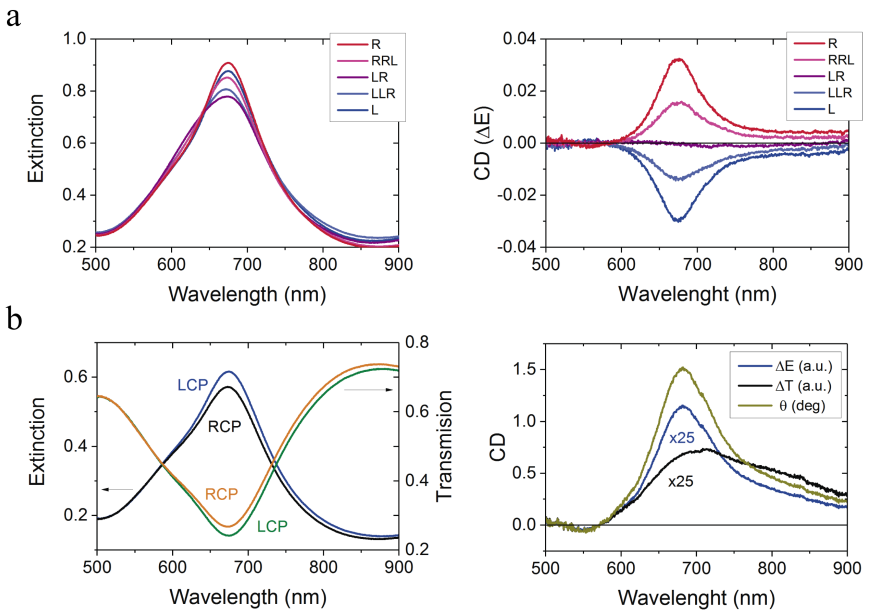

Fig. 1.11 a) Extinction (left) and CD (right) spectra of gammadion arrays with different handedness contribution in the unit cell. As the structure handedness shifts, the extinction spectra remain very similar, while CD flips its sign and "crosses" zero. b) Extinction and transmission spectra (left) for LCP and RCP light.

Although CD is defined by differential absorbance, different needs for comparison and quantification lead to the development of several units and transformations; hence, absorptivity, extinction coefficient or ellipticity are used instead of absorbance to analyse chiral media. These results can be retrieved from transmission measurements on isotropic chiral liquids; however, chiral plasmonic structures are usually anisotropic, so the symmetry of the system must be taken into account[44]. Commonly, results on different calculations may be found in the literature, including

differential absorbance, extinction, differential transmission or ellipticity (θ). They are defined as follows:

$$CD(\Delta E) = E_{LCP} - E_{RCP} = log_{10}\left(\frac{1-T_{LCP}}{1-T_{RCP}}\right) \tag{1.12}$$

$$CD(\Delta T) = T_{RCP} - T_{LCP} \tag{1.13}$$

$$\theta = atan\left(\frac{\sqrt{T_{RCP}} - \sqrt{T_{LCP}}}{\sqrt{T_{RCP}} + \sqrt{T_{LCP}}}\right) \tag{1.14}$$

Figure 1.11b shows different calculations for the same plasmonic system (all calculations are based on a transmission signal with its main feature around $675nm$). While they are not exhibit exact CD, they report the chiral information from the system, so for practical purposes it is advisable to use the more convenient calculation set for one's own system. Since I was searching for sharp peaks for a sensing system, ΔE was the best choice.

It is not straightforward to model chiral plasmonic systems for use as sensors for chiral molecules. When considering the polarizability of a sphere, a simple analytical shape (section 1.1), I mentioned that when the geometry changes (such as using nano-rods instead of a sphere), the resonance showed polarization-dependence effects. When considering a molecule composed of different atoms that have a complex 3D structure, a non-trivial problem arises, with subtle effects on polarization response. In addition, plasmonic particle-molecule interactions should also be considered.

In recent years, several approaches to this problem have been published[42]; however, it is still not clear what mechanisms are involved in the nanoparticle-molecule interactions, or what are the optimal parameters for enhancing sensing performance. Some authors claim that molecules induce CD on non-chiral plasmonic nano-structures through high E field interactions. Others consider chiral plasmonic nano-structures to have a CD that is sensitive to molecular chirality[45]. In these approaches, near-field distributions seem to have an important role; therefore, it is common to see numerical calculations on electric field and optical chirality enhancements, given by the following equation:

$$C = -\frac{\varepsilon_0 w}{2} Im\{E^* \cdot B\} \tag{1.15}$$

Figure 1.12 shows an example of the aforementioned sensing schemes, with chiral features emerged from plasmonic CD spectral differences or from molecular-induced CD.

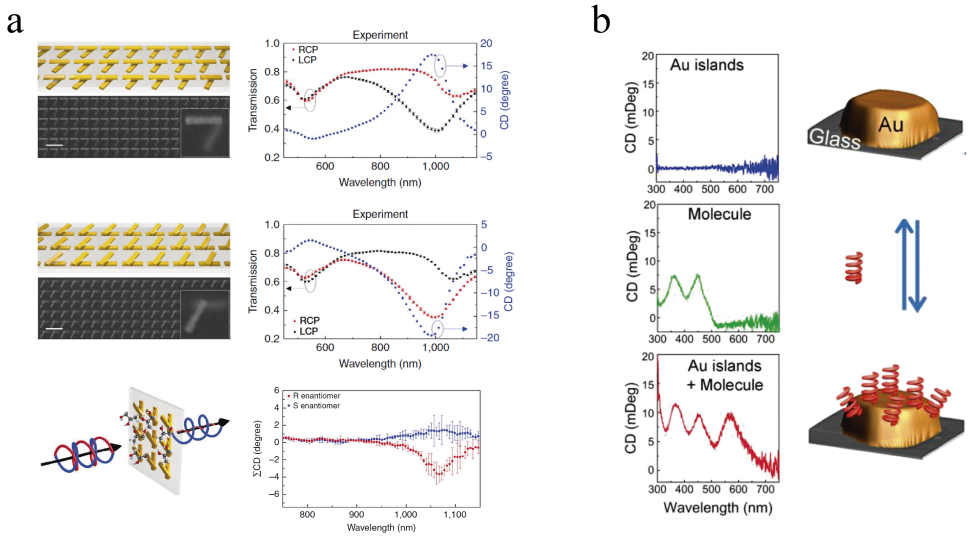

Fig. 1.12 Approaches to chiral plasmonic sensing. a) An experimental scheme in which chiral plasmonic sensors are sensitive to molecular media. The pseudo-symmetric spectra of plasmonic structures (top and middle) shows different sensing of propanediol enantiomers. After adding the opposite CD of plasmonic structures, the chiral discrimination signal appears (Zhao et al.[46]). b) An experimental scheme in which a non-chiral plasmonic sensor shows induced CD from a chiral molecule (reprinted from Maoz et al.[47]).

However, every solution has some drawbacks. Using chiral plasmonics requires non-obvious interpretations of the results, since plasmonic CD shadows the molecules' direct response. Moreover, the signals for non-chiral plasmonic structures are more challenging to measure. Also, the system's sensitivity seems to be dependent not only on sensor properties, but also on molecular properties and distribution, which makes the problem highly complex[48, 49].

Another important issue in the plasmonics chiral sensing community is the wide variety of molecular models used, and the lack of a good verification system. These issues often make it difficult to interpret the results, and lead to reproducibility problems, since to date there is not clear link between the phenomena observed in different experiments.

With such a variety of systems and non-linked results, it is not yet clear what is the best option for developing a robust chiral sensing system.

1.5 Electro-thermo Kinetics

Because of the laminar flow regime, it remains challenging to deliver molecules to sensors beyond diffusion-limited dynamics in microfluidics systems. Ideally, one would like to drag the molecules and place them on the sensors at a controlled rate, leading to a reaction-limited system. The electro-thermo-plasmonic (ETP) effect is an option that affords bulk movement inside the microfluidic channels by applying heat and electric fields under an external action. By doing so, the laminar flow regime would break into a controlled convective regime. Therefore, the molecules inside the media could be dragged toward the sensors if the flow is properly designed.

The physical principle is based on electro dynamic forces acting on a given liquid volume. A general expression for the resulting force can be summarized as follows[50]:

$$\mathbf{f}_e = \rho_q \mathbf{E} - \frac{1}{2}\mathbf{E}^2 \nabla \varepsilon + \frac{1}{2}\nabla \left(\rho_m \frac{\partial \varepsilon}{\partial \rho_m} \mathbf{E}^2 \right) \tag{1.16}$$

where ρ_q represents the charge density, ε stands for permittivity and ρ_m represents mass density. When an electric field is applied into a non-compressible liquid, the third term in this equation has no effect on the dynamics (it is a gradient of a scalar) and therefore can be ignored. The first and second terms represent Coulomb forces and dielectric forces, respectively. Eq.1.16 under the action of and *AC* field and

considering only the steady component, the formulation can be further developed to include temperature dependence of $\varepsilon(T)$ and conductivity $\sigma(T)$, as well as an *AC* field, thus reaching the time-averaged electro thermal force[50, 51]:

Eq.1.16 can be further developed to include temperature dependence of $\varepsilon(T)$ and conductivity $\sigma(T)$, as well as an *AC* field[50, 51], thus reaching the time-averaged electro thermal force:

$$\langle \mathbf{f}_{ethm} \rangle = \frac{1}{2} Re \left\{ \frac{\sigma\varepsilon(\alpha-\beta)}{\sigma+iw\varepsilon} (\nabla T \cdot \mathbf{E})\mathbf{E}^* - \frac{1}{2}\varepsilon\alpha|\mathbf{E}|^2\nabla T \right\} \tag{1.17}$$

where $\alpha = 1/\varepsilon(\partial\varepsilon/\partial T)$ and $\beta = 1/\sigma(\partial\sigma/\partial T)$. At high enough frequency , the second term of eq.1.17 dominates[50], hence the force applied to the liquid depends on the magnitude of the electric field E^2, the gradient of temperature ∇T, permittivity ε and the temperature dependence of permittivity α. To stay in the ETP dominat region we should be in the range $10kHz - 1MHz$[52, 53].

A promising setup has been proposed and demonstrated for enhanced particle manipulation based on the previous result[51]. The system configuration consists of a heat source to generate the temperature gradient and two parallel electrodes to close the micro-chamber and generate the electric field. In fact, the heat source is a plasmonic structure which is laser-excited at the resonant frequency (see Figure 1.13). Flow motion drags polystyrene particles towards the plasmonic structures faster and from considerably larger distances than those achieved with regular optical trapping. Thereafter, the particles remain trapped or are released, depending on external parameters.

Such a configuration may be adapted for LSPR microfluidics: a plasmonic structure could be optimized to efficiently act as a heat source and sensor; the flow vortexes in the microchannel would break the laminar flow regime into a turbulent flow regime, which would be beneficial for diffusion-limited sensing applications.

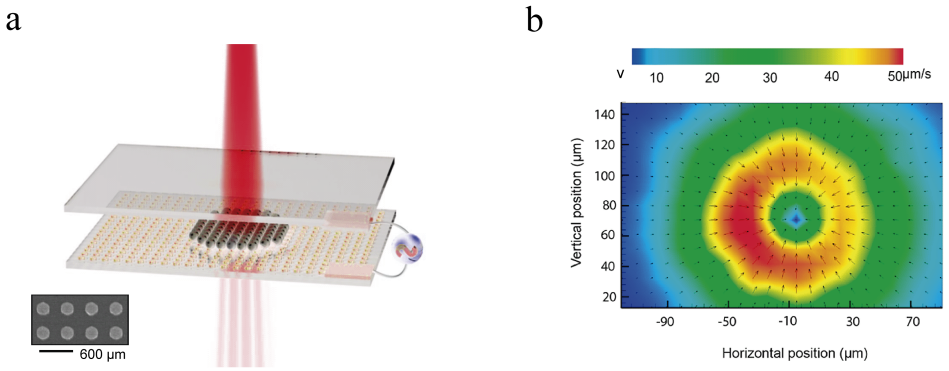

Fig. 1.13 ETP flow-based trapping setup implemented by J. Ndukaife et al. a) A schematic representation of the fluidic cell which contains the transparent electrodes, the nanoparticle array and the beads trapped by the laser action. The inset shows a SEM image of gold nanoparticles. b) Particle image velocimetry field representing the ETP flow in the fluidic cell ($9.8Vpp$ at $100KHz$ and $17mW$ of laser power were applied). (reprinted from J. Ndukaife et al.[51])

2

Experimental methods

Abstract. In this chapter I will review the techniques used to manufacture, characterize and prepare the samples for the various experiments. First, I will introduce the typical experimental flow I followed to manufacture plasmonic substrates and integrate them into the microfluidic environment. I will then introduce micro- and nano-fabrication, and surface chemistry. Next, I will present the experimental optical setups, which were designed and implemented from scratch. One was used to measure real time circular dichroism in a microfluidic environment. Another was used for microfluidic LSPR sensing and included an electrothermoplasmonic effect control.

2.1 Experimental flow

The typical overall methodology in LSPR sensing is as follows: (i) gold plasmonic sensors and microfluidic chips are manufactured; (ii) plasmonics sensors are conditioned for the experiment; (iii) the micro-fluidic chip and substrate with the plasmonic sensors are assembled; (iv) the experimental setting is prepared for the microfluidics experiment (many small steps are needed, ranging from micro-tube cutting to spectral pre-acquisition); (v) the full chip is mounted, aligned and connected; (vi)

bio-chemical samples are prepared and loaded onto the chip; (vii) measurements are performed and the resulting data are processed. Figure 2.1 depicts the typical fabrication steps and the overall experimental methodology.

The experimental flow is not as short and simple as it seems from Figure 2.1. When merging different disciplines in a given experiment, many issues can arise that are not apparent before the experiment is performed. In addition, working with merged systems makes it difficult to determine where problems might come from. Each and every possible source of error needs to be addressed separately, after which the complete 5-day process must be repeated to ensure the proper functioning of the experimental flow. Under perfect working conditions, an experiment would last approximately one week, depending on the number of chips needed. However, in practice it will likely take several months to debug the system of errors.

2.2 Nanofabrication of the plasmonic sensors

Nano-science is the study of objects with at least one of their dimensions in the 1-100 nm range. The composite word "nanofabrication" refers to the manufacturing techniques used to create nano-objects, and many processes are involved in creating a nano-object. Two main methodologies may be used, the "top-down" methodology and the "bottom-up" methodology[54], and I will focus on the former. Specifically, I will describe electron-beam-lithography[55], which is the most commonly used methodology and was originally developed for the computer silicon industry. Specifically, I used a negative lithography process, and this can be adapted to manufacture gold on plasmonic substrates. Figure 2.2 shows the nano-fabrication workflow.

2.2.1 Gold films

The typical plasmonic substrate used was composed of a $25x25x0.4mm^3$ volume of borosilicate glass (PGO MEMPAX) coated by evaporation (Lesker Lab18) with $2nm$

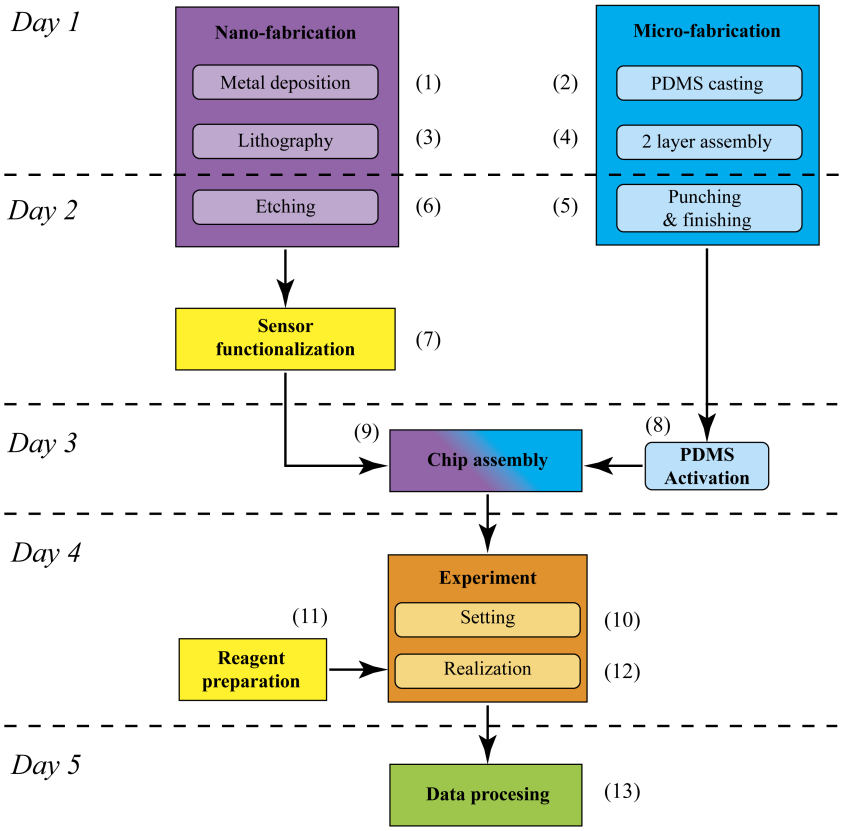

Fig. 2.1 Flow of a typical LSPR experiment. The numbers for the different steps of the process indicate sequence order (minor variations would be possible on day 1). Different disciplines are represented by different colours: nano-fabrication (purple), micro-fabrication (blue), chemistry (yellow), optics (orange) and computing (green).

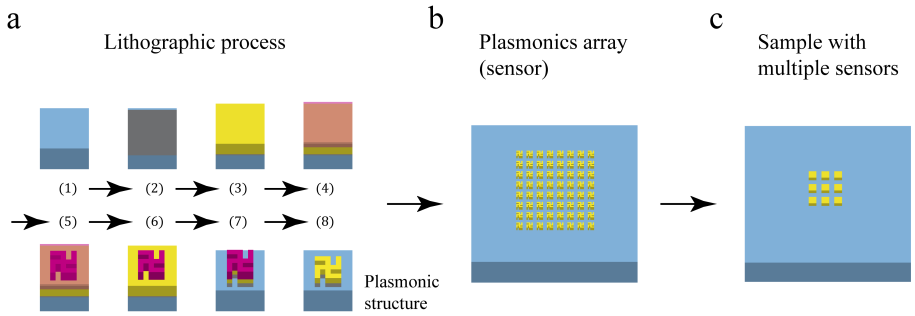

Fig. 2.2 Depiction of the nanofabrication flow. a) Negative lithography process steps; 1) substrate cleaning ; 2) evaporation of titanium layer; 3) gold evaporation; 4) resist coating, 5) e-beam exposure; 6) development; 7) dry etching; 8) resist removal. b) Sensor layout. c) Typical sample layout.

of titanium and 50nm of gold. Eventually, the thickness of the gold layer could be in the 40 to 100nm range.

The substrates are initially cleaned with soap + Deionized (DI) water, DI water, acetone and iso-propanol (5 min. each step) in an ultrasonic bath. Substrates are then dried with a nitrogen flow and mounted on the evaporator holder in 6- to 12-unit batches. Metals are evaporated: titanium (2nm) is evaporated by e-beam evaporation at $1/s$, and gold is also evaporated at $1/s$. Once the process is finished, the samples are stored in clean conditions in a desiccator in the cleanroom.

2.2.2 E-beam exposure

In a negative lithographic process, the 'negative' refers to the negative exposure mode, since the resist that is exposed is what remains after the development process, while the non-exposed are washed away. I have mainly used the ARN-7500.08 e-beam resist, as it combines high resolution and a reasonable exposure time. The structures were mainly designed using CAD software and then exported to machine language. For electron beam lithography (EBL), I used the CRESTEC CABL writer for substrate exposure.

Each combination of substrate + coating is baked at $110°C$ for 5 min., cooled for 1 min., spin-coated with the resist at $8000rpm$, and baked at $85°C$ for 1 min., resulting in an $80nm$ layer. The sample is then loaded and the chosen design is exposed. For a typical chiral sensing experiment, the resist exposure could take 8-12 h. After exposure, the sample is developed for 3 min. in 4:1 developer:DI water and baked at $85°C$ for 1 min. to enhance etching contrast.

2.2.3 Dry etching

Dry etching uses gas plasma to isotopically or directionally remove material from the substrate in a selective manner. I used PlasmaLab System 100 ICP from Oxford Instruments. Directional argon plasma was used to etch the gold layer at $15nm/min$. The gold etching was not sharp, in that the side walls typically formed a $65-70$ angle due to gold redisposition. This effect makes the gold structures non-symmetrical in the perpendicular direction to the array.

After gold etching, resists were removed for subsequent sensing experiments. Oxygen plasma was used to isotropically remove the resist without affecting either the gold or the substrate. During this project I have used both PlasmaLab and PVA TePla for oxygen cleaning. The latter was eventually acquired and located in the cleanroom, and has since become my first choice.

2.2.4 Wet etching

We encountered occasional resist removal problems and altered etching rates, mainly due to the multi-process use of the plasma system, which can result in chamber cross-contamination and altered plasma conditions. In sensing experiments, not removing the resist mask completely can obstruct molecule-nanoparticle interaction, so it is crucial to ensure proper resist removal. However, this is not easily verifiable before the sensing experiment is performed.

As an alternative to oxygen plasma, chemical wet etching can efficiently remove the resist. Piranha solution has a high etching rate for organic compounds and does not affect gold or glass. However, it may slightly etch titanium, which means it must be used with care. Substrates were immersed in a 4:1 solution of $H_2SO_4 : H_2O_2$ for 8 seconds in order to efficiently remove the resist while minimally altering the structures. However, this is an aggressive, stochastic wet process that slightly anneals structures, so it must be carefully controlled. Note that concentrated Piranha is a very aggressive, organic reactive solution, so maximum safety regulations should be taken into account.

2.3 Microfabrication of the microfluidic parts

Microfabrication involves techniques used to create micro-scale objects[55, 56]. In particular, soft lithography technology consists of replicating micro-feature objects using elastomeric materials, mainly PDMS[57]. Sylgard 184 elastomer was used for 2-layer microfluidic chips, following a regular PDMS fabrication process[28]. The typical fabrication process for PDMS chips is as shown in Figure 2.3, although mould fabrication is occasionally used when chip design changes.

2.3.1 Moulds

Master mould was fabricated in the cleanroom using AZ9260 on polished silicon wafers. AZ9260 was used for flow and control layers in a negative optical lithography process where Quintel Q4000 was used as a mask aligner. Masks were designed using a CAD software and printed with high resolution InkJet printing (extra-dense ink) on a highly transparent sheet.

Silicon wafers were cleaned in soap + DI water, DI water, acetone and isopropanol (5 min. each step) in an ultrasonic bath. Substrates were then treated with UV ozone for 5 min., and spin-coated with AZ9260 at $2000rpm$ (maximum speed). The control layer wafer was double-coated. After UV exposure and flow-

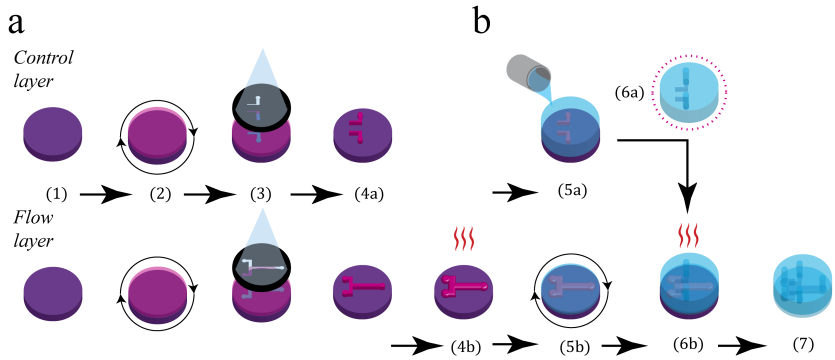

Fig. 2.3 Microfabrication process. a) Mould fabrication, which includes the following steps: (1) clean silicon wafer; (2) photoresist spin-coating; (3) UV-mask photo lithography; (4a) development, (4b) temperature reflow of the flow layer. b) PDMS casting, which consists of (5a) pouring PDMS onto the control layer mould; (5b) PDMS spin-coating on flow layer mould; (6a) control layer drilling, PDMS UV-Ozone activation; and (6b) layer assembly and baking; (7) flow layer drilling and finishing.

layer development, the mould was baked at $140°C$ for 20 min. in order to anneal the channels and make them round-shaped and smooth the surface. The control layer mould was not baked, so that the channels remained square-shaped. The final thickness of channels was $10-11\mu m$ and $22-24\mu m$ for flow and control layer moulds, respectively.

2.3.2 PDMS chips

Chips were made by casting PDMS in silicon moulds. The flow layer was spin-coated at $2000rpm$ to a thickness of $20\mu m$. The control layer was created by dropping a controlled volume of PDMS over the mould inside a Petri dish. The geometry was calculated to produce a $5mm$ thick control layer. Liquid PDMS was baked for 1h at $80°C$, after which the control layer was cut and the control inlet holes were punched. The pieces in control layers and the spin-coated flow layer were activated using UV ozone for 3 min. The control layer was then rapidly aligned and assembled with the

flow layer, and the assembly was then baked for at 80°C for 1h. Finally, the complete microfluidic chip was peeled off, cut and punched.

2.3.3 Assembling

The assembly of the PDMS chip and the plasmonic substrate may be more difficult than it seems. PDMS is usually activated by oxygen plasma and has a tight time window, so specific plasma power and frequency need to be calibrated. Ideally, the plasmonics substrate is also exposed to oxygen plasma in order to activate the glass and put it in contact with PDMS, so that a strong covalent bound is formed between the PDMS and the glass. However, in most sensing experiment the plasmonics sensors are protected or functionalized with organic molecules, which are very sensitive to oxygen plasma. In such cases, substrate exposure needs to be omitted. Under these conditions, PDMS and glass are not usually well bound, and binding needs to be done very quickly right after PDMS exposure to plasma. After they are put in contact, a subsequent baking step (at 50°C for 8h or at 80°C for 4h for non-coated sensors) helps bind the entire chip.

2.4 Surface chemistry

Surface chemistry is the study of how the surface properties of materials change. This is a very relevant area for the present work because plasmonics sensors are more sensitive in the areas that are closer to their surface. Thus, the goal of sensing experiments will be to bring the molecules of interest as close as possible to the sensors' surface, or even to put them in direct contact with the sensors.

While my PhD has focused mainly on other complex fields in this multidisciplinary project, surface chemistry plays a fundamental role in the experiments, so here I will mention the most commonly used protocols. Figure 2.4 shows the process from the point of view of gold sensor surface chemistry.

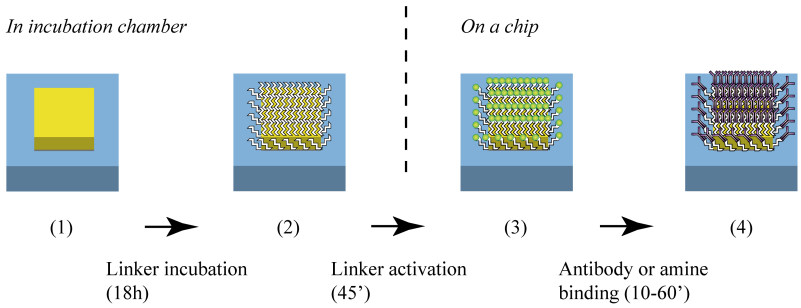

Fig. 2.4 Surface chemistry on gold sensors. The bare sensors (1) are incubated with MUA (linker) in a sealed dark chamber (2). Once on the microfluidic chip, the linker is activated using EDC/NHS (3) and later binds a molecule containing an amine group.

2.4.1 Self-assembly monolayers

A self-assembly monolayer (SAM) is layer of molecules that spontaneously organise over a surface. In doing so, they typically change the surface properties of the material. Hydrophobicity is one of the properties that is usually modified using SAMs[58].

A SAM containing mercaptoundecanoid acid (MUA) over the gold plasmonic sensors was regularly used in bio-sensing experiments. The SAM is built by incubating MUA in a bath of ethanol, along with the plasmonic sensors, usually for 18h. MUA molecules contain a thiol group that reacts with gold, thus creating a covalent bound. Over incubation time, molecules can move and perfectly organize themselves in a highly-packed layer over the sensors. This coating serves a two-fold purpose: it protects the sensors from liquid annealing inside the micro channels, and plays the role of a bio-recognition layer in combination with the amine-coupling protocol. In essence, it will be used to trap molecules with amine groups near the sensors.

2.4.2 EDC/NHS protocol

The preferred method for attaching molecules near gold plasmonics sensors involves an amine-coupling protocol, in which, through an EDC carbodiimide crosslinker, a Sulfo-N-hydroxysuccinimide reaction takes place involving the MUA's carboxyl groups (usually known as EDC/NHS reaction). We typically call this reaction the activation step of the sensor, because it transforms the passivated MUA layer into a capture layer that reacts with other molecules containing amine groups. Thus, antibodies (for example) can be attached to the gold sensors and detected.

2.5 Experimental setup

An important part of my PhD involves building the experimental setup for microfluidic flow manipulation, visualisation and scanning of the entire integrated chip, and the spectral acquisition and processing of plasmonic sensors in real time.

During my PhD, the setup has been upgraded up to six times, mainly to add new features and to reduce noise. It consists of a white light transmission microscope in which the sample (either the fully integrated chip or a single plasmonic substrate) can be illuminated with linear or circular polarized light. The spectrum of light transmitted through the sample can be analysed using a grating spectrometer. Additionally, the sample can be scanned on an XYZ stage and observed at two different magnifications. In addition, microfluidic micro-pumps can be controlled using a pneumatic system.

The various instruments can be either controlled independently in single-spectrum acquisition mode, or automatically synchronized in real-time acquisition mode. I used LabView for instrument control. Data obtained in real-time acquisition mode were also partially processed using LabView.

Figure 2.5 shows a schematic picture of the optical setup.

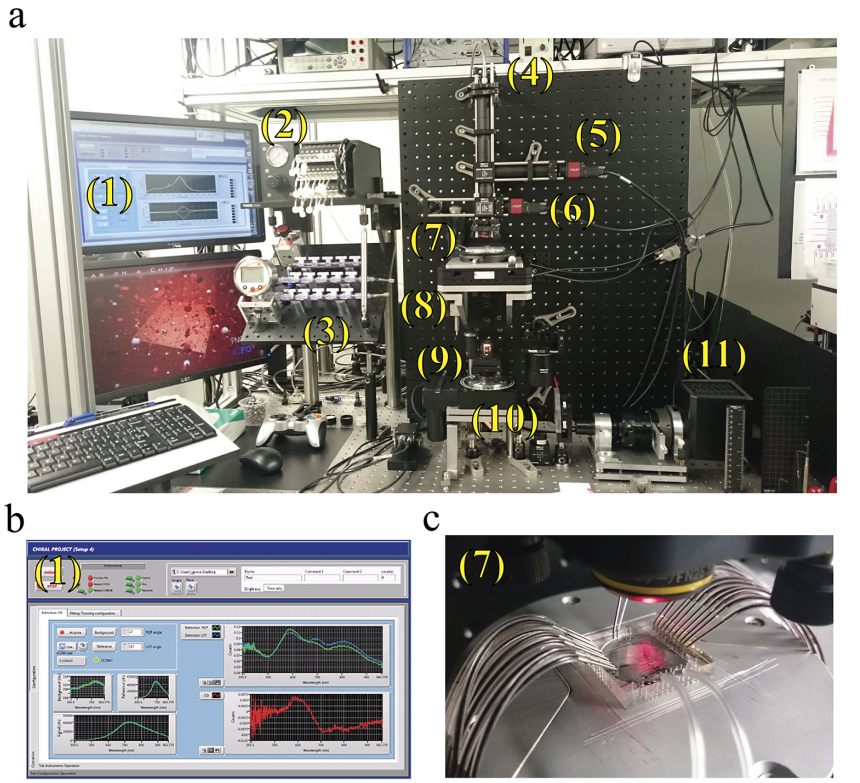

Fig. 2.5 CD-LSPR setup. a) A picture of the experimental setup showing the following main parts: (1) PC to control, acquire, pre-process and display data; (2) electronic pneumatic pump system; (3) reagent reservoirs; (4) fibre coupling to the spectrometer; (5) high-magnification camera; (6) low-magnification camera; (7) sample, i.e. plasmonic-microfluidic chip; (8) XYZ automated stage; (9) broadband lambda quartz; (10) linear polarizer; (11) white light source. b) Detail of one of the acquisition panels of the LabView software. Particularly, the panel is used to acquire the spectrum and calculate extinction and CD. c) Zoom-in on sample area. The collection objective is visible above the plasmonic-microfluidic chip, which is connected to the inlet and outlet tubing.

2.5.1 Spectroscopy

The spectroscopy configuration uses a 100-W halogen white light source (Olympus collimator system) that reaches a linear polarizer (Glan Laser Thorlabs) mounted on a fast rotation stage (URB100CC Newport). When linearly polarized light reaches a broadband quarter wave plate (Fresnel rhomb Thorlabs), the output can vary from linear X or Y parallel to left- and right- circularly polarized light, depending on the incident polarization angle. Once light has passed through the quarter wave plate, the beam is slightly focused on the sample (within $5mm$ diameter area, approximately). Thus, polarized light can be considered uniform over the nanostructures, which are typically $60-120\mu m$ in size. The light transmitted through the structures is collected through a low NA objective ($5x$ Olympus $NA = 0.13$), so scattering may be disregarded and extinction measurement is considered. After the collection objective, the light is split to be imaged by two camera systems with different magnifications; one is used to obtain an overall picture of the microfluidic chip network, while the other is used to visualize the plasmonic sensors in detail, for placement purposes. To measure the spectrum of light, a small region of the illuminated area, called the collection area, is captured an optical fibre connected to the grating spectrometer. This area is $60\mu m$ in diameter and has been optimized to achieve a balance between fast exposure times, the need to average a large number of plasmonic structures in the array, and the need for reasonable fabrication times for the plasmonic structures.

2.5.2 Microfluidic control

Microfluidic control is independent of the spectroscopy setup. Manual and automatic pneumatic valves are implemented. Different pressures are delivered in a controlled manner for the control and flow lines of the microfluidic chips. They can be regulated to control the closing pressure of the micro-valves and the flow speed inside the micro-channels. Automatic valves can be programmed to switch on/off (close/open microfluidic valves) at previously defined times, such that chemical protocols can be handled more easily and precisely. The system can control up to 24 micro-valves and feed 10 flow channels.

2.5.3 Real time CD setup configuration

Circular dichroism can be calculated using the setup configuration shown in figure 2.5, as previously described in section 1.4. Left and right circularly polarized light spectra are acquired and then subtracted to obtain, in this case, a differential extinction value (see Eq.2.1). Differential extinction is somewhat proportional to CD, but has sharper peaks that are useful for tracking purposes. CD can also be calculated in millidegrees from transmission signals, as shown in Eq.2.2.

$$CD(\Delta E) = E_{LCP} - E_{RCP} = log_{10}\left(\frac{(Ref_{LCP} - Bac_{LCP})(Sig_{RCP} - Bac_{RCP})}{(Ref_{RCP} - Bac_{RCP})(Sig_{LCP} - Bac_{LCP})}\right) \quad (2.1)$$

$$CD(\theta) = \frac{0.18}{\pi} atan\left(\frac{\sqrt{T_{RCP}} - \sqrt{T_{LCP}}}{\sqrt{T_{RCP}} + \sqrt{T_{LCP}}}\right) = \frac{0.18}{\pi} atan\left(\frac{\sqrt{\frac{Sig_{RCP} - Bac_{RCP}}{Ref_{RCP} - Bac_{RCP}}} - \sqrt{\frac{Sig_{LCP} - Bac_{LCP}}{Ref_{LCP} - Bac_{LCP}}}}{\sqrt{\frac{Sig_{RCP} - Bac_{RCP}}{Ref_{RCP} - Bac_{RCP}}} + \sqrt{\frac{Sig_{LCP} - Bac_{LCP}}{Ref_{LCP} - Bac_{LCP}}}}\right) \quad (2.2)$$

Bac., Ref., and Sig. represent the acquired background, reference and sample signals, respectively. LabView software allows one to control and synchronize light polarization, the position of the chip collection area and spectrum acquisition. Thus, the program can continuously acquire the spectrum of different plasmonic structures at different polarizations inside the microfluidic chip. The spectra can be processed during acquisition, extinction and/or CD. Peaks and/or centroids can be calculated and plotted for the different structures as a function of time, and changes in the sensor can be tracked in the different steps of the protocols.

The setup is designed for chemical protocols involving plasmonic sensors located inside the microfluidics channels, and for tracking changes in their resonance. Automatic valve control is independent of spectrum acquisition; both systems are launched at the same time and data are synchronized afterwards. Similarly, the procedure can be followed with manual control of the micro-valves.

After completing the experiment, data are processed with MatLab (with more accurate algorithms) and plotted for the analysis using OriginLab.

2.5.4 Electro-thermo-plasmonic setup configuration

I built an additional setup for electro thermo plasmonic experiments. It contains the same basic structure, but is designed to work with simultaneous cross linear polarization instead of alternate circular polarization. To achieve this, the excitation source mixes white light and a 785nm laser beam through a non-polarising beam-splitter (a combiner in this case).

Figure 2.6 illustrates the setup. The laser light beam (785nm Toptica XTRA) is linearly polarized, and its polarization is oriented perpendicular to the polarization of the 100W white light source, which is also linearly polarized. Beam polarizations are strategically crossed to excite the transversal and longitudinal resonances of the specially designed gold nano-rod sensors. The laser beam is loosely focused over the LSPR micro-fluidic platform within an area of 60μm in diameter. White light is also loosely focused within an area of 5mm diameter, using a 50X long working distance objective (LMPLFLN50x Olympus). The light travelling through the chip is collected by a low NA objective (LMPLFLN5x Olympus), and then imaged by a camera and coupled to an optical fibre that delivers the light to a spectrometer (USB400 VIS-NIR Ocean Optics). In this case, the pneumatic system that enables microfluidic valve control and flow pumping is manual only.

LabView software is also used to acquire spectra and to process the peak positions, which is plotted as a function of time during the experiment. I prepared an extra program, also in LabView, to apply a feedback loop on the laser and improve power stability on the sample. Feedback control is obtained by reading a photodetector placed in the first beam splitter.

In this chapter, I have introduced the toolbox used to carry out plasmonic integrated microfluidics experiments. Many of the regular steps in this process involved hand-made components, thus making every experiment unique. I have placed a spe-

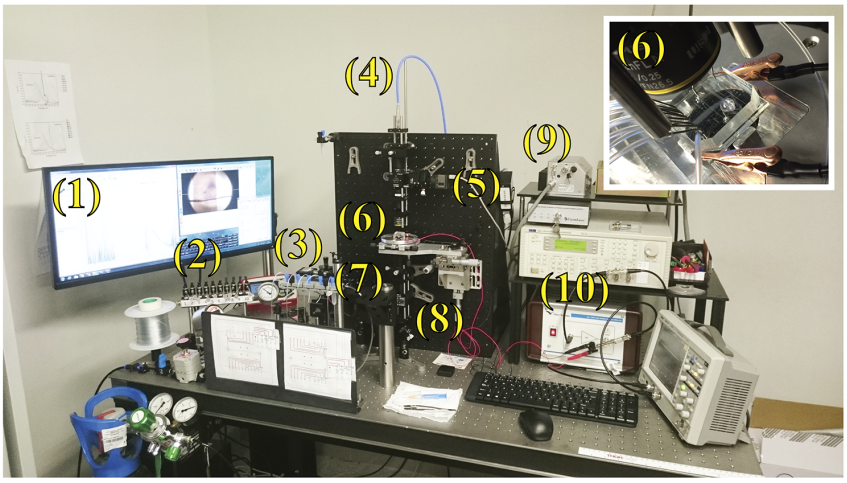

Fig. 2.6 Electrothermoplasmonics experimental setup. The main parts are listed as follows: (1) PC for data control, acquisition and display; (2) manual pneumatic valve system; (3) reagent reservoirs; (4) fibre-coupled spectrometer: (5) imaging camera; (6) sample; (7) white light; (8) beam splitter to combine laser and white light beams; (9) fiber-coupled diode laser and (10) electric sources. The inset shows a zoom-in on the ETP chip.

cial emphasis on minimising fabrication differences and uncontrolled parameters, and these efforts have provided us with a platform for obtaining reliable, state-of-the-art measurements.

3

Enantiomer-selective molecular sensing using racemic nanoplasmonic arrays

Abstract. Building blocks of life show well-defined chiral symmetry which has a direct influence on their properties and role in Nature. Chiral molecules are typically characterized by optical techniques such as circular dichroism (CD) where they exhibit signatures in the ultraviolet frequency region. Plasmonic nanostructures have the potential to enhance the sensitivity of chiral detection and translate the molecular chirality to the visible spectral range. Despite recent progress, to date, it remains unclear which properties plasmonic sensors should exhibit to maximize this effect and apply it to reliable enantiomer discrimination. Here, we bring further insight into this complex problem and present a chiral plasmonic sensor composed of a racemic mixture of gammadions with no intrinsic CD, but high optical chirality and electric field enhancements in the near-fields. Owing to its unique set of properties, this configuration enables us to directly differentiate Phenylalanine enantiomers in the visible frequency range.

3.1 Introduction

Chirality, geometrically understood as the lack of symmetry under specular reflection, is of major importance in biological systems as well as biological and chemical processes[59, 31]. For example, biological receptors for taste and smell are sensitive to enantiomers, the two mirrored images of a chiral molecule, and can chemically differentiate them by producing different responses that we interpret as, for instance, drastically different scents[60, 61]. This asymmetry is critical in the case of the physiological action of drugs, where in the worse scenario one enantiomer acts as a medicine while the other has detrimental effects[62, 63].

Since such critical biological actions can be related with chirality, several spectroscopic techniques have been developed over the years to differentiate enantiomers. Such techniques include circular dichroism (CD), optical rotatory dispersion (ORD) and Raman optical activity (ROA)[33, 34]. Although powerful, these techniques suffer from low signals and sensitivity (ROA) or are located in UV spectral range (CD and ORD), which rely on expensive equipment.[35].

The recent developments in nanotechnology come with novel metamaterials and nanophotonic sensors that exhibit high sensitivity and promising properties for bio-sensing applications[64–66]. These sensors concentrate light efficiently, creating highly sensitive nano-regions that interact strongly with matter and can be used to detect very small amounts of molecules through changes in their resonance wavelength[67–70]. Nanostructures and metamaterials can also be designed to mimic the properties of chiral molecules, controlling the polarization of light in a given wavelength range[42, 71–78]. For instance, giant circular dichroism signals has been reported in the visible (VIS) and near infra-red (NIR) spectral range[72, 78]. Additionally, nanostructures can be devised to provide local fields with large so-called optical chirality, C, defined as $C = (\frac{-\varepsilon_0}{2w} Im(\mathbf{E}^* \cdot \mathbf{B})$. Here, ε_0 is the vacuum permittivity, ω the angular frequency of light, and $\mathbf{E}$ and $\mathbf{B}$ are the electric and magnetic fields of light, respectively. Considering that C is ± 1 for left (σ^+) and right (σ^-) circularly polarized light respectively, larger values may promote stronger light-molecule interactions and thus be beneficial for the detection of chiral molecules.[79–

82]. However, there can also be a strong interaction between localized plasmons in metallic nanostructures and chiral molecules that induce CD signals through dipole and multipole Coulomb interactions[48, 83, 84]. Although it is still not clear what is the best way to extract conformational information from molecular signals coupled to plasmonic systems, several methods have been proposed for the detection of chiral molecules[48, 85–89]. While most of these methods use CD as a primary measurement of chirality some works have also used related signals, e.g. differential transmission, and proposed different ways of extracting the chiral information from the molecules[89, 90, 46]. There are several reports on induced CD from molecules near non-chiral plasmonic structures, that is, structures that exhibit no intrinsic CD signals[83, 91–93]. This method generally relies on plasmonic systems with high electric fields enhancements, but low C. Recently, attention has turned towards chiral plasmonic array-based sensors that experience both large intrinsic CD and C[90, 46]. However, the drawbacks of these designs has been (1) the high intrinsic CD of the sensors (Fig. 3.1a-b), often orders of magnitude bigger than molecules, that potentially could over-shadow the small molecular signals and (2) the need for multiple measurements on separate left- and right handed sensors[90, 46, 94].

In this work, we propose a plasmonic sensor (Fig3.1c) with highly chiral individual components composed in a 2D arrangement together with the enantiomeric counterpart, which result in a non-chiral superstructure. This sensor design has important advantages in terms of both functionality and reliability. While using chiral sensors is desired to achieve high optical chirality, the strong far field CD from the sensors ends up masking the much weaker molecular response. This requires post processing the data in order to extract the chiral signature from the molecules, which eventually can be a source of severe artefacts. Indeed, the subtraction of two very similar spectra may not be reliable especially when involving nano-sensor array that are not fully identical due to nanofabrication deviations. Eventually, our measurements give a direct chiral signature from the molecules hence dramatically increasing the reliability of the sensor. As illustrated in Fig.3.1, a racemic mixture of chiral sensors can keep as large values of C and electric field enhancements in the near fields as the totally handed sensors and at the same time the CD signal of the sensor is suppressed. Racemic sensor arrays have recently been suggested for chiral

molecular detection[94], however this detection scheme has not been implemented experimentally until now. The main idea behind such a sensor is that one molecular enantiomer will interact more with one sensor component, which will shift the CD balance of the entire sensor system and yield a detectable signal. The CD signal is anticipated to mainly depend on the CD and C factor of the sensor components, as the main absorption and CD resonances of chiral molecules reside in the UV. We show that the racemic sensor can be used for direct molecular detection and discrimination between the two phenylalanine enantiomers. D, L and the racemic forms (i.e. D+L at 50/50 concentration, denoted as DL) of the amino-acid are used in order to validate and link the results unambiguously to the chiral conformation of the molecules.

Beyond the use of racemic sensors, another novelty of our study over the prior art is the way the molecules are controllably delivered to the sensors using molecular thermal evaporation (MTE)[95], a rarely used method in this field, but extensively used in molecular electronics. Molecular delivery has also been a limitation in past studies due to poor control and reproducibility issues. MTE is very suitable for our purpose, since it allows accurate control of the molecular deposit conditions and thickness of the coatings, providing more reproducible, homogeneous and dense molecular layers using a solvent-free method[96, 97].

3.2 Racemic plasmonic sensors

Gold chiral plasmonic nano-structures consist in gammadion elements organized in a 2D matrix array of $120\mu m$ in size. The arrays were produced by electron beam lithography (CRESTEC CABL9510C) using a negative resist (ARN7500.08) on $50nm$ gold coated borosilicate substrates separated by a thin ($\sim 2nm$) Ti adhesion layer. After exposure and development, the gold layer was exposed to reactive ion etching (Oxford Plasmalab System 100) followed by resist removal in piranha solution (Caution: piranha solution is a very reactive solution and should be handled with the maximum safety precaution). The nano-structures were optically characterized using a custom-made setup consisting of a white light source followed by a broadband

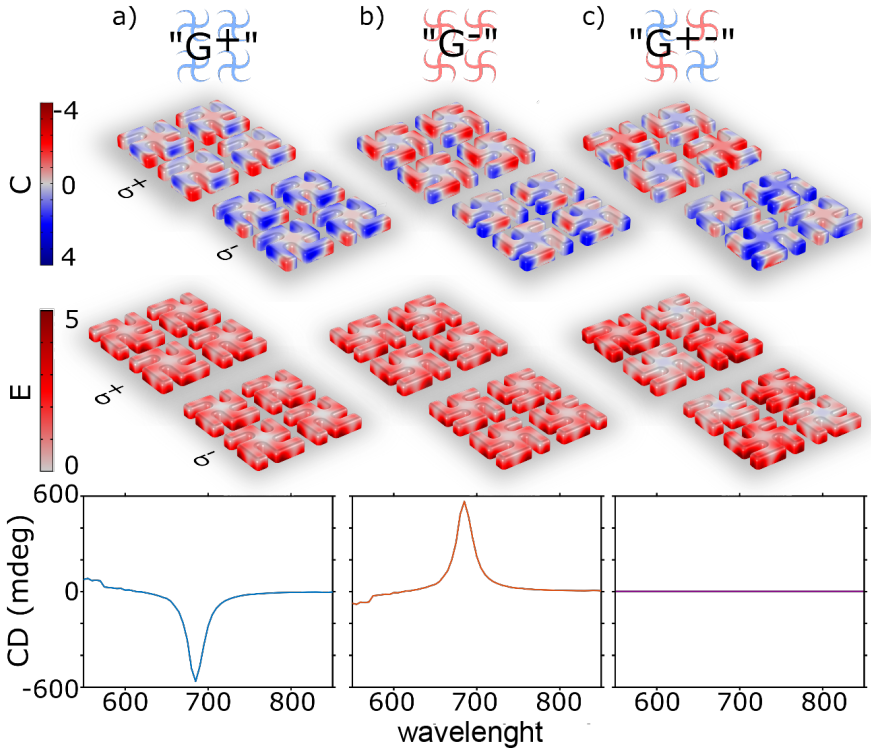

Fig. 3.1 Handed vs. racemic gammadion arrays. The handed arrays, a) G^+ and b) G^-, exhibit large optical chirality (top) and large electric field enhancement (middle), but also large CD (bottom). c) The racemic gammadion array G^{+-} shows large optical chirality and electric field enhancement, but no CD. σ^+ and σ^- indicates excitation with left and right circularly polarized light, respectively.

linear polarizer (Thorlabs GL10) and quarter wave plate (Thorlabs FR600QM), then the sample followed by a low numerical objective (Olympus LMPLFLN5x) which couples to a grating spectrometer (Andor Shamrock 303i iDus401 BR-DD system) through an optical fiber. The interrogated area of the sensor is $60\mu m$ in diameter, which account for an averaging over 28,000 gammadion structures.

In order to visualize the properties of racemic gammadion arrays, we compare these with completely handed arrays. Note that both the gammadion structure as well the racemic and the completely handed arrays have $C4$ symmetry, which ensure anisotropy artifact-free measurements[73]. Figure 3.2 displays scanning electron microscope (SEM, FEI Inspect F) images and spectra of gammadions of $275nm$ in size arranged in a $350nm$ pitch squared matrix. Here, extinction is defined as $E = 1 - T$, where T is the transmitted light, and the CD is calculated using

$$CD = atan\left(\frac{\sqrt{T_{\sigma^-}} - \sqrt{T_{\sigma^+}}}{\sqrt{T_{\sigma^-}} + \sqrt{T_{\sigma^+}}}\right) \tag{3.1}$$

where T_{σ^+} and T_{σ^-} is the transmission of left and right circularly polarized light, respectively. The handed arrays had extinction and CD resonances at $660nm$, either in their G^+ or G^- form, as indicated in Fig.3.2. For the racemic mixture, G^{+-}, we placed right and left-handed gammadions alternatively in a row and then shifted the next rows by one. The racemic array showed a flat resonance peak in between $625 - 675nm$ and zero CD signal all over the measured spectral range (Figure 3.2c). The difference in extinction spectrum is not surprising, as the local environment surrounding a specific gammadion is changed and is thus attributed to the interaction between G^+ and G^- components. This result confirms that, like in molecular systems, right and left enantiomer's CD cancel out in a racemic mixture.

3.3 Molecular layers

Mostly, previous works not only use different sensor systems, but also different chiral molecules like polymeric chains or proteins[83, 90, 91]. These large molecules can

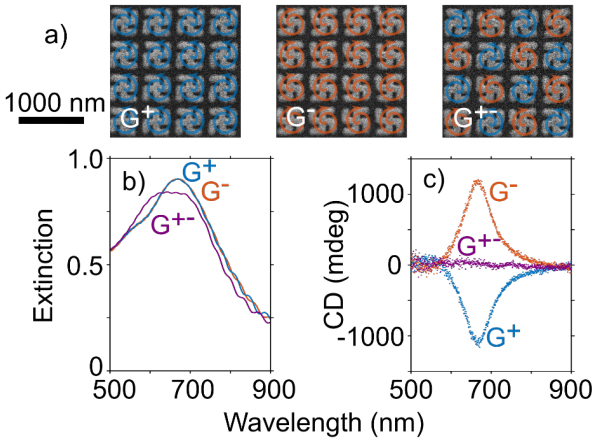

Fig. 3.2 Optical characterization of handed and racemic gammadion arrays. a) SEM images of handed G^+ and G^- arrays, as well as the racemic G^{+-} array. b) Extinction and c) CD spectra of the fabricated nanostructures.

possess supra-structural CD, which might be easier to detect, but the mirror molecule is seldom available, which makes the results difficult to validate thoroughly. On the other hand, enantiomeric systems are typically small and therefore produce small signals that are more challenging to detect. An ideal sensor should not only be able to detect a chiral molecule, but also give signals which reveal the enantiomer handedness in the sample. To fully validate a sensor, it is thus important to test the full set of molecules: not only the two enantiomers, but also the racemic mixture of the two. Phenylalanine, an essential amino-acid, was chosen in this experiment as both enantiomers and the racemic mixture are commercially (78019, P1751 and 147966 Sigma Aldrich). Here, we used molecular thermal evaporation (MTE) in order to accurately control the delivery of molecules and ensure a high density coating. In this technique, the molecules sublimate from a crucible and reach the target substrate similarly to what would happen with conventional metal thermal evaporation (Fig.3.3a). This way the molecules can reach the interparticle regions and the gaps within the gammadion nanostructures. The thickness of the layers can be carefully adjusted using a quartz crystal microbalance (QCM). First, we deposited the different enantiomers and racemic mixture on a quartz substrate. Phenylalanine molecules were sublimated at $100°C$ with a deposition rate of $5A/s$, leading to an

amorphous layer. The thickness was estimated using the QCM readings together with scanning electron microscope images (SEM, Fig.3.3b) and was set to be 150*nm* in order to fully cover all sensitive areas of the nano-structures. The SEM image confirms the uniformity and thickness of the coating.

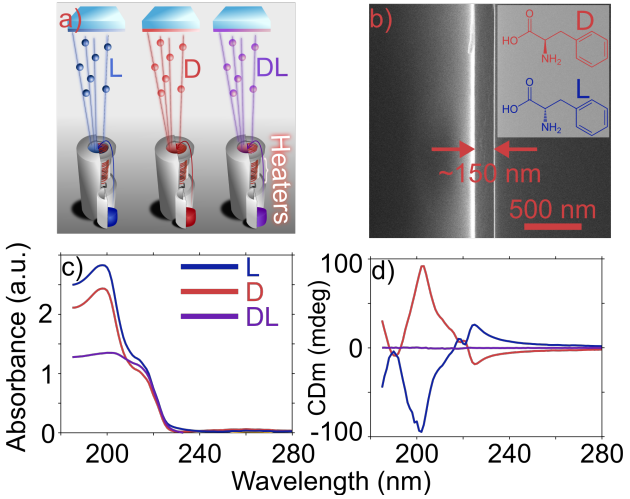

Fig. 3.3 L, D and DL (racemic) coatings of phenylalanine on quartz. a) Schematic of the molecular thermal evaporation technique, where crucibles are filled with the molecules and gently heated under vacuum, until they sublimate and are evaporated on the substrates. b) SEM image of a 150*nm* thin layer of DL phenylalanine. c) Absorbance and d) CD spectra of the respective coatings.

We then characterized the layers optically in a CD-spectrometer (Applied photophysics Chirascan plus), as seen in Fig.3.3c-d. Absorbance spectra of the coatings reveal a main peak at 200*nm* within accordance of 10% for both enantiomers and reflection symmetry of CD. Interestingly, the absorbance of DL coating got on a flat peak in a similar fashion as the racemic plasmonic array. As expected, the CD of the racemic mixture is negligible over in the entire measurement range, confirming the racemic nature of the mixture film. Note that no CD was measured outside of the displayed spectral range for any of the coatings.

3.4 Sensing results

After the previous calibration step on the deposition of molecular layers, we made evaporations of the different molecules on the racemic plasmonic arrays (Figure 3.4). The optical measurements were performed in a custom-made setup, which features a detection area four orders of magnitude smaller than the commercial equipment and no lock-in amplification thus lower signal to noise ratio. Figure 3.4b-c shows the extinction and CD of the coated plasmonic nano-structures. The flat extinction peak from the bare arrays (Fig.3.2b) has now become two close, but distinguishable, peaks. Overall, the extinction increased by 20% in height and shifted about 75*nm* due to the coatings. Exclusively, DL coating extinction increased an extra 10% and split significantly the two peaks in comparison with D and L coatings extinctions. Even more interestingly, the molecular enantiomers induced CD signals with opposite sign originating from the symmetric molecular system (phenylalanine D and L), about 500*nm* from the previous CD peak wavelength. This is made possible thanks to the synergetic effect of the local optical chirality and field enhancement of the sensors which selectively enhances the residual CD of the enantiomers in the VIS-NIR range. Eventually, the signal stems from an unbalance in the racemic array components, in which either G^+ or G^- interacts more with the interrogated molecules. In addition, the DL coating induced no significant CD, in line with the CD measurements of the molecular coatings. These results are in accordance with the symmetry of the system, as we already saw in the molecular coatings and in the plasmonic nano-structures. However, a degradation of the signals and symmetry could be expected due to accumulations of experimental errors for the final measurement. The non-zero CD of the racemic coating could thus originate from slight imperfections in fabrication that lead to different CD enhancements together with minor differences in the coating properties. Additional sets of experiments have successfully reproduced the results, both in the same as well in a completely new batch of sensors.

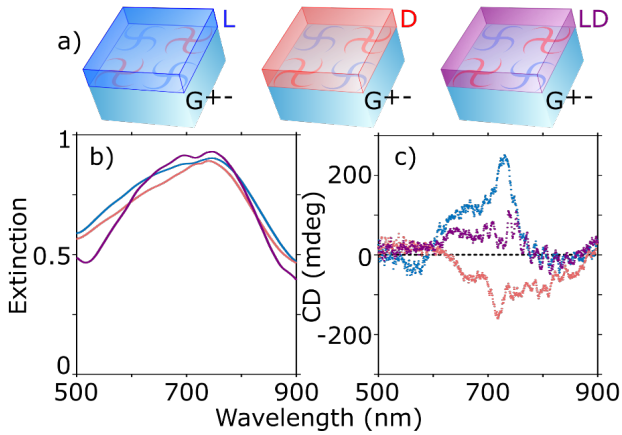

Fig. 3.4 Enantiomer detection in the visible spectral range using racemic gammadion arrays. a) The molecules were deposited on different sensor arrays, showing the corresponding b) extinction and c) CD spectrum.

3.5 Repeatability

Repeatability tests were carried out to validate our conclusions as well as to assess the different experimental sources of deviation. We investigated the UV-CD of the coatings on quartz as well as the CD on our sensors. For investigating the sensor response, we always employed three slightly different sensor arrays on the same chip. Several chips were then coated independently, but we also repeated all coatings on the same sensors after a gentle water cleaning procedure (as molecules are soluble in water). We identified that the deviations in the results can mostly be attributed to the molecular coating. Indeed, measurements on different sensors reveal, on the same chip and with the same coating, only small variations of the induced CD. Conversely, we identified that certain variance in the coating's UV-CD would have direct consequences on the induced CD in the visible.

Figure 3.5a shows the CD (denoted CDm for clarity) in the $220-240nm$ spectral range for three separate coatings of L- and D-molecules, respectively. While the main features of the CD spectra are reproduced in between evaporations, there are magnitude differences that also affect the response of our sensors at $500-900nm$. In order to compensate for this variation, we used the UV-CD to estimate the CD in the

sensing region by using an exponential decay function, see Fig.3.5a. The weight of the estimated molecular CD in the visible was then used to correct magnitude differences of the enantiomeric enhanced signals. To further correct for small measurement and/or fabrication bias errors in racemic sensors, the neutral CD of the racemic coatings were considered as a baseline of the experimental system.

Figure 3.5b-d shows the molecular induced CD for three sets of data, all confirming the repeatability of the effect, using the above mentioned corrections. We associate spectral variations mainly with slight sensor variations. Each subfigure contains spectra of six sensors, three with D-phenylalanine coating and three with L-phenylalanine coating. Figure3.5b and d show the same sensors, that were coated twice, with a gentle cleaning in between. Except for the slight variations in spectral position, these data show that the magnitude and sign of the induced CD is repeatable. Additionally, Fig.3.5c show that very similar results can be reproduced using other sensors arrays that were fabricated in separate batches.

The enhancement is calculated as the ratio CD_G/CD_0, where CD_G and CD_0 are the CD of the molecules+sensors and of the molecules alone, respectively. The maximum enhancement values we measured are of the order of 60 versus 170 in the simulations. Discrepancies are mostly attributed to nanofabrication imperfections.

To illustrate possible errors originating from the molecular coatings and the optical readout using our racemic sensor, Fig. 3.6 shows spectra from the same datasets as in Fig. 3.5, without any applied corrections. From this data, we learn that a weaker UV-CD (Fig 3.6a) of the molecular coatings yields a low CD also when measured on the sensors in the VIS-NIR spectral range. Results also suggest that combined system (sensors + optical system) in this study is prone to yield slightly positive CD values (Fig. 3.6e), however they consistently got more symmetrical after applying the correction (Fig. 3.6f). This effect can stem from non-ideal nanofabrication of the sensors, as well as a slight misalignment in the optical setup.

Finally, we note that sensing variations due to coating wettability, which were not considered in this study, may very well be related with the quality of the coating and molecule/sensor interaction efficiency in general.

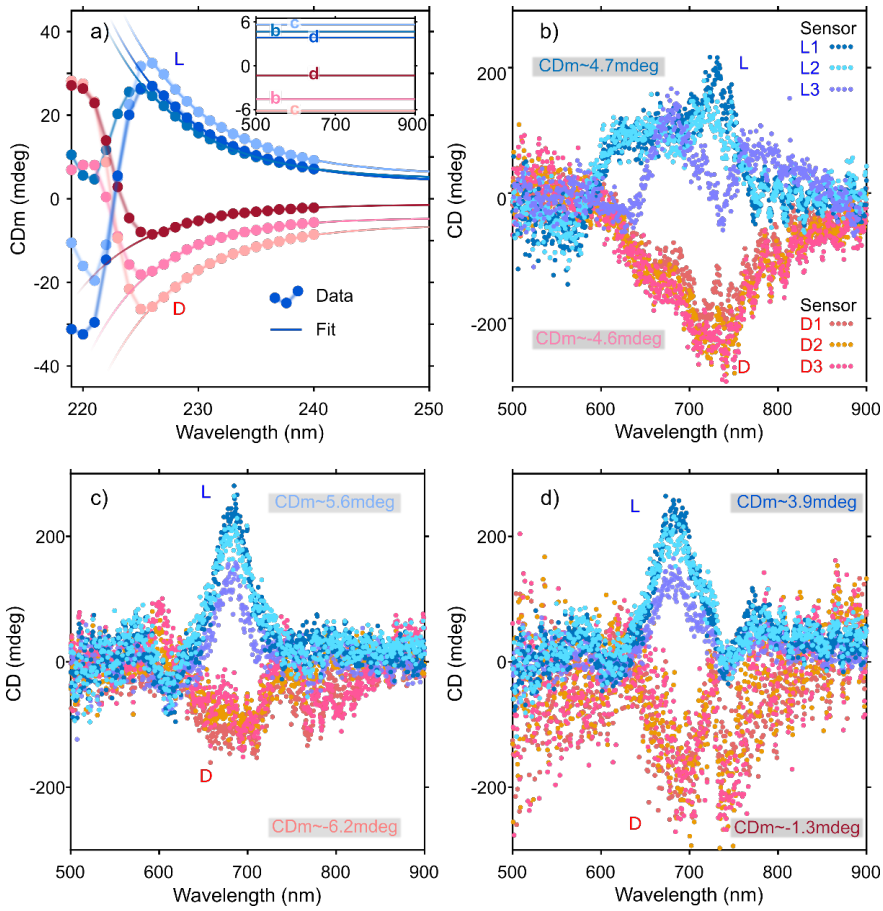

Fig. 3.5 Repeatability of induced CD. a) UV-CD spectra and asymptotic fit of three enantiomeric coatings. The calculated CD values for the molecular coatings in the visible (inset) is indicated in the labels in (b-d). b-d) CD signals corrected for the estimated VIS-CD for the three different sets of coatings in (a). Bluish and reddish data points refer to variations of the sensors in the same chip. The same chips were used in (b) and (d).

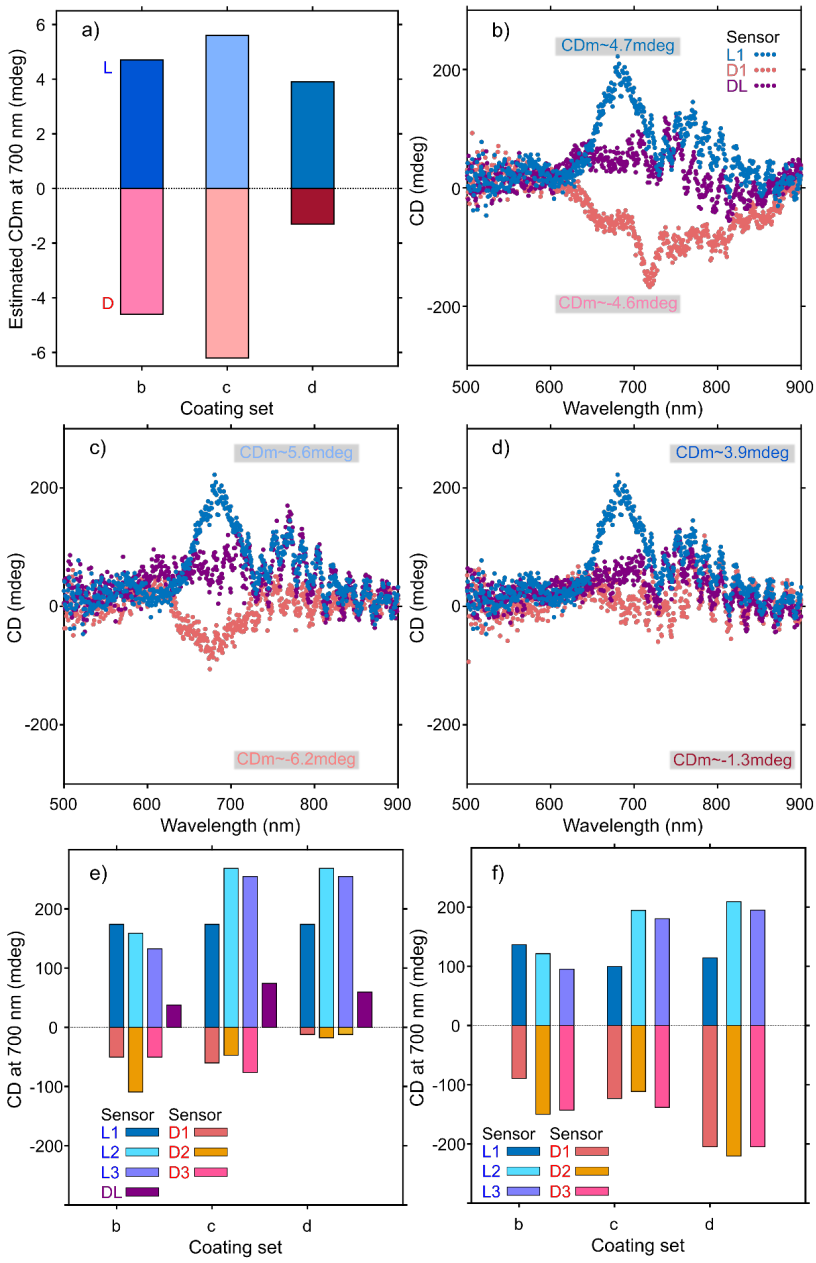

Fig. 3.6 Correction processing effect on the direct measurements of induced CD. a) The estimated CD of three enantiomeric coatings at 700 nm. b-d) CD signals shown in Fig. 3.5b-d without corrections for the estimated VIS-CD for the three different sets of coatings in (a). The bar plots presented in (e) and (f) shown the CD signals values for the estimated VIS-CD at 700*nm* without and with the corrections, respectively, for all the data shown in Fig. 3.5b-d and Fig. 3.6b-d.

3.6 Numerical simulations

COMSOL simulations were performed for racemic gammadion arrays on glass ($n = 1.5$) in molecular refractive index $na = 1.6$, using the geometry in Fig.3.2 (see appendix A for details). Figure 3.7a-b depicts the results, which show two clear peaks in the extinction spectrum and zero CD, in accordance with the experimental results. Experimental peaks are likely broader due to nano-particle fabrication defects that result in inhomogeneously broadened spectra. Note also that the simulations indicate that while the individual components of the array experience very large CD, due to the involved symmetry when combined the total CD for the array is zero. Consequently, small shifts in this balance could motivate detectable CD signals.

Figure 3.7c show the CD enhancement spectra of L and D molecules on top of the racemic sensor. The CD enhancement was calculated from the ratio CD_G/CD_0, where CD_G is the CD of the racemic sensor and the chiral layer, while CD_0 is the CD of only the chiral layer without any nanostructures (see appendix A). The overall line-shape of the simulated spectrum agrees fairly well with the experimental results, even though the latter do not resolve the double peak and feature weaker CD enhancements (see section 3.5). The maximum CD enhancement values are around two orders of magnitude, however, this is likely under-estimated, as the majority of the CD signal originates from a thin layer near the metal (see appendix A), which suggest that it can be much higher locally. In particular, the volume contained between gammadion arms is responsible for about 40% of the CD enhancement (see Appendix A).

Figures 3.7d-f show C and the E-field enhancement for σ^+ illumination at 500, 725 and 900nm, together with their chiral dissymmetry, calculated as $\Delta C = C(\sigma^+) - C(\sigma^-)$ and $\Delta E = E(\sigma^+) - E(\sigma^-)$. Due to the racemic composition of the array, reciprocal patterns of C and E are generated using σ^+ and σ^- illumination. Consistent with the experimental results, the strongest C and the E-field enhancement are found at 725nm. Similarly, ΔC and ΔE are shown to be larger at this wavelength. For a given illumination, the corresponding gammadion within the unit cell, i.e. G^+ under σ^+ or G^- under σ^-, shows stronger E-field enhancement. However, C

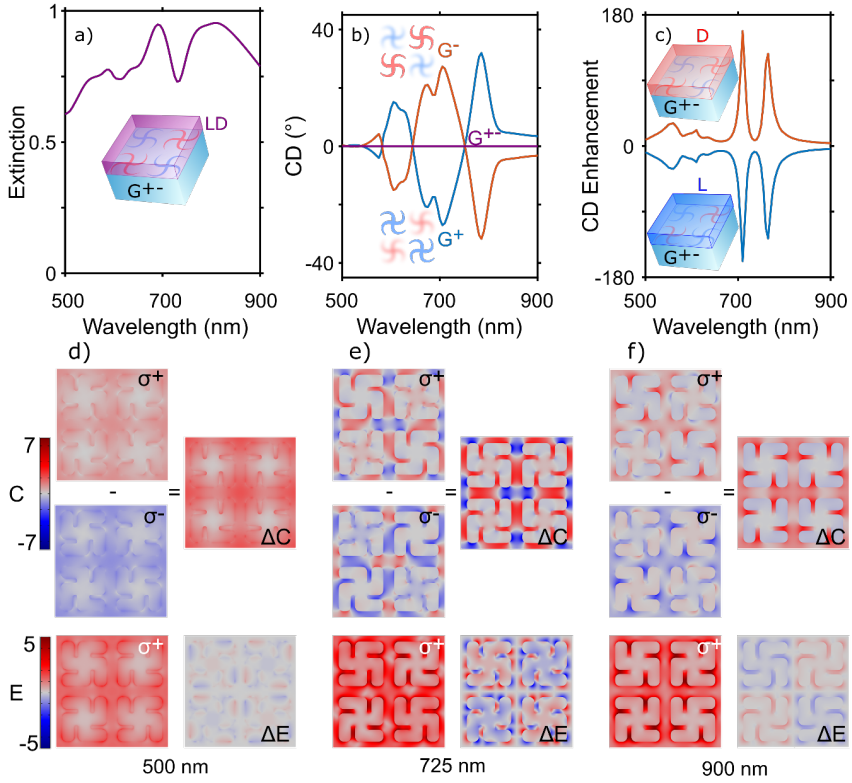

Fig. 3.7 Simulations of gammadions for chiral sensing. a) Extinction and absorption spectra for gammadions on a glass substrate ($n = 1.5$) and in a $n = 1.6$ layer with geometries from the SEM in Fig.3.2. b) CD spectrum of the individual components of the array (G^+ and G^-), showing large and symmetric CD, and the total CD of the system (G^{+-}), without any CD. c) CD enhancement spectrum for the same array with D and L molecular layers. Optical chirality C, the optical chirality dissymmetry ΔC, electric field enhancement E and chiral dissymmetry of the electric field enhancement ΔE at d) 500nm, e) 725nm and f) 900nm.

showed to be larger at odd gammadion-illumination combinations, which is most clearly visualized in the gaps in between the gammadion arms. Regarding C and E dissymmetry, ΔE exhibit clear reflection symmetry with the gammadion handedness, whereas ΔC exhibit handedness-independent distribution.

Aside from the clear wavelength dependence of these parameters from Fig. 3.7, the influence of the parameters on the molecule-sensor system is subtler. The sign of C promotes the interaction for a given enantiomer with the sensor. While the magnitude of ΔC shows the difference of this interaction, which would be related to the discrimination capacity of the system and is shown to be independent to the gammadion handedness. On the other hand, E shows the excitation enhancement for a given illumination. For example, G^+ shows a stronger enhancement for σ^+ illumination and, reciprocally, G^- is best excited using σ^-. Hence, ΔE shows the local chiral dependence of the enhancement. Combining these properties of C and E, a given sensor enantiomorph will interact more with a given molecular enantiomer, for example promoting G^+ and L molecule or G^- and D molecule interaction. At the same time, the symmetry of the array yield equal interaction capabilities with both molecular enantiomers. The racemic array thus enables the enantiomer discrimination in a one-shot measurement.

Conclusions. In this study, we measured CD of L, D and racemic phenylalanine on chiral gold nano-structures mixed in an array in a racemic fashion. The designed sensors showed zero intrinsic CD, but locally high optical chirality and electric field enhancements. When in contact with a chiral molecular layer, the CD signal separates from zero, indicating the handedness of the enantiomer near the plasmonic resonance region. This way we demonstrate that plasmonic sensors can be engineered to offer chiral selectivity while they remain intrinsically CD free.

We show that the use of molecular enantiomers, as well the use of racemic molecular mixture as a control, is a key point to confirm chiral detection in plasmonic sensing experiments, which offers a robust model to validate any chiral sensing platform.

Furthermore, phenylalanine species were evaporated using molecular thermal evaporation, a robust deposition technique that allowed us to deposit layers of $\sim 150nm$ of the different enantiomers and racemic mixture of the molecules. We believe that this method is an important step forward towards more reproducibility in the loading of the chiral sensors as well as a way to better understand the physical and chemical mechanisms involved in plasmon-enhanced chiral sensing.

4

Enantiomer discrimination using micro-fluidics

Abstract. The mechanism underlying the interaction between light and chiro-plasmonic sensors remains unclear, and there is a general lack of the deep understanding required to design effective chiro-sensitive biosensing platforms. Since Tang & Cohen's proposal[98] that super-chiral light can interact more efficiently with an enantiomer of the same handedness, several plasmonic sensing approaches have been proposed for differentiating chirality[47, 91, 99, 100]. In particular, Hendry et al[90] described the use of chiral plasmonic sensors, and the creation of optical chiral hot spots for detecting molecular chirality with enhanced sensitivity. These authors claimed to have achieved a $x10^6$ unit enhancement over conventional CD spectroscopy and picogram sensitivity. While these results have never been reproduced by other groups, they create a new paradigm towards enantio-sensitive detection on-a-chip. The original objective of my PhD thesis was to complete the entire process, to create an integrated chiro-sensitive microfluidics platform capable of differentiating molecular enantiomers. In this chapter, I report our results in this area, with a focus on the issues encountered.

4.1 Introduction

In the original study by Hendry and colleagues, the authors considered a chiral plasmonic sensor formed by an array of lithographically-fabricated gold gammadions[101, 76, 102]. The manufactured arrays were introduced into a liquid cell used to incubate the various molecular analytes that were adsorbed on the sensors' surface. The sensors' circular dichroism was measured before and after molecular adsorption using a commercial CD-spectrometer. The shift of the CD peak between left- and right-handed gammadions was attributed to molecular adsorption, and the shift difference between their peak positions, known as dissymmetry shift, was associated with molecular chirality. The found that certain molecules produced shifts of opposite direction for left- and right-handed gammadions. Six different proteins and one amino acid were screened, and the following conclusions were reached: (i) CD peaks' dissymmetry shifts were of positive value when working with proteins containing beta-sheets and right-handed gammadion sensors; (ii) conversely, no dissymmetry shifts were obtained for proteins containing alpha-helices; (iii) finally, a negative dissymmetry shift was obtained for the amino.

Figure 4.1 shows the spectra of gammadion structures for two of the proteins studied, along with average CD shifts and dissymmetry results for the screened set.

We based our work on the phenomena described above, considering the hypothesis that the CD shift and dissymmetry of chiral plasmonic sensors represents a chiral molecular signature. However, despite the impressive results, we also consider Hendry's configuration to have several mayor drawbacks. First, the sensors (bare gold plasmonic structures) are reused and consequently modified after every use[103]. Second, the molecular set is not optimal, given the lack of racemic references required to validate the chiral effect. Third, liquid cells need to be repositioned after every measurement, which can introduce variations in the results. We wanted to develop a platform that allows us to tackle these drawbacks in order to obtain more reliable results. First, all molecules would be measured under the same conditions; a sensor set that had gone through the same sample processing steps would be used for every molecule. Second, the molecular models would involve enantiomorphs,

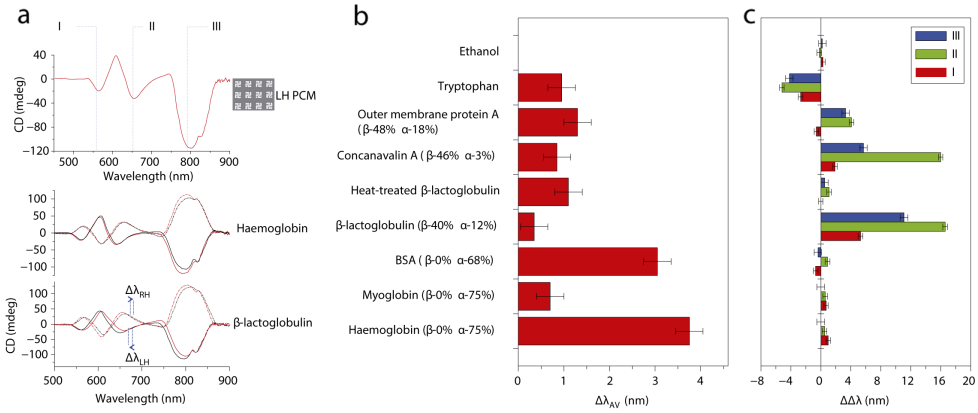

Fig. 4.1 a) CD spectrum of right-handed gammadions exhibiting 3 different modes (top). Experimental data on two different proteins, Beta-lactoglobulin (middle) and Haemoglobin (bottom). The red lines correspond to the spectra of the structures in buffer solution, while the black lines correspond to the spectra obtained after molecular adsorption. While the beta-lactoglobulin spectrum shows clear dissymmetry between spectral shifts, we observe haemoglobin shifts in the same direction. b) Average CD peak shift of the peak mode (I); and c) shift dissymmetry for all modes and all molecules screened. (reprinted from Hendry et al.[90]

and the racemic mixture would be used as an additional reference. By doing so, we expect to obtain a chiral signature of the molecule while suppressing it in the mixture. Third, the system would integrate a microfluidics network to allow reagent manipulation without the need to disturb the sensors.

To deal with sensor reutilization, which can alter sensitivity due to sensor degradation issues, we developed a system in which the gammadion sensors are integrated into a microfluidics network. Different replicas of these sensors are located in isolated chambers, and different molecules may be tested in each of the chambers. Moreover, all sensors go through the same steps towards molecular binding, and mechanical disturbance is avoided (their positions are not altered between one step and the next). Furthermore, CD peaks are tracked in real time in such a way that we can detect potential differences in kinetics between sensors.

To obtain reliable results, we used amino acids as molecular models. One interesting property of optical chirality is the fact that two perfect enantiomers exhibit

symmetrical CD spectra, as they have an opposite optical response to circularly polarized light. This is not the case with proteins, because their chiral properties, or more precisely their CD spectra, are associated with the conformation of their supra-structures (in most cases, secondary to tertiary structures). Therefore, the study of fully chiral models helps understand whether or not the sensor-molecule interaction is related to the chiral properties of the molecule. Additionally, such models are suitable for creating racemic mixtures (mixtures of enantiomers in the same proportion). Interestingly, no CD spectra of racemic mixtures can be obtained, since the contribution of one enantiomer is suppressed by that of its counterpart. As a consequence, the properties of racemic mixtures can be used as a reference to validate the chiral nature of pure enantiomeric samples.

Moreover, we have included racemic gammadion arrays in the set of sensors. This specific array provides a background-free CD measure, while maintaining the near-field optical properties of fully chiral gammadion arrays, as I have shown in chapter 3.

In this work, we studied two molecular models based on amino acid enantiomers. One of the molecular models was cysteine, a thiolated amino acid that, because of its thiol group, may be chemically bound to the gold surface of our sensors. The other molecular model was glutamic acid, an amino acid that can bind to the sensor's functionalized surface by means of an induced chemical reaction (see section 1.3). We decided to use chemical adsorption procedures instead of physical ones in order to prevent the potential desorption of molecules due to subsequent rinsing steps in the microfluidic channel. As a result, we found that the stability of bare gold sensors was compromised during the experiments, whereas functionalized sensors remained stable. Consequently, we measured important shift drifts in the real time acquisition microfluidic platform, which could remain hidden in two-step measurement experiments. Moreover, while we were unable to measure opposite dissymmetry on fully chiral sensors, we observed opposite CD induction by glutamic acid enantiomers on racemic gammadion sensors. This result unambiguously reproduces the accomplishments mentioned in the previous chapter, and shows that racemic chiral sensors are superior for enantiomer discrimination.

4.2 CD-LSPR setup

The CD set-up we developed to measure several experimental conditions simultaneously, and to do so in combination with the microfluidic chip. It allows us to screen enantiomers, racemic mixtures, reference buffers, etc. on different types of sensors under individual experimental conditions at once. Note that the setup was progressively updated during the project, mostly to improve reliability and reduce noise. Thus, the experimental results discussed here have been acquired with different versions of the setup. Nevertheless, they continue to be independently valid.

4.2.1 Microfluidic chip & plasmonic sensors

We used three fluidic architectures to perform the experiments. One was based on a steady incubation chamber with isolated regions to independently combine sensors and molecules, while the other two were based on two-layer PDMS microfluidic technology. Microfluidic networks were conveniently chosen to facilitate surface functionalization protocols and to simplify the overall operation of the platform.

Figure 4.2 shows both microfluidic chip designs. The first (Fig. 4.2a) has four identical network replicas (top-bottom-left-right), each with 4 independent channels. Every channel has 2 inlets and 2 outlets, and this is a suitable design for cysteine experiments, which require the flow of both buffer and molecular solution.

The second design (Fig. 4.2b) has a total of four channels, which can be addressed individually or under a common flow scheme. The individual branches are prepared to deliver one solution (the analyte), while the common branch can deliver up to 4 different solutions.

Plasmonic sensors are formed by a square-shaped, periodic array of gammadion gold nanostructures. In addition to purely left- and right-handed arrays, we also considered racemic arrays containing an equal proportion of both types of handedness. To optimize sensor resonance for our sensing experiments, we carried out an extensive

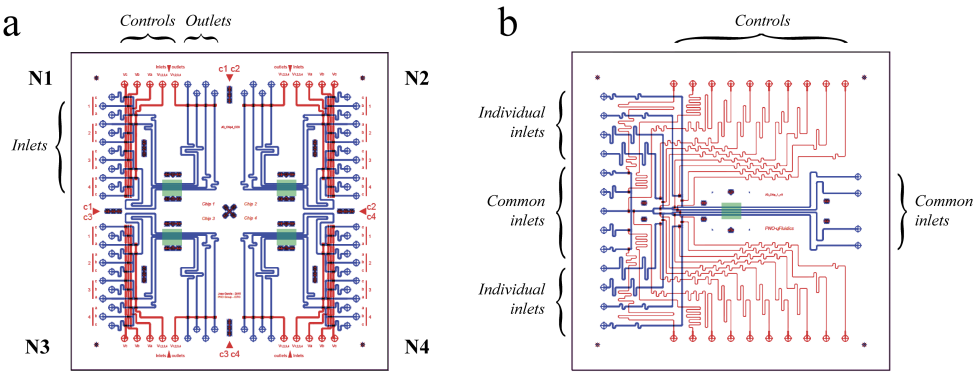

Fig. 4.2 Microfluidic network layouts of the chips used for the experiments: red lines correspond to the control layer, blue lines correspond to the flow layer and green areas correspond to sensor location in the flow layer. a) Chip design with 4 independent channels. N1-4 are the network replicas. This configuration has been used in cysteine experiments. b) Design of a 4-channel chip containing 4 individual inlets and 4 common inlets. This configuration has been used in glutamic acid experiments.

study of geometrical parameters (gammadion dimensions and pitch; sensor thickness was fixed at 50*nm*). Figure 4.3 shows examples of extinction and CD spectra of fabricated gammadions, highlighting the influence of different parameters.

After multiple manufacturing iterations, the optimum design includes 270*nm* gammadions with 70*nm* arms and a 350*nm* pitch, featuring an extinction and CD resonance centred around 675*nm* (see Figure 4.4).

4.3 Cysteine measurements

Cysteine, a non-essential amino acid, is the only amino acid (of the twenty natural amino acids encoded in humans) that contains a thiol group. L-Cysteine, a naturally occurring isomer found in most proteins, is a structural component of many tissues and hormones; in contrast, its enantiomeric counterpart, D-Cysteine, is a non-proteinogenic amino acid. Cysteine is important for protein synthesis and for several metabolic functions. It plays a role in collagen production, and may be found in

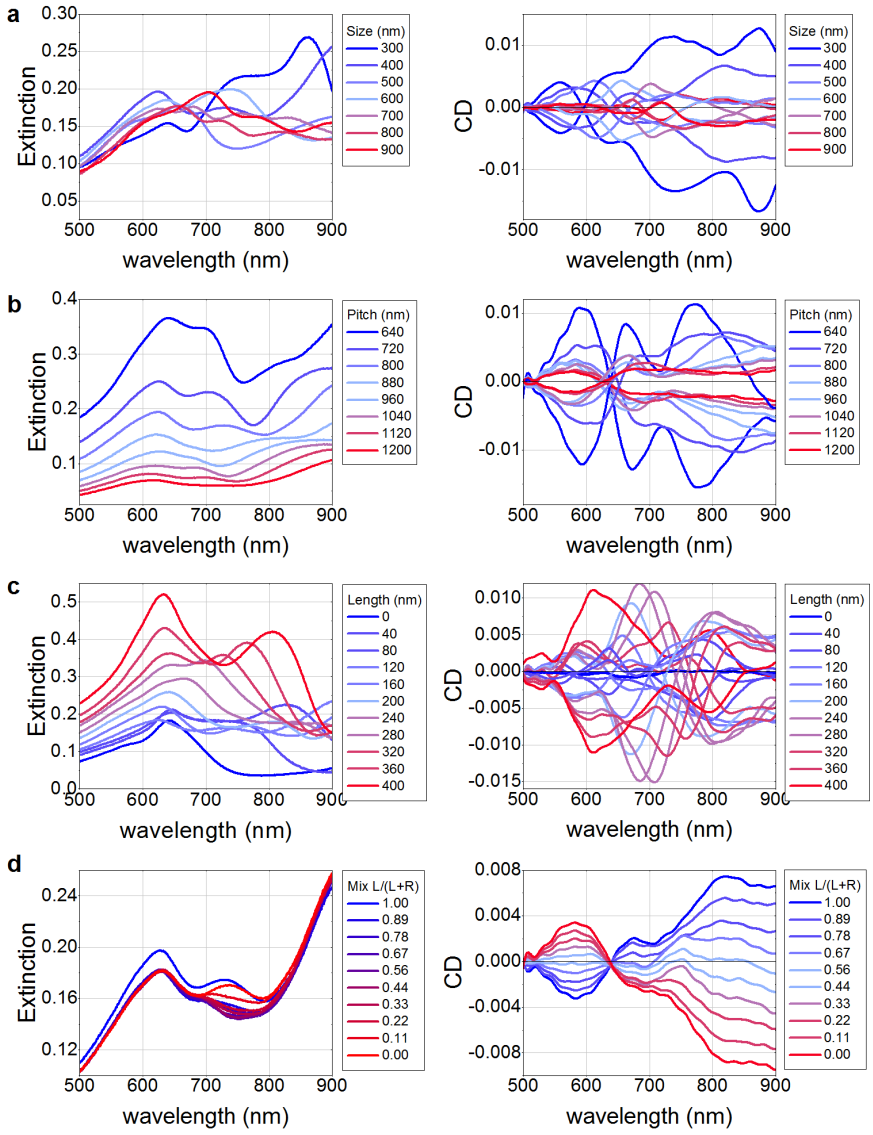

Fig. 4.3 Parametric fabrication of gammadion arrays. LCP light extinction (left) and CD (right) spectra. (a) Outer size variation of the gammadion particle at a proportional array pitch (p=2*size). (b) Pitch length variation at a fixed gammadion size of 400 nm. (c) Gammadion lateral arm length variation from 0 nm (crosses) at 400-nm size and 800-nm pitch. (d) Variation in gammadion handedness inside the array.

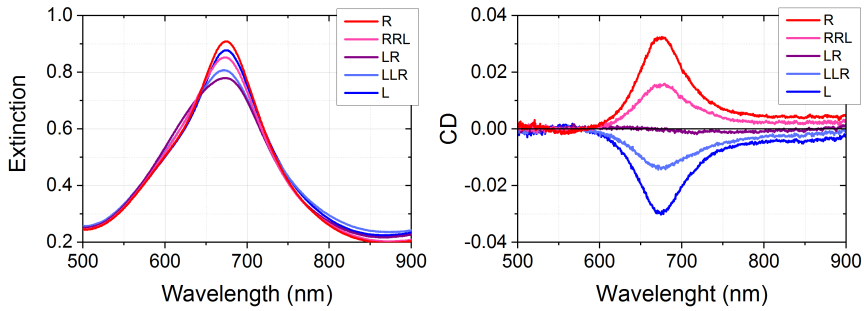

Fig. 4.4 Fine-tuning of gammadion sensor spectra for microfluidic CD-LSPR sensing. Extinction (left) and CD (right) of the left-, 0.75 left-/0.25 right-, racemic mixture, 0.25 left-/0.75 right- and right- handed gammadion arrays. A centre extinction and CD peak is achieved at a 270 nm and 350-nm pitch (Au thickness: 50 nm).

beta-keratin, nails, skin and hair. Cysteine is a component of antioxidant glutathione, and plays a role in the metabolism of essential biomolecules such as coenzyme A, heparin, and biotin. It is also a required component for taurine generation. Oxidation of cysteine's thiol group can form cystine, which consists of two cysteine residues joined by a disulphide bond. Such bonds are crucial for structure definition in many proteins. Cysteine is an important source of sulphur in human metabolism; although it is classified as a non-essential amino acid, it may be essential for infants and the elderly. Cysteine and its derivates exist as a dietary supplement, and are used in a range of clinical applications, including baldness, psoriasis and preventing smoking-related cough. Cysteine is also used for treating asthma. In the future, it may be used to treat cobalt-induced toxicity, diabetes, psychosis or cancer[104–108].

Cysteine isomers have a molecular weight of $121.15 g/mol$ and are highly soluble in water ($> 20 g/L$ at $25^{(\circ)}C$). Their enantiomers are commercially available as a colourless crystalline powder and as a white powder for L and D forms, respectively (30089 Sigma and 30095 Aldrich). The structural difference between the enantiomers is due to swapping the amino group and the hydrogen that are bound to the chiral centre. The molecules have electronic resonances in the UV spectral region; they show equal absorbance between $180-200 nm$ and opposite circular dichroism around $200 nm$. Figures 4.5a and b show their molecular formula and 3D structure, providing

a fairly clear representation of the chiral centre. Figure 4.5c shows the absorbance and CD of the molecules and their racemic mixture in the UV region.

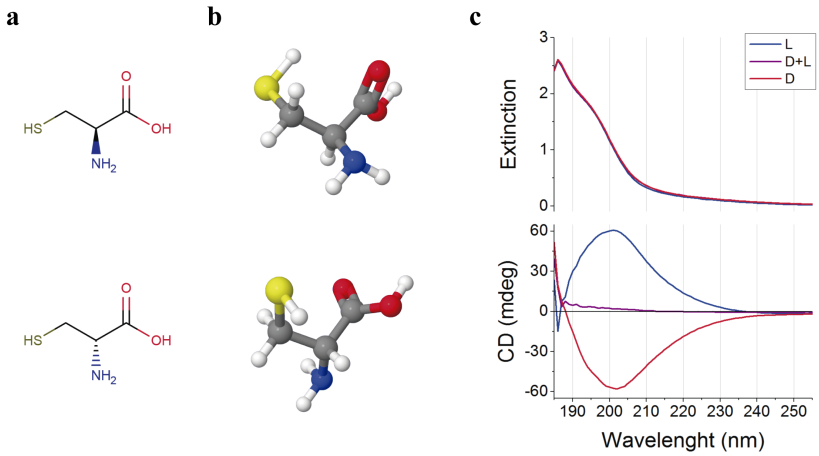

Fig. 4.5 Cysteine isomers; a) molecular formula and b) 3D structure representation of L-cysteine (top) and D-cysteine (bottom). c) UV absorbance and Circular Dichroism spectra of L- and D- enantiomers of cysteine and their racemic mixture

4.3.1 Liquid cell incubation

Since the chemical reactions used for cysteine experiments are quite simple, we decided to incubate the amino acid with the sensors in a buffered solution. The experimental procedure consisted of measuring the sensors' spectral response in the buffer solution to obtain a reference spectrum. Next, incubation with cysteine was performed, and a new measure was obtained in the buffer solution to observe the changes that had been induced as a consequence of the molecular layer. By doing so, we expected to cover the sensor with a cysteine monolayer bound to gold through a sulphide bond.

The original purpose of this experiment was to reproduce Hendry's experiments by performing a similar procedure with a better chiral molecular model. To avoid reusing the sensors, we manufactured 4 sets of handed and racemic gammadions on the same substrate. Each set was used for a single measurement of L- or D- cysteine

enantiomers, its racemic mixture or the reference buffer. Incubation chambers included the substrate and a cover slip separated by a $1mm$ thick spacer.

A phosphate buffer solution ($100mM$ concentration, pH 7) was used as a solvent for the molecules. We performed reference measurements with buffer solution before molecular incubation. All chambers were then emptied and refilled, three with molecular solutions ($82.5mM$ concentration), and one with buffer again. Solutions were incubated in the dark for 1h and then measured.

The results obtained for the CD measurements, before and after molecular incubation, are shown in Figure 4.6. Initial measurements in buffer show a slight discrepancy (around 15%) in terms of amplitude. Higher discrepancies were obtained for the racemic sensor, since the measured signal was ten times smaller. Surprisingly, no shift dissymmetry was detected in molecular measurements. L- and D- enantiomers red-shifted the resonances of fully handed sensors by $\sim 20nm$, while the racemic mixture red-shifted resonances by $\sim 10nm$. Sensor showed similar shifts for both types of handedness. As for the racemic sensor, no clear signal was obtained, although L- and D- molecules produced a larger amplitude change (as compared to the reference) than did the racemic mixture of molecules.

When looking at the extinction spectra (figure 4.7), similar trends to those in CD can be detected. Average shifts continue to be larger for L- and D- molecules, while they remain smaller for the mixture. In contrast, racemic sensors showed multiple peaks after molecular incubation. Peak splitting may be caused by a slight narrowing of extinction bands after molecular adsorption. Qualitatively, overall changes show similar trends to those of CD, with larger shifts detected for enantiomers than those for the racemic mixture.

Spectral analysis did not clearly show the results expected, in that we observed only relatively small differences between molecules. Therefore, we decided to perform a numerical analysis for average shift and dissymmetry, using the following equations:

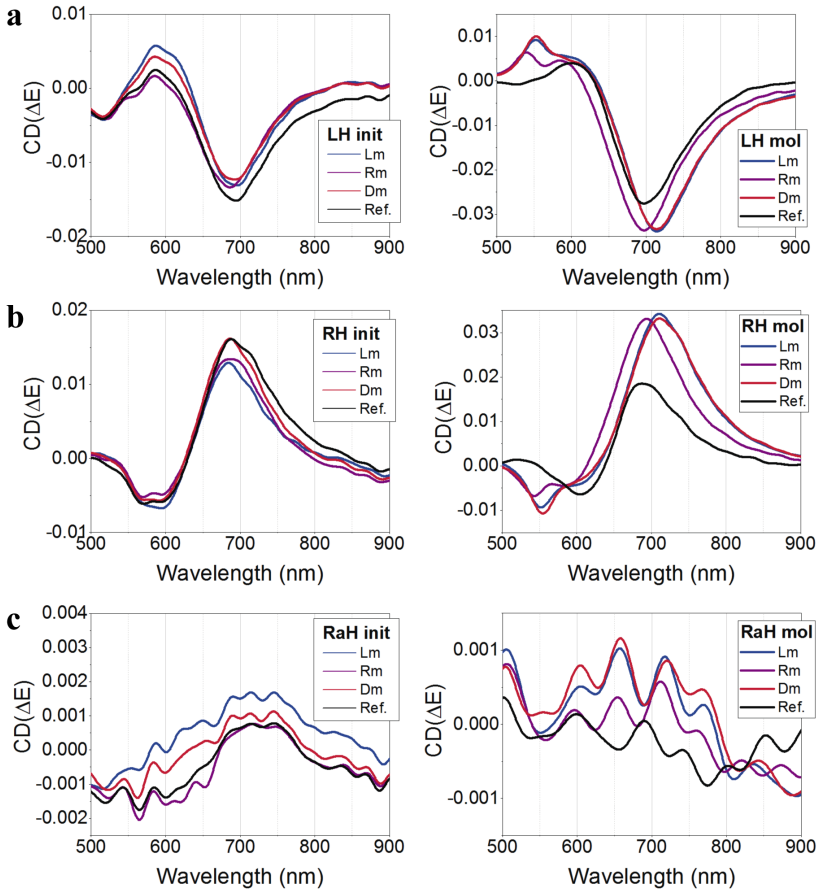

Fig. 4.6 CD spectra for incubated cysteine enantiomers, its racemic mixture and reference buffer on left- and right- handed and racemic sensors (from top to bottom). The left column shows the initial spectra obtained when the sensors were soaked in buffer, while the right column shows the spectra obtained after the sensors were incubated in the corresponding solution for 1h.

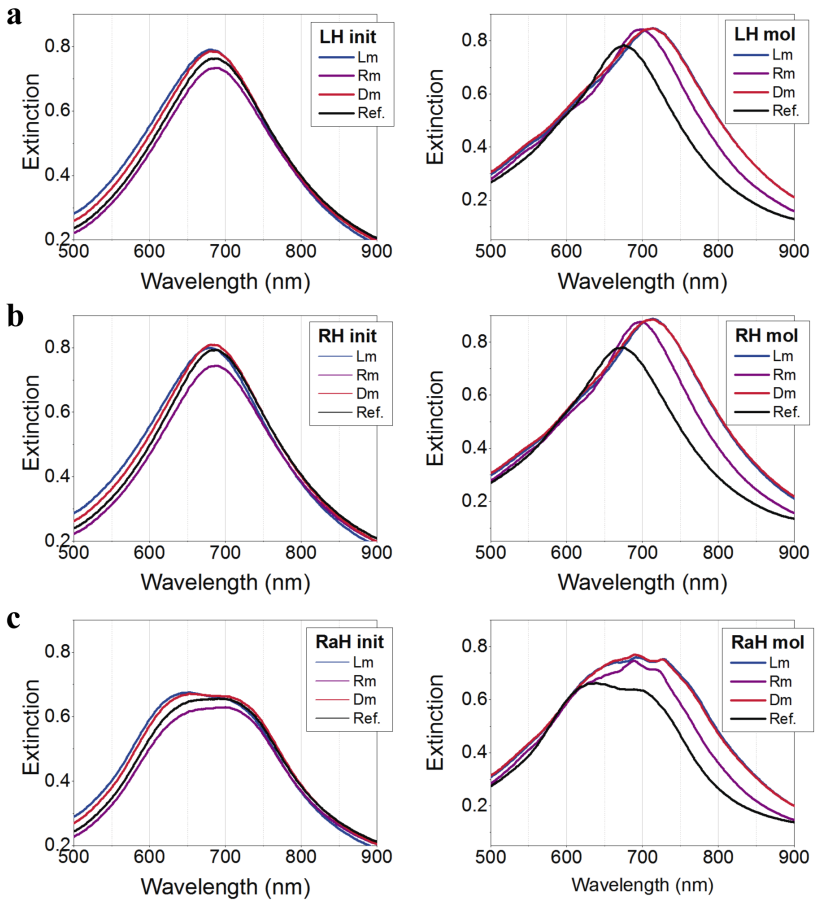

Fig. 4.7 Extinction spectra for incubated cysteine enantiomers, the racemic mixture, and reference buffer on left- and right- handed sensors and racemic sensors (from top to bottom). The left column shows the initial spectra obtained when the sensors were soaked in buffer, while the right column shows the spectra obtained after the sensors were incubated in the corresponding solution for 1h.

$$\Delta\lambda_{AV} = \frac{\Delta\lambda_{LH} + \Delta\lambda_{RH}}{2} \tag{4.1}$$

$$\Delta\Delta\lambda = \Delta\lambda_{LH} - \Delta\lambda_{RH} \tag{4.2}$$

LH and RH sub-indexes refer to left- and right- handed gammadion sensors, respectively. We used opposite dissymmetry notation to that of Hendry et al. so as to maintain overall coherence with the rest of our notation. In terms of racemic sensors, I plotted the extinction central peak and the centroid peak in order to average multiple peak occurrence. In Figure 4.8 I used bar plots to facilitate the analysis of these quantities. The results show a comparable average CD shift for both enantiomers, and less than half of this shift for the racemic mixture. Interestingly, CD dissymmetry took an opposite sign between enantiomers and the racemic mixture. Note also that the dissymmetry obtained for the reference measurement (incubation in buffer solution only) is of the same order as for the molecules. There is no straightforward interpretation of these results. First, the dissymmetry obtained is not what would be expected in a discrimination scenario, since both enantiomers shift in the same direction, while the racemic mixture does so in the opposite direction. Second, incubation with reference buffer showed significant dissymmetry. No dissymmetry was expected for the buffer solution, which suggests that dissymmetry may come from a source other than molecular binding.

Extinction average shifts showed the same trend as for CD. Enantiomeric shifts were comparable and very significant ($\sim 35nm$) for such a small molecular system. The racemic mixture shift was still significant ($\sim 15nm$) for binding to be considered, but it was much lower than that of the enantiomers. Therefore, there is at least one factor that reduces the binding efficiency for the racemic mixture. Curiously, a significant shift ($10nm$) may be observed when the buffer solution is incubated on its own, and this shift provides an additional swap towards blue. In terms of the dissymmetry of extinction, an even bigger shift could be detected for the reference buffer than for the molecular bindings. This result supports the idea of another source of shift besides molecular binding. Shifts obtained for racemic sensors also confirm

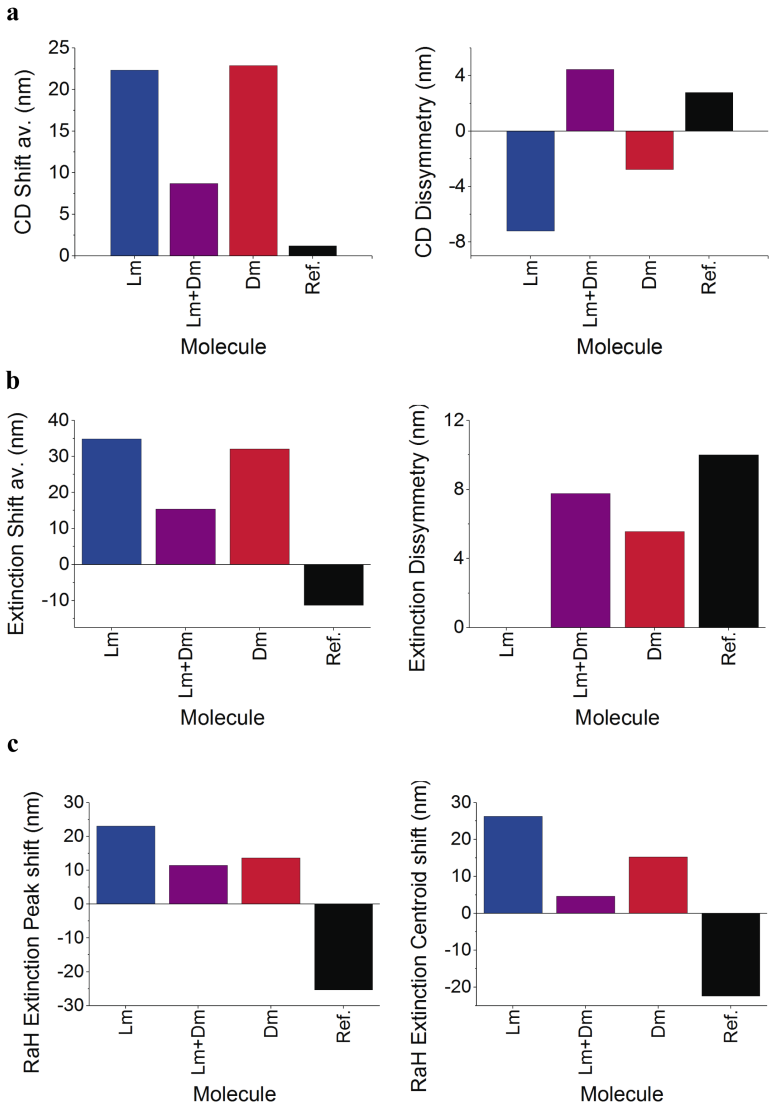

Fig. 4.8 Shift results in the cysteine incubation experiment. a) CD average shift (left) and dissymmetry (right) of enantiomers, the racemic mixture and the reference buffer on left- and right- handed sensors. b) Extinction average shift (left) and dissymmetry (right) for enantiomers, the racemic mixture and the reference buffer on left- and right- handed sensors. c) Peak (left) and centroid (right) shifts for gammadion racemic sensors.

the existence of a buffer-induced shift. In fact, considering that this is a shift towards blue, it may be related to structure annealing[103]; however, this effect is not obvious in such complex structures.

There is no clear evidence of chiral discrimination in the results obtained. However, the lack of consistency between the measured shifts suggests that there may be some interference during the binding. The significant contribution of the buffer solution to CD dissymmetry and extinction shifts suggests that solvent annealing plays an important role in the process. Although not reported extensively, annealing is known to induce morphology changes in nanostructures, thus altering their spectra[103, 109, 110]. Consequently, we are observing the effect of molecular binding in combination with the annealing of plasmonics structures. Therefore, there is clear justification for using microfluidic experiments to accurately monitor binding dynamics.

4.3.2 Microfluidic LSPR tracking

To develop a deeper understanding of cysteine binding to plasmonic sensors, we performed experiments in a microfluidic environment. We measured the changes in spectra by monitoring the peak shift in very short time periods (<1'). Additionally, sensors were subject to very similar experimental conditions because of the accurate sample volume and time control provided by the set-up. None of the benefits from previous experiments was lost in the microfluidics experiments.

We performed experiments to analyse the binding of cysteine enantiomers and their racemic mixture to fully handed and racemic gammadion sensors, using the chip depicted in Figure 4.2b. Every channel in the chip included a full set of sensors; only one solution was injected in every channel. One of the channels in the chip was devoted to checking the effect caused by the buffer solution on the sensors under identical conditions to those of molecular binding. To reduce the effects of annealing on the sensors, we first injected phosphate buffer ($100mM$) into all channels for 1

h, and then injected the cysteine solutions (82.5mM concentration). Finally, the channels were rinsed with phosphate buffer to remove non-bound molecules.

Figure 4.9 shows a plot of the positions of extinction and CD peaks over time. LCP and RCP light illuminations are plotted to show extinction peak shifts, in order to prove that the curves are equivalent, and therefore that the analysis may be applied to any of them. CD curves were relatively noisy when compared to extinction curves, and they eventually grew against background noise. However, similar trends were clearly distinguishable for the CD response of enantiomers, whereas no response was observed for the racemic mixture. Analysis of the extinction curves, which showed less background noise, revealed several interesting features. First, racemic sensors were more sensitive than fully-handed sensors: the total shift for racemic sensors was about 12nm, whereas that for fully-handed sensors was around 8nm. However, all sensors showed the same tendency in terms of molecular binding. Second, enantiomers bound, whereas the racemic mixture did not; we observed a shift for L- and D-molecules, but not for the racemic mixture. Third, each enantiomer has different binding dynamics. L-molecules show a faster binding rate at the beginning of the process, while D- molecules show an initially slower rate that evolved over time; at the end, similar levels were reached.

This is a subtle dynamic effect. In particular, right-handed sensors showed a shift flip of a D-molecule over an L-molecule along the binding step. No flip occurred in the left sensor. The results were more obvious for racemic sensors, as the final shift is not equal for both enantiomers. The slower pace of D-molecules position their shift 2nm below that of L-molecules. This is a very relevant observation, as the final result is therefore time-dependent. This means that, eventually, results could change their sign depending on the incubation time. Finally, no shift was detected for the reference buffer, which, in principle, dismisses annealing interferences and confirms that no binding is obtained in the racemic mixture.

Figure 4.10 shows extinction and CD spectra obtained before and after cysteine binding. As can be easily appreciated, shifts are smaller than those obtained in incubation experiments, and therefore little information can be retrieved from direct observation of the spectra. Qualitatively, we observe an overall decrease in magnitude

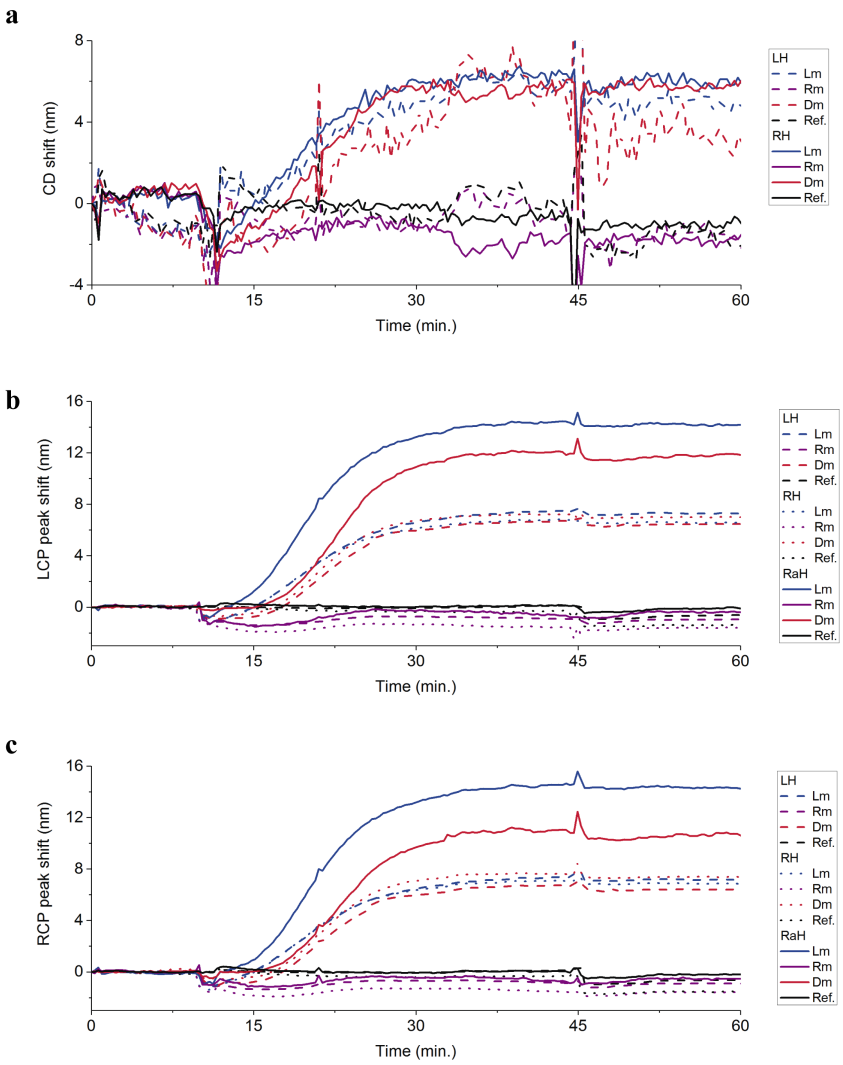

Fig. 4.9 Plots showing the shift in resonant peaks. Peak position for CD and extinction is measured continuously over time for left-handed (LH), right-handed (RH) and racemic-handed sensors (RaH) reacting to cysteine molecular species: left (Lm), right (Rm) and racemic mixture (Rm). a) Shift in CD peaks; b) left circularly polarized illuminated extinction shift; and c) right circularly polarized illuminated extinction shift. Molecular solution concentration: 82.5mM.

in the spectral peaks after binding. The CD spectra of racemic sensors did not show an obvious trend that enabled discrimination, and extinction spectra showed a multi-peak shape even before binding. The initial buffer pre-conditioning appears to affect the sensor such as to make it possible to achieve smaller binding shifts. This further supports the hypothesis that buffer annealing of sensors makes an important contribution to the total shift.

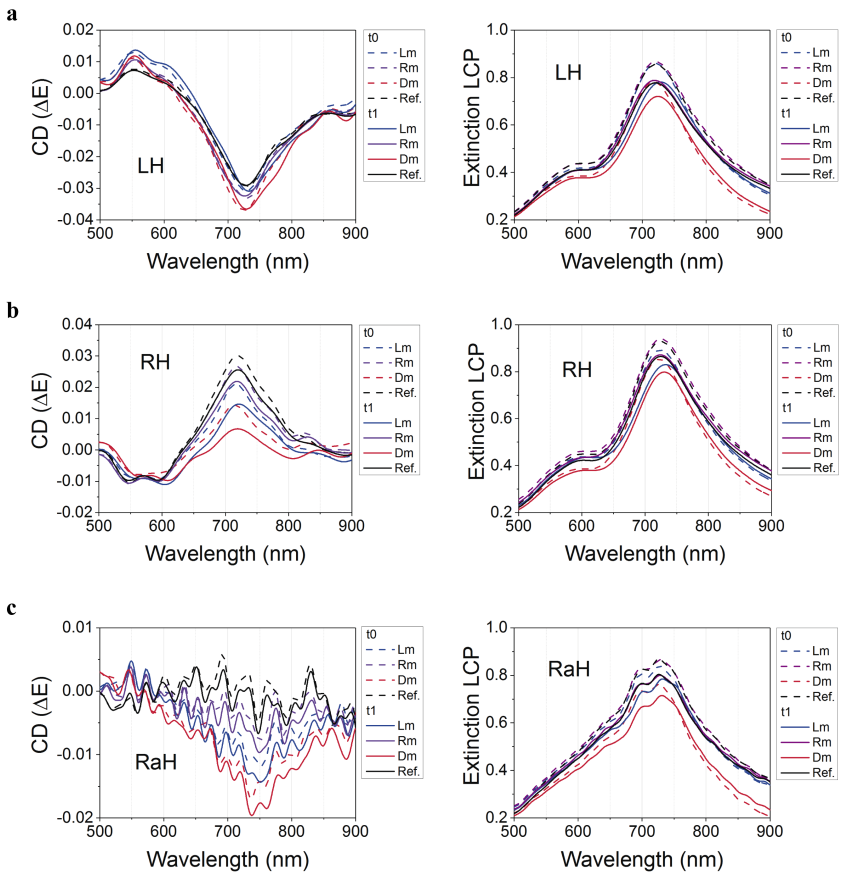

Fig. 4.10 Spectral plots for the microfluidics experiment involving the binding of cysteine species, taken before ($t0$) and after ($t1$) molecular binding. CD (left) and Extinction (right) spectra are shown for cysteine L-enantiomer (Lm), cysteine D-enantiomer (Dm), and the racemic mixture (Rm) of cysteine enantiomers for the three different gammadion sensors: left-handed (a), right-handed (b) and racemic (c).

To obtain further insights into these results, I plotted the average shift and dissymmetry for CD and extinction measurements of each sensor (Figure 4.11). The continuous acquisition mode allows us to obtain statistical data, calculated from 10-20 sequential acquisitions (3'-6' in time) taken on a flat region of the curves, before ($t0$) and after molecular binding ($t1$).

The average CD shift increased by $\sim 6nm$ for enantiomers and decreased to $-1nm$ for the racemic mixture. The opposite trend was found for dissymmetry, which showed similar results to those obtained in the incubation experiment. However, dissymmetry values included large experimental errors, apart from fluctuations from the initial state. Reference buffer measurements were low for the average shift, but significant for dissymmetry, which confirms that dissymmetry is sensitive to minor degradations in the sensors. The overall tendency is reproduced by the extinction average shift and dissymmetry, which show more accurate values than those for CD, but of the same order of magnitude. A similar scenario is observed for the racemic sensor, although only the extinction shift can be measured. The shift showed a difference of about $2nm$ between enantiomers, while no shift was detected for the racemic mixture or for the buffer.

As in the previous experiment, these results were not conclusive. CD shifts and dissymmetry are of a different order of magnitude for different enantiomers, but no opposite dissymmetry is obtained. In addition, the values obtained for the racemic mixture could not be used as a baseline for those of enantiomers, thus validating chiral discrimination. However, extinction results confirmed the absence of binding in the racemic mixture, which made it impossible for measurements on enantiomers to be validated or discarded. Additionally, the absence of a buffer effect in extinction shifts increases the reliability of the bindings. As for racemic sensors, their higher sensitivity makes them more interesting for binding analysis, although they do not currently provide a good signal for chiral discrimination.

These experiments provide additional support for the liquid-annealing hypothesis. The coincidence of the shift magnitudes for the racemic mixture and the buffer, both in this experiment and in the incubation experiment, strengthens the hypothesis that

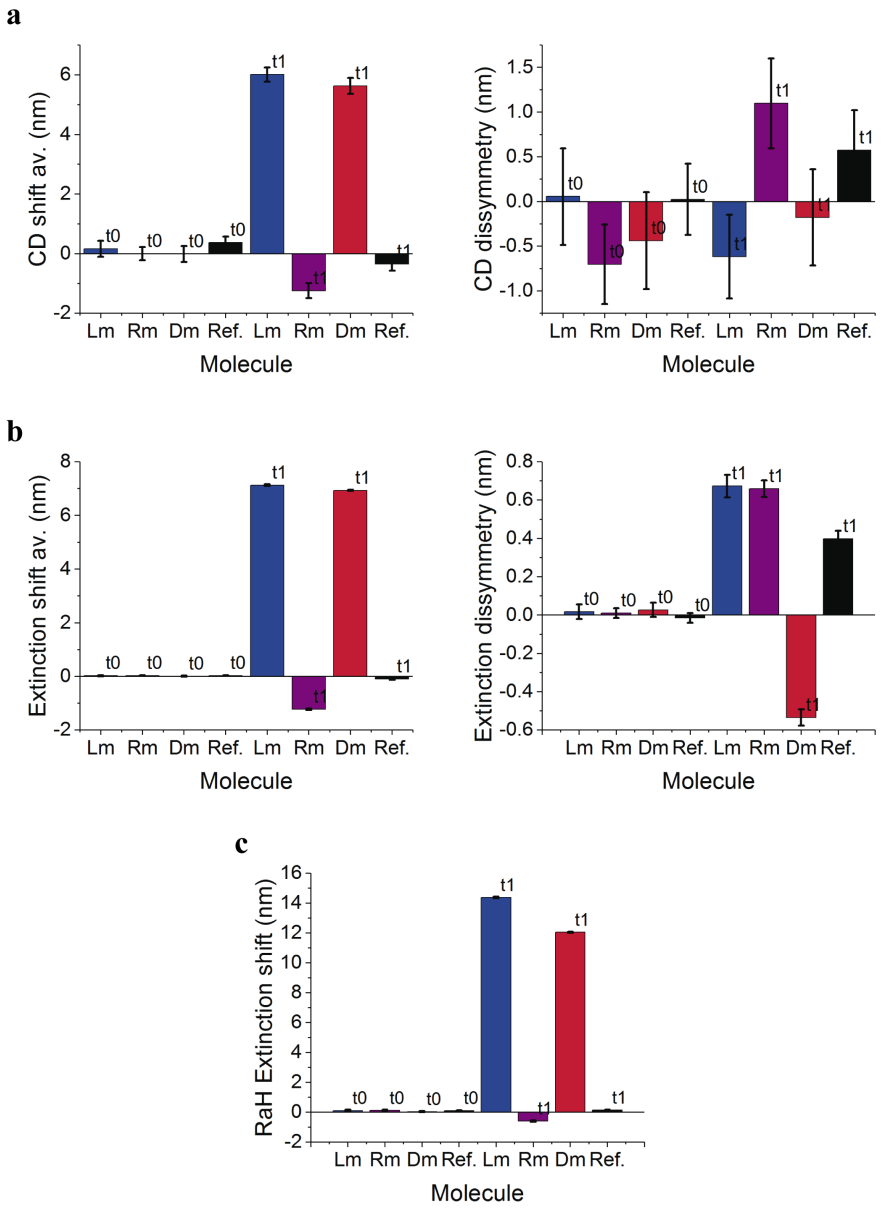

Fig. 4.11 Shift for cysteine binding to gold chiral sensors in a microfluidic environment. Shift average and dissymmmetry are shown for a) CD and b) extinction. c) shows the extinction peak shift for the racemic sensor.

liquid annealing has a significant influence on the measured quantities. In particular, dissymmetry quantities are very sensitive in this regard.

Additionally, the different binding dynamics showed by L- and D-enantiomers presents new questions about the evolution of signals during molecular binding. In that sense, racemic sensors shown better sensitivity, which makes them good candidates for further study of this phenomenon.

4.3.3 Microfluidic LSPR stepped binding

Understanding the different binding dynamics exhibited by cysteine enantiomers, which could ultimately alter the results obtained depending on incubation time, we performed another set of microfluidics experiments to characterize this effect more completely. In this new set, we used a lower concentration of cysteine molecules ($8.25mM$), and the binding process was divided into three partial binding steps. By doing so, we expected to improve the visualization of the dynamics by slowing down the binding rate.

First, buffer was passed through all channels for 1 h, after which we performed three cycles of cysteine-buffer (30' cystenine - 30' buffer; 1 h each). Thereby, the 30'-minute period devoted to cysteine binding in the previous microfluidics experiment was extended to 1.5 h.

Regarding molecular binding analysis, Figure 4.12 shows the peak shifts for left-, right- and racemic-handed sensors to which L-cysteine, D-cysteine, racemic mixtures of cysteine enantiomers, and buffer solutions were added. The slow binding rate helps visualize the different binding dynamics. As in the previous experiment, the binding rate for L-cysteine at the beginning of the experiment was faster than that of D-cysteine. Over the first two cycles, shifts were larger for L-enantiomers than for D-enantiomer. In the third cycle, shifts in L-enantiomers began to saturate, and D-enantiomer shifts overcame those of L-enantiomers, at which point the experiment was concluded. In this experiment, the trends shown by each of the three sensors were found to be more similar, in contrast with the large differences observed previously

for the racemic sensors. However, racemic sensors were still slightly more sensitive, providing larger shifts and molecular shift separations. In line with previous results, no binding was detected for racemic molecules (only bulk refractive index effects were found between steps). On the other hand, shifts were only observed during the first step in buffer solutions, and were higher for left-handed enantiomers. This is probably due to the different time requirements in the pre-annealing step for different sensors/chips.

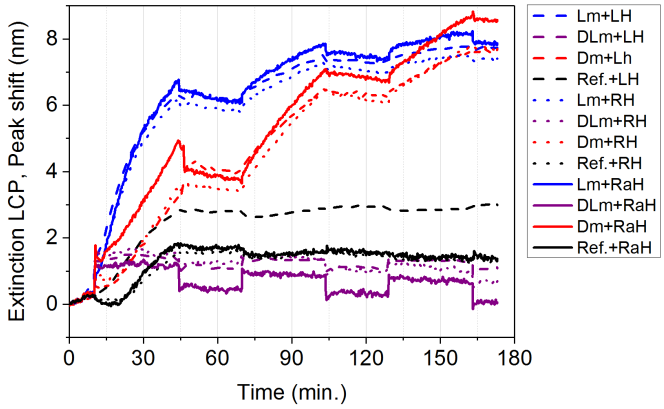

Fig. 4.12 LSPR shift for the different sensors: left (dashed lines), right (dotted lines) and racemic (continuous line) due to L-cysteine molecules (blue), D-cysteine molecules (red), their racemic mixture (purple) and reference buffer (black). The curves show the three binding-rinsing steps.

An alternative view is provided by the spectra depicted in Figure 4.13. Four different spectra are shown in each plot, each depicting different conditions and sensors taken at different time points (at the beginning ($t0$) and after each binding step ($t1-t3$)). Time progression is indicated by the colour gradient). As shown in the plots, the spectral shift progression of D-molecules is slower than that of L-molecules. No shift can be seen for the racemic mixture, and only a slight variation is detected for the reference buffer. Racemic sensors show slightly different spectra than in the previous microfluidic experiments, but they still maintain their peak splitting shape.

To aid interpretation, these results are presented in the bar-plot shown in Figure 4.14. Equivalent results were obtained for averaged extinction shifts (in handed sensors) and racemic sensors shifts. After the first cycle, L-molecules showed

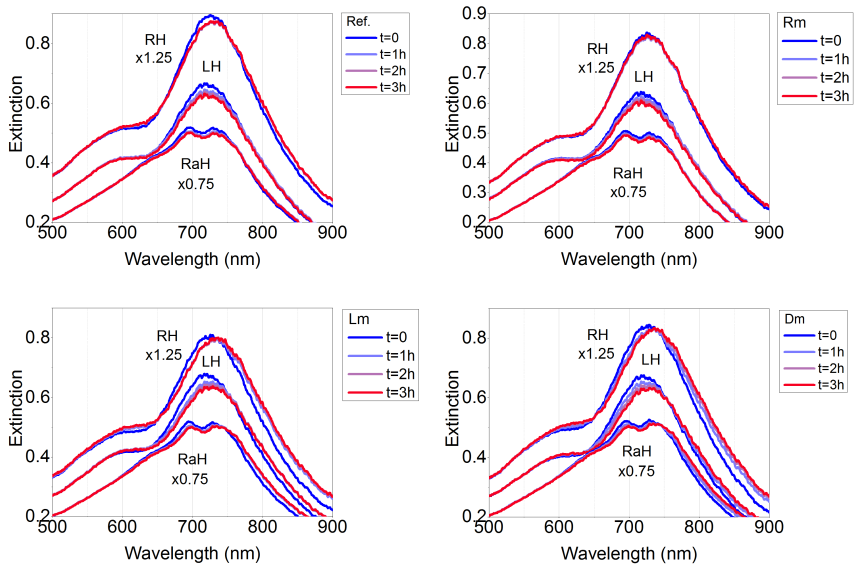

Fig. 4.13 Extinction spectra for the different enantiomers, their racemic mixture and the reference buffer for left- and right-handed and racemic sensors. Very similar magnitudes were observed in each case for the three sensors. For representation purposes, the values obtained for right-handed and racemic sensors were scaled up (25%) and down (25%), respectively. The colour gradient shows the different time measurements taken after every cycle.

a larger shift than that for D- molecules. After the second cycle, the difference between shifts begins to balance out. After the last cycle, the shift for D-molecules slightly overcame that for L- molecules. A much lower but stable shift was observed for the racemic mixture, which confirms the reduction in or absence of binding. Dissymmetry in handed sensors tended towards the previous microfluidics results, where L- and racemic solutions showed positive values and D- solutions showed negative values. Dissymmetry in the racemic mixture evolved from negative to positive values, although the three measurements were found to be quite different when compared independently.

These results highlight the need to accurately control molecular adsorption, since differences in molecular binding dynamics can lead to different results if incubation conditions are not tightly control.

In addition, the reference buffer showed a significant shift and a marked dissymmetry, higher than that obtained with molecular solutions. Once again, we can see that dissymmetry measurement is highly sensitive to buffer.

Separating CD signal results to facilitate data analysis, we observe a similar tendency to that for extinction. Time traces and spectra are shown in Figures 4.15 and 4.16, respectively. L-molecule CD peaks shifted faster than those of D-molecules, and a smaller and constant shift was exhibited by the racemic mixture and the reference buffer. Essentially, we obtained a noise-ridden reproduction of extinction measurements. Consistent with this, spectra plots showed small shifts for enantiomers and even smaller for the racemic mixture and buffer. Dissymmetry cannot be observed from spectra.

Bar plots confirm the previous results: L-enantiomers show larger shifts than those of D-enantiomers, but this advantage is reversed over time (see Figure 4.17). Additionally, dissymmetry plots show several interesting results. First, all analytes follow a constant trend over the three cycles, and only slight magnitude variations may be detected (mostly for the racemic mixture). This is quite an interesting result, as it is decoupled from the extinction trend. In addition, we observe opposite dissymmetry values for L- and D-molecules, and the values obtained for the racemic

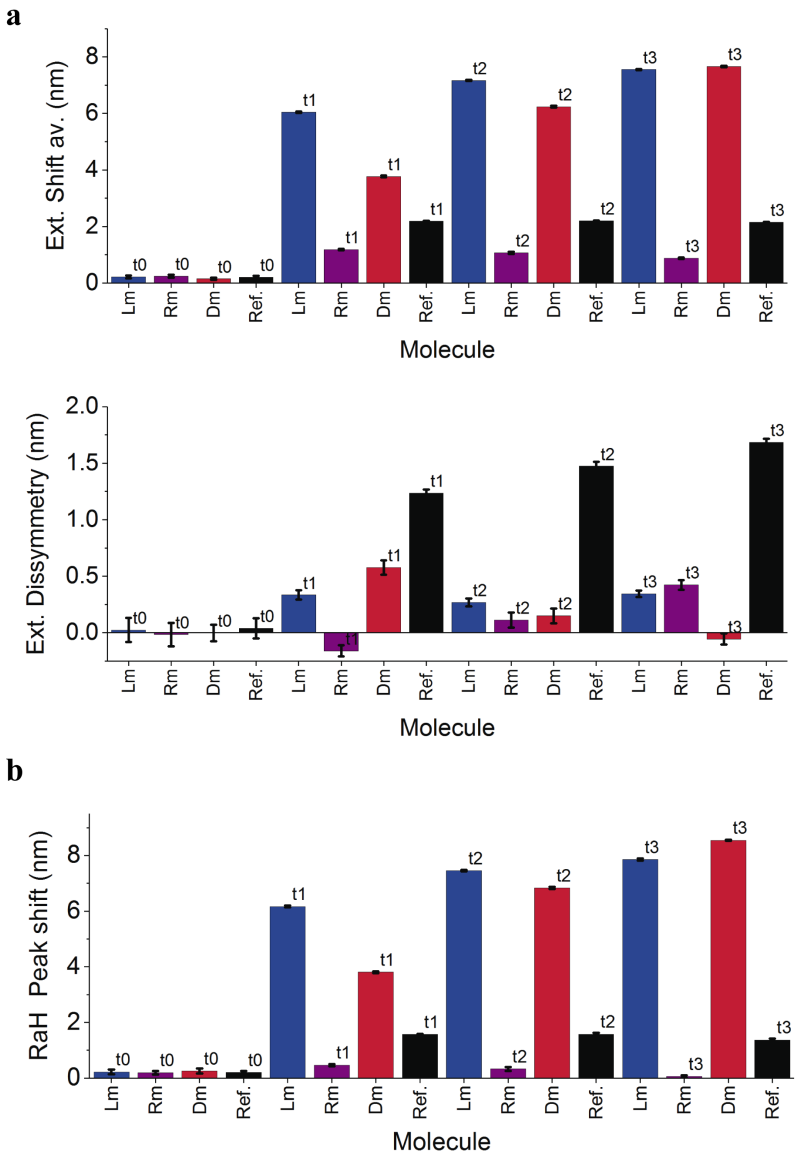

Fig. 4.14 Bar plots of shift for the 3-cycle binding of cysteine to gold chiral sensors. a) Shift average and dissymmetry are calculated for left- and right- handed gammadions, and b) the extinction peak shift is calculated for the racemic sensor. Measurements are taken at the beginning of the experiment in buffer-only conditions ($t0$) and after each cysteine binding cycle ($t1-t3$). Every measurement and its associated error bar were obtained by averaging consecutive acquisitions (≥ 10) at every time position.

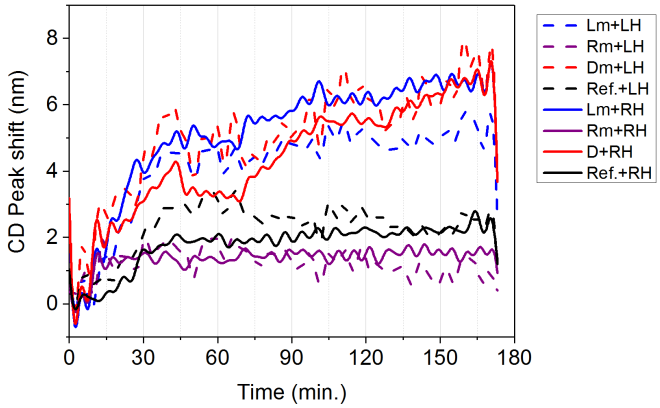

Fig. 4.15 CD peak shift curves for left- (dashed line) and right- (continuous line) gammadion sensors for the 3-cycle binding experiment. The curves show the interaction between the sensors and L-cysteine (blue), D-cysteine (red), the cysteine racemic mixture (purple), and the reference buffer (black).

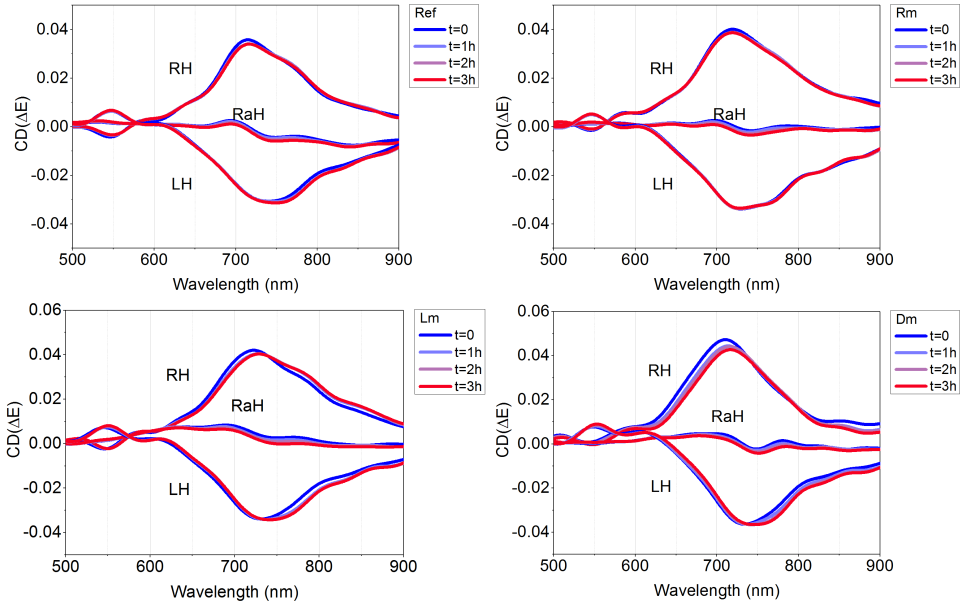

Fig. 4.16 CD spectra for cysteine enantiomers, their racemic mixture and the reference buffer on gammadion sensors at the beginning of the experiment ($t0$) and after the different binding cycles ($t1-t3$). Gradient colours indicate measurements at different time points during the experiment.

mixture oscillated between both values and zero. These results are promising because a clear and coherent set of signals is obtained, which allows for discrimination if the racemic chiral contribution is considered to be zero. However, as did for the previous ones experiments, these results have significant issues: no binding is detected for the racemic mixture in extinction analysis, which means that CD dissymmetry values may not be reliable. Also, there is significant buffer-related shift, and it is not clear how this could affect the binding of different molecules. In fact, dissymmetry values for the racemic mixture and the buffer followed very similar trends.

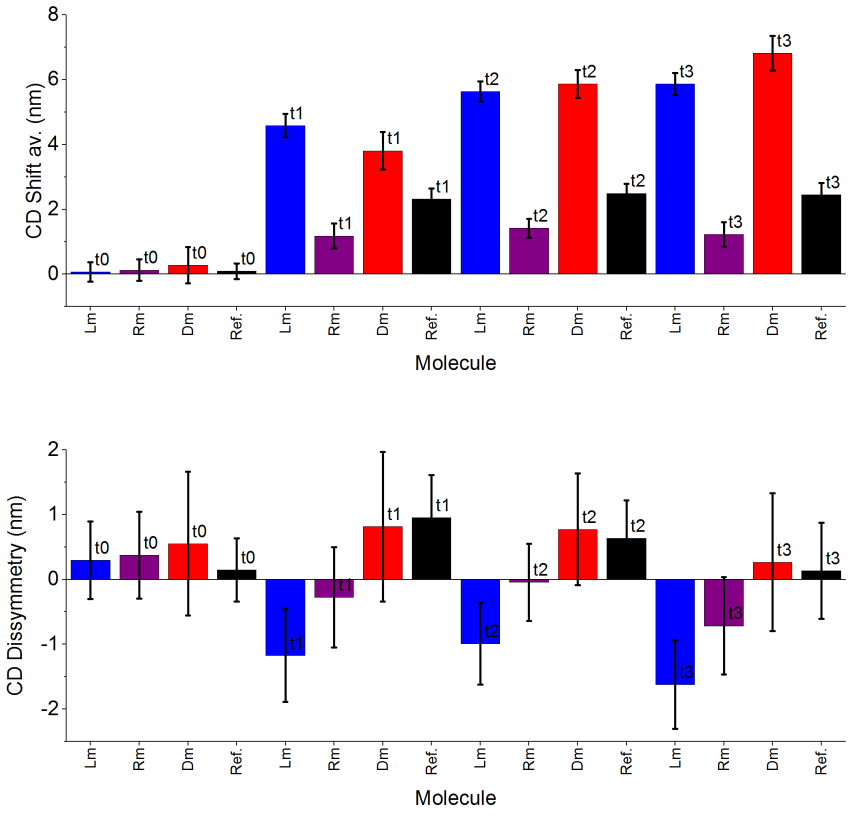

Fig. 4.17 Bar plots for the 3 cysteine-binding cycles on gold chiral sensors. a) CD shift average and b) CD dissymmetry calculated from left- and right- handed gammadion sensors at the beginning of the experiment under buffer-only conditions ($t0$) and after each cysteine-binding cycle ($t1-t3$). Measurement statistics correspond to 10 or more consecutive acquisitions around each time position.

Furthermore, this experiment shows that it may be useful to perform a precise shift analysis using time-trace plots. Otherwise, results such as CD dissymmetry acquired at different time points ($t1$ or $t3$, for example), which show similar values, could have an entirely different interpretation in terms of shift contribution. Therefore, these curves provide us with a clear insight that would be overlooked in single acquisitions.

In summary, the results obtained in the different experiments with cysteine did not show the expected difference in the sign of dissymmetry for gammadion sensors. Consequently, it was not possible to discriminate enantiomers. The binding analysis revealed that the racemic mixture did not bind to the sensors, and so the molecular model did not work under these conditions. This is most probably due to the solution being inactive, since the enantiomers showed nice binding curves. The differences in binding shift kinetics for enantiomers point to a shift swap over time. It is essential to control the circumstances around this time trend, as failure to do so could eventually lead to false or confusing conclusions. In addition, we detected a major drawback of using gold sensors for such sensitive measurements: solvent annealing. The effect of the buffer on the bare sensors was found to be very important for binding and chiral measurements, thus interfering with the signal contribution of cysteine molecules. Despite adding a pre-annealing step, the buffer solution continued to influence dissymmetry, and therefore the chiral discrimination capabilities of the sensing system. The racemic sensors showed very good binding sensitivity, although again chiral discrimination was not possible.

These findings clearly suggest the presence of a molecular change beyond that involving sensor protection from solvent annealing. In the following section, I will analyse an alternative solution.

4.4 Glutamic acid measurements

Glutamic acid, also known as glutamate (anion), is a non-essential amino acid that occurs naturally in its L-form, and is one of the 20 proteinogenic amino acids. Glutamate plays a key role in cell metabolism and is the most abundant fast excitatory

neurotransmitter in the mammalian central nervous system. It is involved in synapse triggering and plasticity, and is believed to have a role in cognitive functions such as learning and memory. Glutamate transporters are found in neuronal and glial membranes. Upon brain injury or disease, an imbalance in glutamate concentration may generate high concentrations of calcium ions inside cells, a process called excitotoxicity that can lead to neuronal damage and eventually cell death. Glutamate-related excitotoxicity is part of the ischemic cascade, and it is associated with diseases such as stroke and Alzheimer's disease. Glutamic acid is also involved in epileptic seizures. Moreover, the hydrochloride salt form of glutamic acid is used as a gastric acidifier[111–113].

In contrast, D-glutamic acid is not produced endogenously in higher mammals. It is found primarily in the cell walls of certain bacteria, and is also present in some foodstuff, such as soybeans. Unlike other D-amino acids, D-glutamate is not oxidized by D-amino acid oxidases, which means that this detoxification pathway may not be used for its disposal. In a similar manner, D-glutamic acid escapes most deamination reactions when ingested (unlike its L-counterpart). Free D-glutamate is found at surprisingly high levels in mammalian tissue, and accounts for 9% of total glutamate in the liver. To date, D-glutamate is considered to be the most powerful natural inhibitor of glutathione synthesis[114, 115].

Glutamic acid has a molecular weight of $147.13 g/mol$ and is water-soluble ($\sim 8 g/L$ at $25°C$). Its enantiomers are commercially available as a white crystalline powder (G1251 Sigma and G1001 Sigma from Sigma-Aldrich). L- and D-enantiomers differ in the exchange between the amino group and the hydrogen bound to the carbon chiral atom. Their electronic resonances can be found in the UV spectral range, with an absorbance peak spanning from deep UV to $190nm$, and a circular dichroism peak at $200nm$. Figure 4.18a shows the molecular formula and its 3D structure representation. The amino group in the chiral centre can be oriented inwards (L-configuration) or outwards (D-configuration). Figure 4.18b shows the absorbance and CD spectra of the molecules and that of their racemic mixture in the UV region.

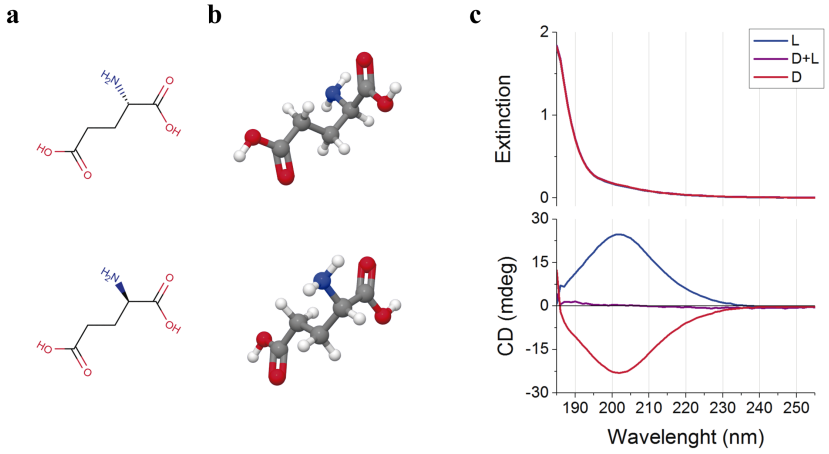

Fig. 4.18 Glutamic acid isomers. a) molecular formula; b) 3D structure representation of L-glutamic acid (top) and D-glutamic acid (bottom). c) UV absorbance and Circular dichroism spectra of L- and D-enantiomers of glutamic acid and that of their racemic mixture.

4.4.1 Microfluidics LSPR on handed gammadion arrays

The next step after the cysteine experiments involved improving sensor stability. To this end, we used a SAM containing MUA to coat the sensors and stabilize their shape, thus making them more robust against liquid annealing. However, such a coating would also prevent the binding of new molecules, so it is necessary to chemically activate the coating in order to capture new molecules. To couple glutamic acid through its amine group, I followed the EDC/NHS protocol described in Chapter 2 (section 2.4.2), choosing glutamic acid instead of cysteine because the cysteine's thiol would compete with MUA. Once again, I tested L- and D-enantiomers and their racemic mixture at a concentration of $67.97mM$.

Phosphate buffer was used as a solvent and reference. This time I used the microfluidic network shown in Figure 4.2b, since a common channel action was required to perform the activation in all channels. Each channel was also individually loaded with one of the corresponding solutions of interest. The three sensors, left-

and right- handed gammadions and racemic gammadions, were integrated into each of the four channels.

The experimental procedure is more complex than the previous one, mostly because of the delicate manipulation required for MUA activation reagents (rather than because of its overall length and number of steps). The EDC/NHS solution has a short lifespan, so it must be prepared right before injection into the chip. The protocol sequence includes two main steps: activation of the sensors' coating and analyte binding. We added conditioning and rinsing steps before and after these two steps, and they were especially short after activation, in order to minimize decay in reactivity experienced by the capture coating. Figure 4.19 shows the peak shift, as a function of time, of extinction and CD spectra for left- and right- handed gammadion sensors. These plots highlight two remarkable aspects: (i) reference signals only drift slightly (as compared to the binding signal); (ii) CD signals are quite noise-ridden when compared to extinction signals. The former was expected because of the SAM coating. The latter implies that the acquisition system is performing poorly. The detected CD noise is caused by mechanical vibrations generated by the automated XYZ positioning stage, which will need to be fixed in the future. Moreover, shifts were found to be very small when compared to the two previous experiments. Only $\sim 1.2nm$ ($\sim 0.7nm$ for glutamic acid) were obtained, compared to $\sim 7nm$ in the cysteine microfluidics environment, and $35nm$ for the cysteine incubation. The shifts were appropriate for measuring extinction variations, but were smaller than desired for the differential analysis of signals, such as those obtained in CD, as shown in Figure 4.19b. However, since there are minimal buffer-induced effects and three solutions were bound correctly, the experiment can be considered satisfactory, even despite the poor trend shown by the CD curves. The most important implications for the CD results is that the values obtained with molecular solutions are above those obtained with the reference buffer, which provides further evidence for signal independence, in contrast to the results achieved with cysteine experiments.

Figure 4.20 shows the CD spectra for the different analyses at the beginning of each experiment ($t0$) and after molecular binding ($t1$). The shifts are clearly very small, when compared to those obtained in previous experiments with cysteine.

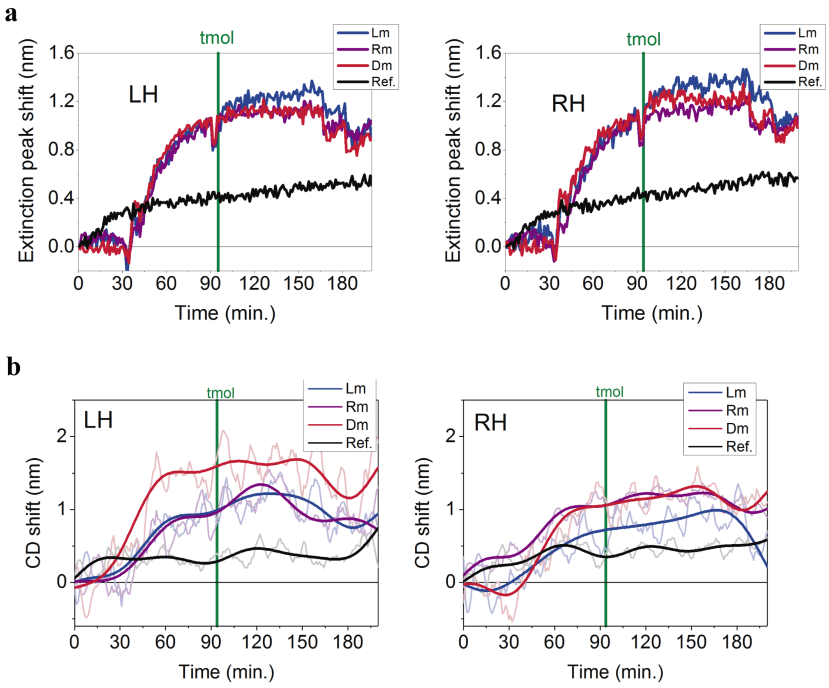

Fig. 4.19 Experimental time traces for glutamic acid detection. a) Extinction and b) CD peak shifts for L- and D-glutamic acid, the racemic mixture and the reference buffer on left-handed (LH) and right-handed (RH) gammadions. The vertical green lines correspond to the delivery time of molecular solutions immediately after the activation step.

Figure 4.20d zooms in on the racemic sensor CD spectra, which was negligible when compared to the CD spectra of fully-handed sensors. Nothing particularly interesting could be seen on the signals beforehand. However, in the following section we will devote a special attention to the treatment of racemic sensor signals.

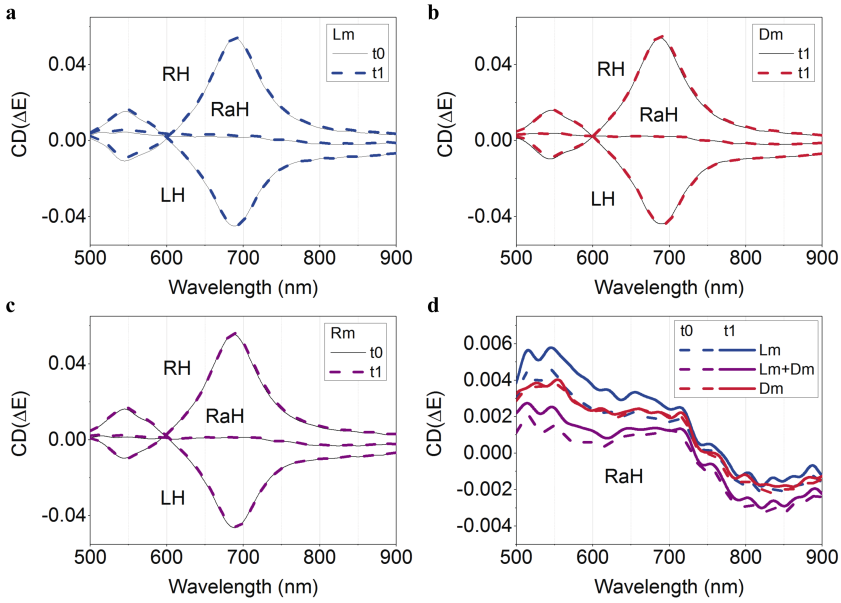

Fig. 4.20 CD spectra of glutamic acid enantiomers (a,b) and their racemic mixture (c) at the beginning of the experiment (t0) and after the binding step (t1) for left-handed (LH), right-handed (RH) and racemic (RaH) gammadions. d) Zoom in on the racemic sensor for the three molecular sensing measurements

To complete the analysis of the handed sensors, I constructed bar plots of extinction shifts and CD shifts (Figure 4.21). The plotted average shift and dissymmetry values and error bar were calculated from the spectra at around t0 and t1 (the time points used in Figure 4.20). In this case, we make the reasonable assumption that the common activation step alters all sensors' response equally, such that the total experimental shift should be proportional to any effect caused by independent molecular bindings.

Extinction average shifts of enantiomers were slightly different in magnitude. The racemic mixture shift was slightly lower, which means that all molecules showed

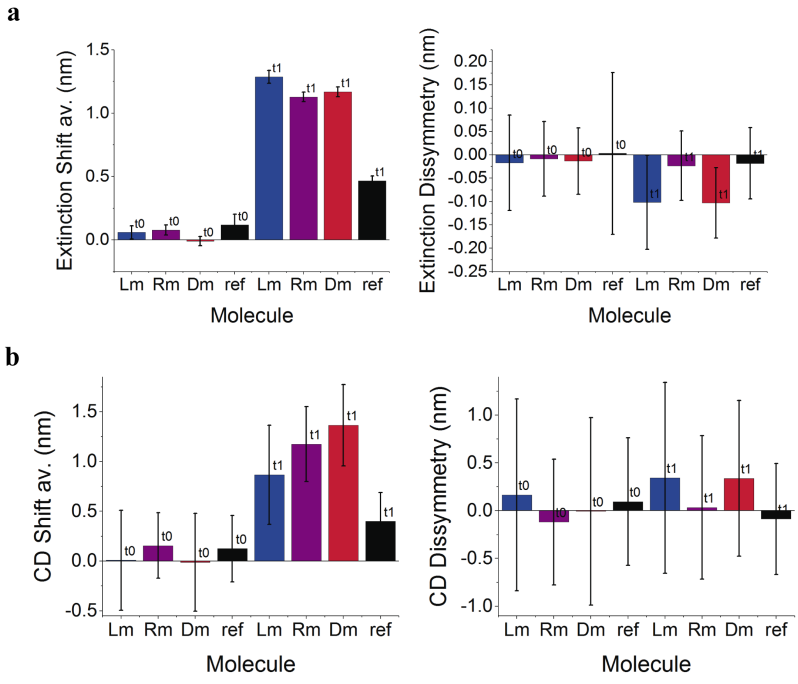

Fig. 4.21 Bar plot of shift average and dissymmetry for a) extinction peak shifts and b) CD peak shifts. Several peak measurements ($\geq$ 10) were averaged at the beginning of the experiment and after glutamic acid binding and used for the calculations.

a similar binding behaviour. The buffer-induced shift is reasonably low, less than half of a molecules' magnitude. In this case, dissymmetry is very low and the calculated error becomes significant.

The average shift for CD spectra shows a larger difference between enantiomers and intermediate values for the racemic mixture, thus providing a properly distinguishable set of values. However, these values were accompanied by large errors that were particularly notable in dissymmetry calculations. Furthermore, dissymmetry had the same sign for both enantiomers, while that of the racemic mixture was around 0, which makes the results uninteresting for the purpose of enantiomer discrimination.

Therefore, we can conclude that fully-handed gammadion arrays do not provide useful results for enantiomer discrimination.

4.4.2 Microfluidic LSPR using racemic gammadions sensors

As shown in Chapter 3, racemic gammadion sensors are a particular case. They show promising properties for chiral sensing in terms of enhancing molecular chiral signals. In this experiment, bindings were achieved for the full set of molecules, in contrast to the cysteine experiments, where the racemic mixture showed no response to the sensing scheme. Therefore, the enhanced CD signal of racemic sensors was treated in a similar manner to that shown in Chapter 3.

The disperse spectra shown in Figure 4.20d show the familiar differential features of racemic sensor enhancement when $t0$ is subtracted from $t1$ (i.e. when the effective molecular contribution is extracted). Results are shown in Figure 4.22. The signal obtained for the racemic mixture clearly shows features that are halfway between those for each enantiomer. A clear, general deviation from baseline is observed, which can be related to experimental limitations that become relevant given the very small signals being measured. The racemic mixture signal was taken as a reference for baseline correction. Consequently, a clear dissymmetric response was obtained

for enantiomers, with an opposite sign after subtraction. CD spectra for the racemic sensor provide evidence of molecular handedness.

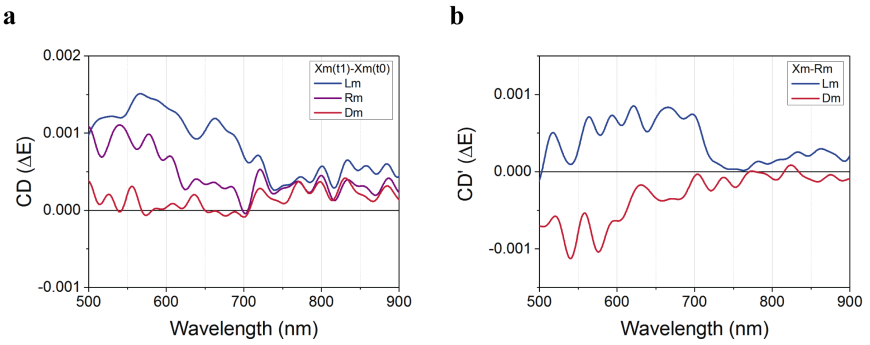

Fig. 4.22 Enhancement signal for glutamic acid using racemic sensors. a) CD response of racemic sensors to L-enantiomers, D-enantiomers and their racemic mixture. The enhanced response has been calculated as the difference in CD before (t0) and after molecular binding (t1). b) CD enantiomeric response correction. The racemic mixture signal has been subtracted from L-enantiomer and D-enantiomer signals. Signals were averaged using 10 sequential acquisitions and then smoothed.

Figure 4.23 shows the extinction peak shift for racemic arrays. These shifts provide interesting information beyond binding confirmation. They show a split during the binding step that reproduces the results obtained for the averaged CD shift, which showed increasingly larger shifts for L-, racemic and D-solutions, respectively. However, the split disappeared after rinsing. This could be related to chiral enhancement caused by the bulk solution rather than by the monolayer of molecules. As shown in Appendix 1 the major contribution to chiral enhancement provided by racemic sensors stems from the volume between gammadion arm gaps, rather than from the gammadion surface. Though rare, the extinction shift seemed to show chiral sensitivity. As for the buffer, it maintained a lower shift, with no risk of interference.

In addition to the analysis of the regular extinction shift, we also exploited the particular tendency shown by the molecular system. We considered the racemic mixture curve to be a baseline; subtracting it from the curve for each enantiomer (see Figure 4.24), we obtain two interesting time traces. Corrected time traces for L- and D-glutamic acid showed a signal that was different from zero only while

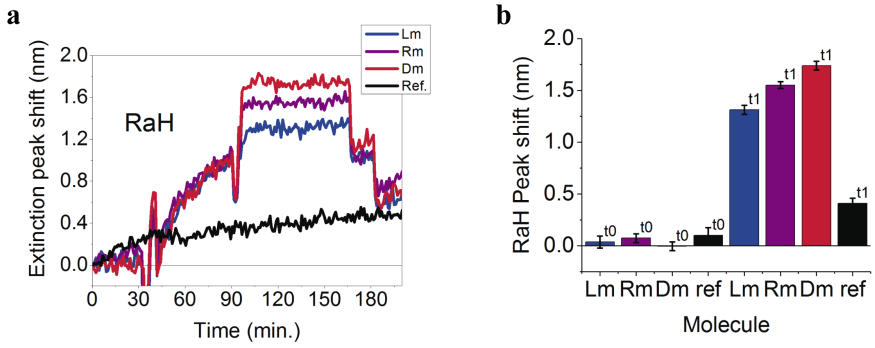

Fig. 4.23 Sensing plots for racemic gammadion sensors. a) Extinction time traces and b) shift plot bars for L- and D-glutamic acid, their racemic mixture and the reference buffer.

the molecular solution was flowing. As if it were a chiral signature, this effect reinforces the fact that phenomena emerged from the bulk influence rather than from the monolayer. While we do not yet have a clear enough understanding of this phenomenon to claim chiral sensitivity in the extinction signal, this result is interesting enough to perform further research on the properties of racemic sensors.

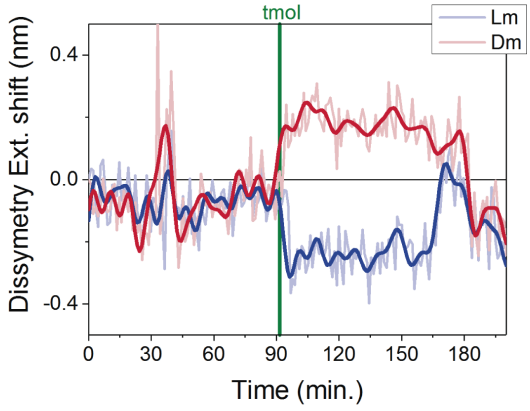

Fig. 4.24 Racemic gammadion time traces for L- and D-glutamic acid after extracting the contribution of the racemic mixture.

Conclusion. We have demonstrated cysteine binding on bare gold plasmonic gammadion sensors. We performed a detailed study of the process using either continuous peak shift time traces or strategically selected spectral acquisitions. The results obtained provide new insights into the importance of binding kinetics and annealing contributions in the final results. The results are sensitive to the incubation time or buffer pre-treatments used, which creates a risk of incorrect interpretations. Moreover, buffer-annealing-induced shifts have been shown to be particularly important for dissymmetry measurements, thus obscuring chiral detection results. Therefore, for these sort of experiments it would be advisable to perform dynamical binding/adsorption studies, or to repeat the experiment to obtain reasonable statistics, instead of making repeated measurements of the same sample.

We also performed experiments with glutamic acid and showed that sensor function reduces the effect caused by buffer annealing drift. However, peak shifts in molecular sensing were reduced as a consequence. The small shifts observed were close to the resolution limit of the system for CD signals, highlighting the need to revise the experimental system to reduce noise. Despite CD noise, the results obtained were generally coherent for the three glutamic acid solutions. Fully-handed gammadion sensors showed a different average CD shift, but its chiral nature could not be confirmed by their dissymmetry, as it was found to show the same sign for both enantiomers. Interestingly, the racemic gammadion extinction shift reproduced the averaged CD shift result obtained with fully handed sensors. Additionally, under analogous processing conditions to those used in Chapter 3, the CD enhancement of racemic gammadions showed the dissymmetry between enantiomers, which confirms the outstanding discrimination properties of racemic sensors. This result led us to calculate time traces of dissymmetric extinction shift, which were shown to be sensitive to the chiral properties of the analyte.

5

Overcoming diffusion-limited biosensing by electrothermoplasmonics

Abstract. Biosensing based on optical micro- and nano-resonators integrated in a microfluidics environment is a promising approach to lab-on-a-chip platforms capable of detecting low concentrations of analytes from small sample volumes. While sensitivity has reached the single molecule level, in practice, the applicability to real-life settings is limited by Brownian diffusion of the analyte to the sensor surface, which dictates the total duration of the sensing assay. Here, we use the electrothermoplasmonic (ETP) effect to overcome this limit through opto-electrical fluid convective flow generation. To this end, we designed a Localized Surface Plasmon Resonance (LSPR) sensing chip that integrates ETP operation into state-of-the-art microfluidics. First, we optimize and characterize the ETP dynamics inside the microfluidic chamber, showing high fluid velocities. Then, we perform proof-of-concept experiments on model immunoglobulin G detection to demonstrate ETP-enhanced biosensing. Our results demonstrate the synergetic effect of temperature

and electric field proving that ETP-LSPR has improved performances over standard LSPR.

5.1 Introduction

The unique optical properties of integrated micro- and nano-optical resonators play a significant role in a wide range of scientific and technological areas, ranging from information processing and coloring to biomedicine[2, 12, 116–121]. Particularly, in the field of biosensing, resonant plasmonic nanostructures have led to promising sensing capabilities, with sensitivity levels that can be pushed down to the detection of single molecule binding events[9, 122, 70, 123, 124]. Furthermore, the combination of localized surface plasmon resonance (LSPR) biosensing with microfluidic technology[125, 126] has recently allowed the implementation of elaborate lab-on-a-chip sensing assays[127, 64, 128, 65]. However, this technology, like all sensing schemes based on quasi-planar transduction schemes, faces a bottle neck due to Brownian diffusion-limited dynamics inside microfluidic channels[129, 130, 24, 25] which places a limit to the analyte binding rate to the sensors and hence the duration of the assay.

Different approaches have been proposed to overcome diffusion-limited transport in LSPR-based sensing schemes. On the one hand, previous studies have shown that strong temperature gradients created around resonant plasmonic nanostructures can lead to convections flows in the surrounding fluid[131, 132]. While such light-induced convections could potentially be used to alter laminar flows throughout a microfluidic channel, they are associated with high temperatures of the metallic nanoparticles, which are incompatible with most biosensing assays which typically involve temperature sensitive biomolecules. On the other hand, electrokinetic phenomena like dielectrophoresis and electroosmosis[133] can also be used for active flow manipulation. Both AC and DC schemes have been shown to lead to efficient micro-mixing[134] inside microchannels, but face several drawbacks that make them inappropriate for biosensing. For instance, they typically require high elec-

tric fields, which greatly complicate their implementation into portable systems. Additionally, approaches based on induced-charge electrokinetic phenomena only work for low ionic strength[135], thus, compromising the stability of biomolecules. Furthermore, some of the aforementioned techniques involve complex geometries and asymmetric features of the microchannels, considerably complicating the fabrication procedures[134]. Recently, a promising electro-optical technique based on the creation of an electrothermal flow[50, 136], coined as electro-thermo-plasmonic (ETP) effect[137], has been used to load on-chip plasmonic traps[138–140]. In this approach, local heating of plasmonic nano-structures creates a local change in the electric conductivity of the fluid which, under an electric field generated by two planar parallel electrodes, leads to flow vortices that span over $100\mu m$ and particle speeds in the range of tens of $\mu m/s$.

In the present work, we demonstrate for the first time that the ETP effect can be implemented in a biosensing assay to overcome the diffusion limit and boost the detection performance. We designed and fabricated a microfluidic LSPR sensing chip with ETP flow control. We first optimize the ETP-induced convection in a microfluidic setting using microparticles as tracers to observe the pattern of the induced flow and compare it with electrohydrodynamics numerical simulations. We then demonstrate how this effect can be used to benefit LSPR sensing. In particular, our experiment shows that ETP-enhanced LSPR reduces duration of the assay and enables reaching larger resonance shift.

5.2 LSPR microfluidic chip with ETP flow control

The platform we use in this work (Fig.5.1) leverages on the LSPR microfluidic chip presented in ref.[64] to which we added a pair of planar electrodes used to activate the ETP effect. The electrodes are made of $1.1mm$ thick borosilicate substrate coated with $100nm$ of ITO ($2 \cdot 10^{-6} ohm \cdot m$ resistivity), faced by the ITO side and separated by a $50\mu m$ double layer adhesive film that seals the sensing microfluidic layer. The

bottom electrode hosts the plasmonic nano-structures while the top electrode is connected to a second microfluidic layer for flow control.

The plasmonic sensor consists of a 2D periodic arrangement of gold nano-rods fabricated by electron beam lithography and reactive ion etching. The gold nano-rods have dimensions of $160x120x75nm^3$ (Length*Width*Thickness) and are assembled in a square array of $120x120\mu m^2$ with $400nm$ pitch. These parameters confer them a transversal extinction peak at $785nm$ that we excite to induce heating and a longitudinal peak at $850nm$, used for sensing (see Fig.5.1). The microfluidic architecture of the chip consists of three functional layers: On top, a control layer with the control valves, at the middle the flow distribution layer with the inlet and outlet channels to distribute the reagents, and finally, at the bottom, the sensing layer with a single $300\mu m$ wide channel that flows the liquid to the sensors. The control and flow layers were made by standard PDMS molding and assembling processes[28, 141], while the sensing layer was patterned by laser engraving.

5.3 Experimental setup

The assembled ETP chip is operated and optically interrogated by a dedicated transmission optical set-up. A pneumatic pump operates the micro valves of the control layer and pushes the reagent through the flow channels. The ETP electrodes are powered by an AC signal generator and amplifier. Local temperature gradients are created by shining a weakly focused $785nm$ laser beam on the plasmonic nano-rod array (linearly polarized along the transverse resonance) [131]. Along the same optical path, a white light source linearly and cross-polarized to the heating beam excites the longitudinal resonance of the nano-rods. Light transmitted through the sensor is collected and analyzed by a microspectrometer. The spectral signal is acquired in real time and peak tracking is used to monitor spectral shift associated to molecular binding to the sensor.

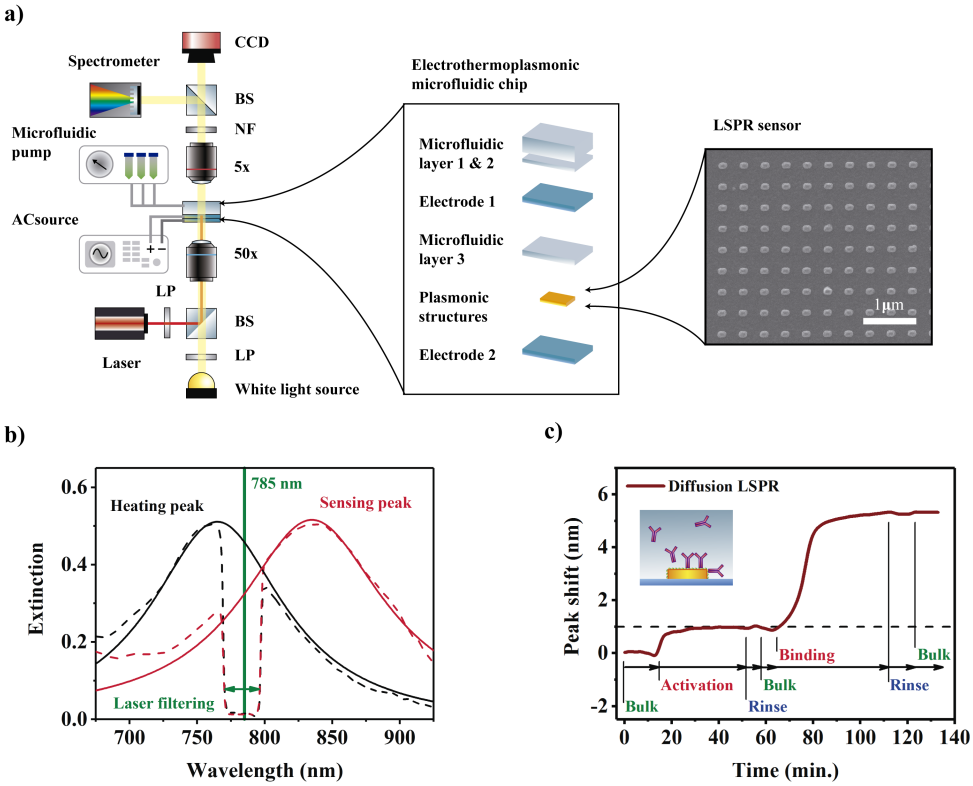

Fig. 5.1 Overview of the on-chip ETP-enhanced LSPR biosensing experiment. (a) Schematic representation of the experimental setup and details of the LSPR chip. The microfluidic chip is mounted on a translation stage to position the sensing region at the focus of a 50x objective (Olympus LMPLFLN50x). A 785*nm* CW laser and a white light source are linearly and cross-polarized with respect to each other using two linear polarizers (LP) and recombined by means of a beam splitter (PBS) before being weakly focused by the objective onto the gold nano-rod array. Transmitted light is then collected by a 5x objective (Olympus LMPLFLN5x), and passed by a notch filter (NF) to remove the heating laser light contribution. Next, a beam splitter (BS) divides the collected light into two paths, one directed to a microspectrometer for spectral analysis and the other one to a CCD camera for imaging. The insets show the structure of the ETP-enhanced LSPR chip along with a scanning electron (SEM) micrograph of a portion of gold nano-rod array. (b) Extinction spectra for each of the linear polarization channels, longitudinal (red lines) and transversal (black lines) with respect to the long axis of the nano-rods. Measured data (dashed line) feature a 30*nm* wide dip around 785*nm* resulting from the notch filter. Solid lines represent a Lorentzian fit that omits the filtered region. (c) Typical molecular binding curve (without ETP effect) acquired with the platform. The activation step aims to prepare the sensor the antibody capture (binding). Bulk steps are intended to separate bulk shifts from the binding shift while the rinse step removes unbound molecules. The inset shows a cartoon representation of the antibody capture on a single nano-rod (not at scale).

5.4 Standard LSPR sensing

Biosensing based on LSPR consists in accurately monitoring the shift of LSPR peak of the sensor during the biochemical assay. Here, we study the binding dynamics of Immunoglobulin G (IgG) antibody as a model biomolecular system. The concentration of IgG ($130fM$) was carefully selected right above the limit of detection of the sensor and below the complete saturation of the sensor in order to evidence the contribution of the ETP effect. We used the results of regular diffusion LSPR as a reference. The plasmonic particles were first coated with a self-assembly monolayer (SAM) made of Mercaptoundecanoid acid (MUA). Amine-coupling protocol through EDC/NHS was used to activate the sensor surface for antibody capture. The sensing assay is defined by the following steps:

$$S1 \xrightarrow{MES} S2 \xrightarrow{EDC/NHS} S3 \xrightarrow{MES} S4 \xrightarrow{MQW} S5 \xrightarrow{IgG} S6 \xrightarrow{MQW} S7 \xrightarrow{MES}$$

where $S1$ and $S4$ are bulk conditioning steps with 2-(N-morpholino)ethanesulfonic buffer (MES) and MilliQ water buffer (MQW) respectively. $S3$, $S6$ and $S7$ are the respective rinsing steps. $S2$ is the SAM activation step and $S5$ is the detection. We do not expect unspecific binding in these experiments, because the simplicity of the protocol and the purity of solutions. Figure 5.1c shows a typical curve obtained from LSPR sensing experiment, where the time required to reach binding saturation is long (about $50min.$) and increases as the concentration decreases. This can be attributed to the low Reynolds number of the system ($Re \sim 10^{(}-2)$) which limits the fluid motion along the channel making diffusion the dominant molecular transport process towards the sensors. In the following, we demonstrate that this limitation can be overcome by generating fluid vortices by means of the ETP effect.

5.5 Characterization of the ETP flow

ETP flow originates from a local temperature gradient that is responsible for permittivity and electrical conductivity gradients in the surrounding fluid. Consequently, the application of an AC electric field (at angular frequency w) produces a body force that leads to the formation of vortices inside the microchannel[50, 137]. For our current purpose, the temperature gradient can be generated by metal losses inherent to the resonant excitation of the gold nano-rods[142, 143, 51]. Interestingly, this body force contains a steady component and one that oscillates at twice the driving frequency $2w$. At high enough frequencies (over $1kHz$ in an aqueous solution), the steady term dominates; therefore an AC field can lead to a net force on the fluid, leading to steady convective flows inside the channel without the drawbacks of DC electric fields[50]. For a given fluid element on a temperature gradient $\nabla T(\mathbf{r})$ and an AC electric field E, the time average electrothermal body force per unit volume in the fluid is given by[50]

$$\mathbf{F}_{ETP}(\mathbf{r}) = \frac{1}{2} Re \left\{ \frac{\varepsilon(\alpha-\beta)}{1+iw\tau} (\nabla T(\mathbf{r}) \cdot \mathbf{E}) \mathbf{E}^* - \frac{1}{2}\varepsilon\alpha^2 |\mathbf{E}|^2 \nabla T(\mathbf{r}) \right\} \tag{5.1}$$

where $\alpha = (1/\varepsilon)(\partial\varepsilon/\partial T)$, $\beta = (1/\sigma)(\partial\sigma/\partial T)$, σ and ε are the conductivity and permittivity of the fluid, respectively, at the angular frequency w. Finally, $\tau = \varepsilon/\sigma$ is the charge relaxation time of the liquid, and its inverse denotes a crossover frequency at which the second term on the rhs of eq.5.1 starts to dominate over the first one, and therefore an inversion on the direction of the flow takes place. This flow inversion is expected to occur above the MHz range for any buffer solution, and we will therefore always consider smaller frequencies of the applied electric field. On the other hand, electrode polarization effects at lower frequencies, which can be safely excluded above a few kHz[53]. Therefore, we considered frequencies in the range 10 kHz to $1MHz$, where we do not expect any significant frequency dependence. As we demonstrate below, this body force can give rise to mixing inside a microchannel at moderate electric field intensities combined with a temperature increase still compatible with biosensing experiments (below $40°C$).

In order to confirm the generation of ETP flow in a microfluidic environment and identify an optimum set of parameters for our biosensing essays, we conducted a systematic experimental study by monitoring the flow pattern via time-lapse imaging of tracer particles. We used an aqueous suspension of $5m$ SiO2 beads as tracers, whose motion was recorded with a CCD camera. Under static conditions corresponding to no flow in the channel, i. e. when the microfluidic pump is OFF (see Fig.5.2a), the ETP effect creates stable vortices that span up to $300\mu m$ in diameter close to the region illuminated by the heating laser (about $60\mu m$ in diameter). These vortices bring the particles close to the nanostructure where they accumulate, exhibiting maximum speeds of up to $\sim 1mm/s$ (calculated from the outer part to de center of the structures was processed via a particle tracing algorithm[144]). Under flow conditions (microfluidic pump ON), both the ETP-induced and laminar flow coexist and lead to an asymmetrical flow pattern. Specifically, the beads from the entire channel cross-section are focused and directed towards the heated region (Fig.5.2d).

To get further insight into the vortex formation inside the microchannel, we performed electrohydrodynamics numerical simulations accounting for both ETP-induced and laminar flows. The parameters of the simulation were tuned by comparing their output with measurements of the velocity of the particles. The ETP flow mechanism is described by two coupled partial differential equations, which have been solved using COMSOL Multiphysics software package:

$$\rho c_P \mathbf{u}(\mathbf{r}) \cdot \nabla T(\mathbf{r}) - \kappa \nabla^2 T(\mathbf{r}) = q(\mathbf{r}) \tag{5.2}$$

$$\begin{cases} \nabla \left[p(\mathbf{r})\mathbf{I} - \mu \left(\nabla \mathbf{u}(\mathbf{r}) + (\nabla \mathbf{u}(\mathbf{r})^T \right) \right] = \mathbf{F}(\mathbf{r}) \\ \nabla \cdot \mathbf{u}(\mathbf{r}) = 0 \end{cases} \tag{5.3}$$

These two coupled equations are the heat transport equation, eq.5.2 and the incompressible Navier-Stokes equations, eq.5.3. In these equations, the material properties ρ, c_P, κ and μ are the volume density, specific heat capacity, thermal conductivity and dynamic viscosity of the buffer aqueous solution, respectively (see the Appendix B for the values used). $T(\mathbf{r})$, $\mathbf{u}(\mathbf{r})$ and $p(\mathbf{r})$ are the spatial temperature, fluid velocity and fluid pressure fields, respectively. $\mathbf{I}$ is the constant 3x3 identity matrix and the superscript T denotes matrix transposition.

The main heat source comes from the region of the plasmonic array illuminated by the heating laser beam. This heat source enters in the problem as a temperature boundary condition with Gaussian distribution, analogous to the laser beam. The volume heat source term $q(\mathbf{r})$ in eq.5.2 represents the heat generated per unit volume inside the fluid domain, which in this case is due entirely to the Joule heating by the applied AC electric field:

$$q(\mathbf{r}) = \frac{1}{2}\sigma Re\{\mathbf{E}\cdot\mathbf{E}^*\} \tag{5.4}$$

where $\mathbf{E}$ is the externally applied AC electric field.

There is a strong bidirectional coupling between both equations. On the one hand, the fluid velocity field $u(\mathbf{r})$ appears in the convective term of the heat transport equation, eq. 5.2. On the other hand, the temperature field $T(\mathbf{r})$ and its partial derivatives $\nabla T(\mathbf{r})$ enter in the total volume body force $\mathbf{F}(\mathbf{r})$ acting on the fluid that appears as a source term in the Navier-Stokes equation, eq.5.3. The total body force can be expressed as:

$$\mathbf{F}(\mathbf{r}) = \mathbf{F}_{buoy}(\mathbf{r}) + \mathbf{F}_{ETP}(\mathbf{r}) \tag{5.5}$$

where $F_{buoy}(T(\mathbf{r}))$ is the buoyancy force that depends on the temperature field $T(\mathbf{r})$ and generates natural convection in the fluid domain. $\mathbf{F}_{ETP}(\mathbf{r})$ is the electrothermoplasmonic body force given by eq.5.1, which is a function of the partial derivatives $\nabla T(\mathbf{r})$ of the temperature field.

The simulations in Fig.5.2b,c predict the formation of large vortices all around the illuminated area. In the absence of external flow, the particles get trapped over the structures moving in and out following vortices with toroidal-like distribution, in agreement with experiments. The simulations also predict the behavior observed experimentally when an externally imposed flow alters the convective vortices induced by the ETP effect. From the top view (Fig.5.2e) we see that all the particles in the channel are brought to the center of the structure following the toroidal vortices. The lateral cross-section view of the flow in the channel shows that as the flow crosses the sensor, the velocity field results on an inflection from bottom to top, in very good agreement with the experimental observation where particles are seen to move out of focus after the center of the sensing array (Fig.5.2f). The presence of this strong

upward flow is not optimal for our sensing application, and will have to be addressed in future developments.

5.6 Biosensing experiments with ETP flow

In order to study the effect of ETP flow in LSPR sensing, we repeat the above mentioned IgG sensing protocol, with the difference that the ETP effect was activated during the binding step. The ETP flow was triggered by $25mW$ of laser power and an electric field of $5 \cdot 105Vrms/m$ at $100kHz$. We chose this frequency because we observed that at this value the velocity measured with the tracer particles featured a slight maximum. The diffusion limited saturation time (50min) and maximum shift ($4.5nm$) are given by a reference experiment in the absence of ETP flow (brown curve). Next, we carried out two experiments under ETP conditions with different durations (Fig.5.4). The first experiment (green curve) was stopped (by interrupting the delivery of antibody and flowing buffer and switching OFF both the laser and electric field) at the precise time needed by diffusion limited transport (i.e. in the absence of ETP flow) to reach binding saturation. Interestingly, when the heating laser and the electric field are switched ON, new features appear in the curves due to the presence of ETP flow. First, a fast blue-shift of about $2nm$ is observed just after the binding step is initiated. This behavior is attributed to the reduction in refractive index of the aqueous solution upon heating, which results in a blue shift in the plasmon resonance peak. Analogously, when the liquid is cooled down, the refractive index increases again and the plasmon resonance red shifts.In the figure 5.3 we show the effect of laser heating in the sensing scheme for different laser powers, i.e. different temperatures.

When the ETP flow is activated during the time needed to reach saturation under diffusion limited conditions, the total red shift at the end of the experiment reaches $10.5nm$, i.e. 2.3 times larger than without ETP effect. The greater shift when using the ETP effect is associated to an increase in the adsorption rate of IgG while maintaining the desorption rate. The second experiment (blue curve) was interrupted

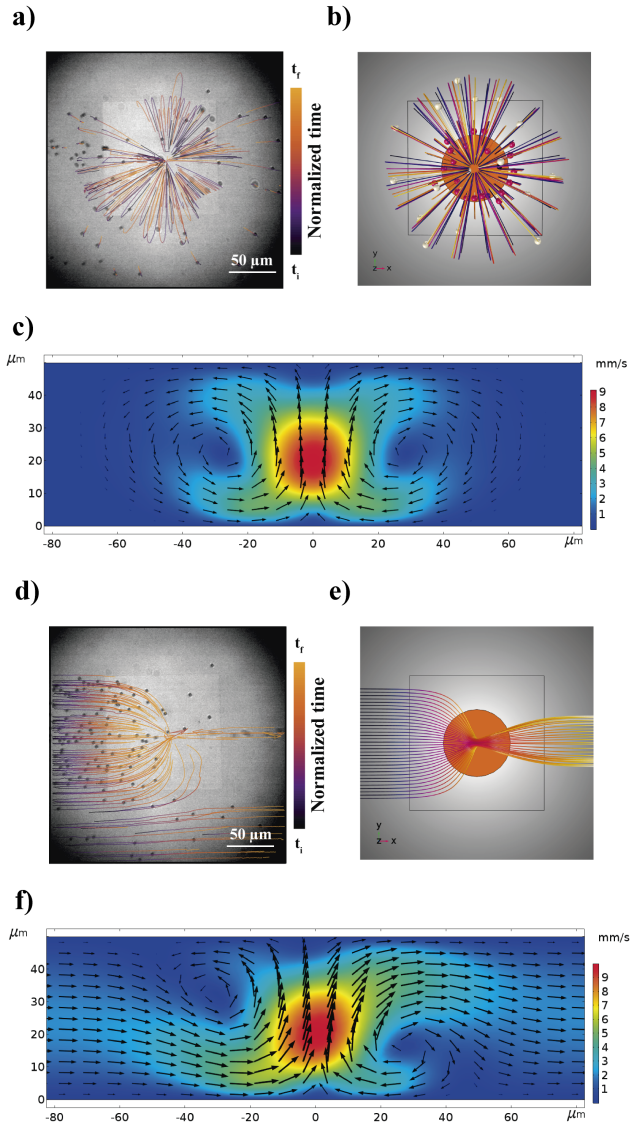

Fig. 5.2 Demonstration of ETP flows generated inside a microchannel. (a) CCD image of the vortices generated under static conditions (microfluidic pump OFF), SiO2 microparticles were used as tracers. The image was obtained combining a set of frames of the video recording (see AppendixB). The lines indicate the trajectories followed by the particles during the video, while the color shading corresponds to a normalized time, indicating the start (ti) and end (tf) of each individual track. The total duration of the recorded trajectories is 10 s. (d) CCD image for flow conditions (microfluidic pump ON). The same processing used in (a) was applied (see AppendixB). (b and e) Simulations of the analogous situations of the experimental demonstrations depicted in (a) and in (b). (c) Simulated fluid flow profile along a vertical cut of the central line of the microchannel for the situation shown in panel (b). (f) Analogous simulation described in (c) but under flow conditions.

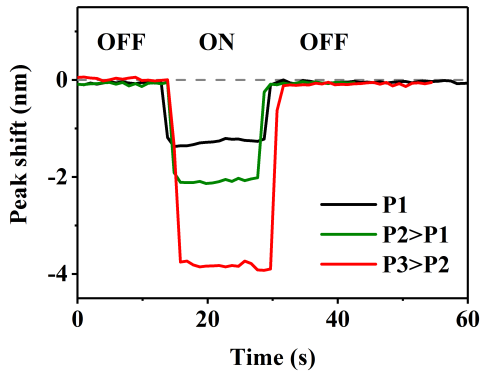

Fig. 5.3 Shift effect originated by laser heating in static conditions. The shift showed to be higher when the laser power is increased, which is attributed to water density reduction hence refractive index reduction.

once the detected shift was equal to the one reached at binding saturation in the absence of ETP flow, accounting for the expected additional red-shift due to cooling of the sensor once laser heating is switched OFF. In these conditions it took 17*min*. to reach diffusions' saturation shift, i.e., the same signal was reached 2.9 times faster than the diffusion limited case. These two experiments demonstrate a substantial improvement of the performance of LSPR sensing, as ETP can be used to either increase sensitivity or reduce the overall time of the assay.

To better understand the dynamics of LSPR sensing under ETP flow, we evaluated the respective contributions of surface heating and applied electric field (see Fig.5.5). Our data show that reducing either the electric field or the heating laser power leads to a performance loss compared to the diffusion-limited dynamics. We have observed that the binding kinetics slows down progressively as the heating laser power is decreased, while maintaining the optimum electric field. At maximum laser power (P=P3 and E=E2)) the sensing performance is clearly improved. Below a certain threshold (P=P1), the sensing performance get worse than without ETP, as can be seen in Fig.5.5a. Similarly, for a given laser power there is a threshold value of the electric field required to observe improvement over the diffusion-limited assay (Fig.5.5b). This may be due to some inhibitory effect of the temperature on the binding that takes place at low electric fields. Eventually, we conclude that neither

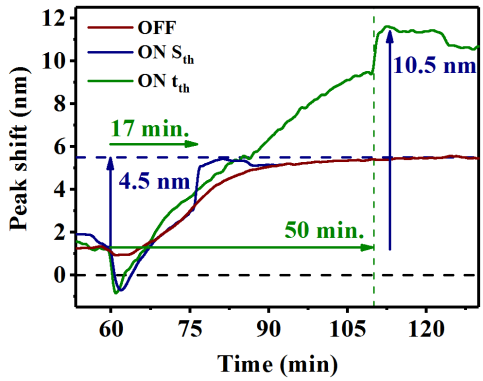

Fig. 5.4 Experimental demonstration of ETP-enhanced LSPR sensing capabilities. Brown line: IgG binding experiment in the absence of ETP flow. Green line: experiment with ETP ON during diffusion limited saturation time threshold t_{th}. Blue line: experiment in which ETP was stopped after the diffusion limited shift threshold S_{th} was reached. The dashed lines represent the benchmarks based on saturation shift (blue) and time (green) for diffusion-limited dynamics.

thermal nor electric field induced flows alone are enough to improve the sensing performance; only a synergetic effect of both contributions enables to overcome diffusion dynamics.

The available instrumentation prevented us from checking higher laser powers and electric fields. In fact, the maximum laser power available (P=P3 fig.5.5a) already shows traces of instability in form of spikes in the binding curve. Nevertheless, one of the major challenges to face is the reproducibility of the properties of the chips, since they are single use and many are needed for set-up optimization and to get a full set of data. In order to reduce dispersion due to some hand-made steps during the fabrication, the chips were produced in small batches. Several sets were tested during the improvement of the platform, giving us confidence about the reproducibility of the observed effects (see additional data set in supporting information). However, these fabrication-related issues could be easily improved in a large scale facility.

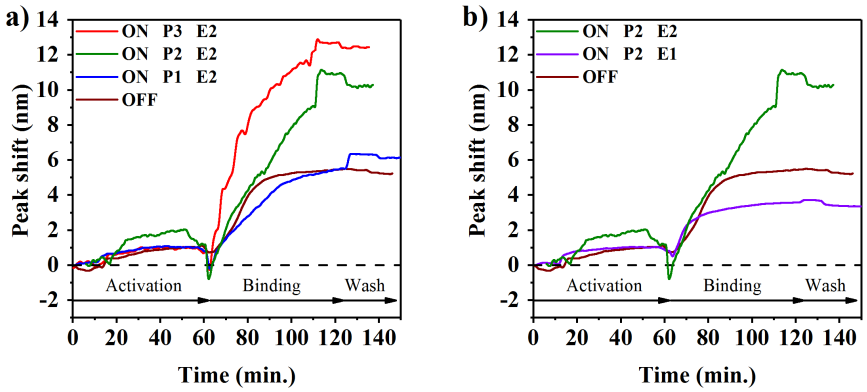

Fig. 5.5 Study of the respective contribution of laser heating and electric field on the IgG binding curve. ON (OFF) refer to experiments performed in the presence (absence) of ETP flow, respectively. (a) Binding curves for different laser power P (P1<P2<P3) at fixed electric field E. (b) Binding curves for different electric fields (E1<E2) at fixed laser power. P1, P2 and P3 correspond to laser powers of 20, 25 and 30mW respectively. E1 and E2 correspond to $3 \cdot 10^5$ and $5 \cdot 10^5 V_{rms}/m$, respectively.

5.7 Results reproducibility

One of the major challenges when working with LSPR detection integrated with microfluidics is the repeatability over the different fabricated chips. The differences in chip characteristics come mainly from the several handmade steps involved in the current fabrication process. Additionally, at the current state of the technology, chips are not reusable and one chip per curve is needed. Therefore, in order to reduce the differences between chips, they were prepared in batches. Following this approach, we achieved good consistency between the results obtained with different chips. High control over the system has permitted us to demonstrate the synergistic effect between the temperature gradient and the electric field, as well as the need for an optimum set of values for both parameters to effectively increase the sensing performance. In order to demonstrate the robustness of our approach, we present an additional set of experiments in Fig. 5.6. These data evidence the reproducibility of the ETP effect on the kinetics of the binding curves, despite being acquired in a slightly different configuration. Indeed, in these chips the transversal resonance of

the rods was used for sensing and the longitudinal resonance for heating, opposite to the data presented in the main text. While a very similar behaviour is obtained, which demonstrates the robustness of the effect, the best performance (in terms of binding speed and maximum shift) is lower compared to that of the main text due to the lower laser power used.

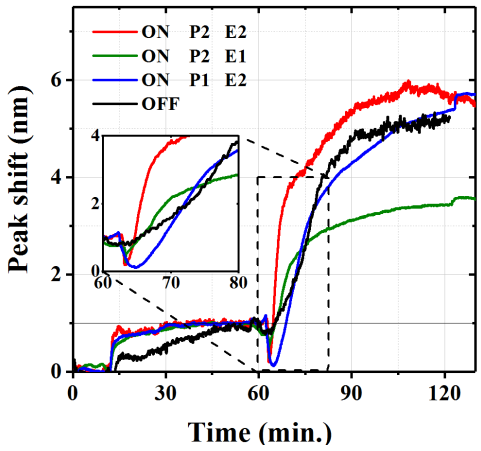

Fig. 5.6 Effect of the laser heating and the electric field on the IgG binding curve. Diffusion limited dynamics are represented by the OFF curve, while ON represents the different curves with ETP dynamics with laser power (P1<P2) and electric field (E1<E2), where $P1 = 7mW$, $P2 = 12.5mW$, $E1 = 3 \cdot 10^5 V_{rms}/m$ and $E2 = 5 \cdot 10^5 V_{rms}/m$. The inset shows the rising part of the binding curves.

Conclusions. In this study, we demonstrated that the implementation of the ETP effect in a microfluidic LSPR chip contributes to improve biosensing performances beyond the diffusion limit, substantially increasing both the binding kinetics and maximum resonance shift. Further control over the ETP-induced fluid dynamics is foreseen to lead to improved capabilities which could greatly impact LSPR-based sensing. While this approach more naturally fits plasmonic sensing schemes, owing to the excellent photothermal properties of noble metal nanostructures, it could be translated to other sensing mechanisms by adapting the activation of local temperature gradients. This experimental demonstration gives rise to new opportunities in the LSPR sensing community, looking for faster and more sensitive platforms.

Conclusions

Abstract. We have explored new plasmonic sensing schemes, combined with state-of-the-art microfluidics and surface chemistry, with an emphasis on enantio-selective biosensing. We addressed the controversy in the chiro-plasmonics community regarding reproducibility, and have focused our efforts on developing robust experimental protocols and reproducible experiments. We have addressed some of the potential drawbacks that affect the reliability of chiral plasmonic sensing, and have proposed alternative strategies to improve performance. We have also worked to solve a general problem concerning integrated sensing schemes in microfluidic environments: the diffusion-limited transport of molecules. We performed proof-of-principle experiments demonstrating that this limit can be overcome using electrothermoplasmonic-induced flows, thus leading to a faster, more sensitive sensing scheme.

In this thesis, we developed a sensing platform combines plasmonic sensors and PDMS microfluidic chips. This allowed us to apply controlled surface chemistry protocols and obtain optical readouts. Using this strategy, we have developed several biosensing scenarios using chiral plasmonics nanostructures, and more reliable protocols than those previously available.

In Chapter 1 I reviewed the fundamental scientific concepts involved in this multidisciplinary project: LSPR sensing, microfluidics, surface chemistry, circular dichroism and electrothermoplasmonics. In Chapter 2 I described the surface chemistry protocols, manufacturing methods, and experimental setups used.

In Chapter 3, I presented the first experimental application of the entire process. We selected amino acids as model chiral molecules because their enantiomers are available; thus, chiral detection can be validated using the two mirror images, while the racemic mixture can be used as a reference. We showed enantioselective detection using gammadion plasmonic arrays distributed in a racemic arrangement. By using racemic sensors, we could directly detect phenylalanine enantiomers by removing the strong circular dichroism background of the gammadion structures by their racemic distribution within the sensors' array. Depositing phenylalanine by thermal evaporation provided a high density coating on the plasmonic hot regions, which allowed us to obtain a clear signal in an opposed direction for each enantiomer; the signal obtained for the racemic mixture was zero.

In Chapter 4, we changed to a microfluidic environment to study the performance of fully-handed gammadion sensors, as well as racemic sensors. We directly bound cysteine to bare gold sensors, and glutamic acid to functionalized gold sensors through an amine linking protocol. We found that bare gold experiments showed large LSPR shift contributions caused liquid annealing of the structures, which interfered with chiral discrimination measurements. While extinction or circular dichroism shifts were in a range that achieved reasonable reliability, their dissymmetry values continued to be sensitive to the reference buffer used in the measurement. Additionally, the experiments performed on functionalized sensors were more robust to the annealing effect, but their binding sensitivity was reduced because molecules were bound through an interfacial layer instead of being bound directly to the sensors. The shifts obtained were smaller, but sufficient to perfectly track extinction signals and discriminate CD trends. However, the analysis based on dissymmetry of the fully-handed sensors was not conclusive for chiral discrimination. In contrast, when we perform an analogous analysis to that described chapter 3, but this time using racemic sensors, the results reproduced the discrimination between the enantiomers.

To exploit LSPR sensing in microfluidics channels, in addition to the chiral experiments, we addressed the challenging problem of diffusion-limited transport in micro-channels. In Chapter 5, we developed and tested a novel three-layer chip architecture and an experimental platform that integrates the electrothermoplasmonic

effect with microfluidics for biosensing applications. Enabling the electrothermoplasmonic effect in the micro-channels introduced toroidal shape-like flows around the sensors, which promoted molecular transport towards the sensors. By systematically monitoring molecular binding through LSPR, we demonstrated that faster and more sensitive dynamics can be achieved with electrothermoplasmonic-enhanced sensing than through regular diffusion-limited sensing.

The results I have presented in this thesis create new horizons in plasmonic chiral sensing, and in plasmonic sensing using microfluidics systems in general. We provide the chiro-plasmonics community with more reliable routes for sensing and with more effective sensors, which paves the way for new systems to be systematically tested, and for new molecular characterizations to be developed. In addition, our work in electrothermoplasmonic-enhanced sensing advances the field toward faster, more sensitive experiments that will push forward the current limits of detection. We hope our project has contributed a further step in this fast, small world.

Outlook

The work presented in this thesis opens new directions in the biosensing field that are foreseen to improve sensing platforms performances and help transferring them towards real life applications.

In the field of chiral sensing our approach based on using a racemic sensor brings a powerful solution to enantio-selective detection with applications in particular to the pharmaceutical industry. Yet, this is still a proof of principle and several directions would need to be pursued to reach a robust platform. First of all, further work should be done on identifying the optimum design of racemic sensors to maximize both sensing sensitivity and enantio-selective discrimination performance. Also, next steps should improve operation in a flow environment which is the most likely configuration to implement in an industrial environment.

As for the use of the electrothermoplasmonic effect to boost the performance of LSPR sensing platforms, there are different directions to be followed. While our experiment showed a clear boost of the analyte binding, the current temperature distribution at the sensor is not optimum as it induces a local depletion of molecules in some regions of the sensing region. Engineering the temperature landscape should enable to greatly improving the binding enhancement. Another important aspect to develop is to make simpler the fabrication of the microfluidic chips which currently involve a long series of tedious steps.

References

[1] Katherine A. Willets and Richard P. Van Duyne. Localized Surface Plasmon Resonance Spectroscopy and Sensing. *Annual Review of Physical Chemistry*, 58(1):267–297, 2007.

[2] Stefan A. Maier. *Plasmonics: Fundamentals and Applications*. Springer US, New York, NY, 2007.

[3] John David Jackson. *Classical electrodynamics*. Wiley, 1999.

[4] Craig F Bohren and Donald R Huffman. *Absorption and scattering of light by small particles*. John Wiley & Sons, 2008.

[5] Hitoshi Kuwata, Hiroharu Tamaru, Kunio Esumi, and Kenjiro Miyano. Resonant light scattering from metal nanoparticles: Practical analysis beyond rayleigh approximation. *Applied Physics Letters*, 83(22):4625–4627, 2003.

[6] K. Lance Kelly, Eduardo Coronado, Lin Lin Zhao, and George C. Schatz. The optical properties of metal nanoparticles: The influence of size, shape, and dielectric environment. *Journal of Physical Chemistry B*, 107(3):668–677, 2003.

[7] Viktor Myroshnychenko, Jessica Rodríguez-Fernández, Isabel Pastoriza-Santos, Alison M. Funston, Carolina Novo, Paul Mulvaney, Luis M. Liz-Marzán, and F. Javier García de Abajo. Modelling the optical response of gold nanoparticles. *Chemical Society Reviews*, 37(9):1792, 2008.

[8] Stefan Enoch, Romain Quidant, and Goncal Badenes. Optical sensing based on plasmon coupling in nanoparticle arrays. *Optics Express*, 12(15):3422, 2004.

[9] Srdjan S. Aćimović, Mark P. Kreuzer, María U. González, and Romain Quidant. Plasmon near-field coupling in metal dimers as a step toward single-molecule sensing. *ACS Nano*, 3(5):1231–1237, 2009.

[10] Boris Luk'yanchuk, Nikolay I. Zheludev, Stefan A. Maier, Naomi J. Halas, Peter Nordlander, Harald Giessen, and Chong Tow Chong. The Fano resonance in plasmonic nanostructures and metamaterials. *Nature Materials*, 9(9):707–715, 2010.

[11] Kathryn M. Mayer and Jason H. Hafner. Localized surface plasmon resonance sensors. *Chemical Reviews*, 111(6):3828–3857, 2011.

[12] Jeffrey N Anker, W Paige Hall, Olga Lyandres, Nilam C Shah, Jing Zhao, and Richard P Van Duyne. Biosensing with plasmonic nanosensors. *Nature materials*, 7(6):442–453, 2008.

[13] Amanda J. Haes and Richard P. Van Duyne. A nanoscale optical biosensor: Sensitivity and selectivity of an approach based on the localized surface plasmon resonance spectroscopy of triangular silver nanoparticles. *Journal of the American Chemical Society*, 124(35):10596–10604, 2002.

[14] Andreas B Dahlin, Jonas O Tegenfeldt, and Fredrik Ho. Improving the Instrumental Resolution of Sensors Based on Localized Surface Plasmon Resonance interfacial refractive index of nanoscale noble metal generic data analysis algorithms and a simple experimen- comparable to that of state-of-the art SPR systems. 78(13):4416–4423, 2006.

[15] Tie Wang, Xiaoge Hu, and Shaojun Dong. The fragmentation of gold nanoparticles induced by small biomolecules. *Chemical communications (Cambridge, England)*, (38):4625–4627, 2008.

[16] Angelika Ku, Trolle R Linderoth, Michael Schunack, and Flemming Besenbacher. L -Cysteine Adsorption Structures on Au (111) Investigated by Scanning Tunneling Microscopy under Ultrahigh Vacuum Conditions. *Adsorption Journal Of The International Adsorption Society*, (111):2156–2160, 2006.

[17] M Duval Malinsky, L Kelly, G C Schatz, and R P Van Duyne. Chain length dependence and sensing capabilities of the localized surface plasmon resonance of silver nanoparticles chemically modified with alkanethiol self-assembled monolayers. *Journal Of The American Chemical Society*, 123(19):1471, 2001.

[18] Tanya Karakouz, Alexander B. Tesler, Takumi Sannomiya, Yishay Feldman, Alexander Vaskevich, and Israel Rubinstein. Mechanism of morphology transformation during annealing of nanostructured gold films on glass. *Physical Chemistry Chemical Physics*, 15(13):4656, 2013.

[19] Todd M. Squires and Stephen R. Quake. Microfluidics: Fluid physics at the nanoliter scale. *Reviews of Modern Physics*, 77(3):977–1026, 2005.

[20] O. Reynolds. An Experimental Investigation of the Circumstances Which Determine Whether the Motion of Water Shall Be Direct or Sinuous, and of the Law of Resistance in Parallel Channels. *Philosophical Transactions of the Royal Society of London*, 174(0):935–982, 1883.

[21] Matthew J Davies, Marco P C Marques, and Anand N P Radhakrishnan. Microfluidics theory in practice. In *Microfluidics in Detection Science*, pages 29–60. 2014.

[22] Gian Luca Morini. Laminar-to-turbulent flow transition in microchannels. *Microscale Thermophysical Engineering*, 8(1):15–30, 2004.

[23] Ismail Tosun, Deniz Uner, and Canan Ozgen. Critical Reynolds number for Newtonian flow in rectangular ducts. *Industrial & Engineering Chemistry Research*, 27(10):1955–1957, oct 1988.

[24] Thomas Gervais and Klavs F. Jensen. Mass transport and surface reactions in microfluidic systems. *Chemical Engineering Science*, 61(4):1102–1121, 2006.

[25] Todd M Squires, Robert J Messinger, and Scott R Manalis. Making it stick: convection, reaction and diffusion in surface-based biosensors. *Nature Biotechnology*, 26(4):417–426, 2008.

[26] S. Prakash, M. Pinti, and B. Bhushan. Theory, fabrication and applications of microfluidic and nanofluidic biosensors. *Philosophical Transactions of the Royal Society A: Mathematical, Physical and Engineering Sciences*, 370(1967):2269–2303, 2012.

[27] Kwang W. Oh, Kangsun Lee, Byungwook Ahn, and Edward P. Furlani. Design of pressure-driven microfluidic networks using electric circuit analogy. *Lab Chip*, 12(3):515–545, 2012.

[28] M a Unger, H P Chou, T Thorsen, A Scherer, and S R Quake. Monolithic microfabricated valves and pumps by multilayer soft lithography. *Science (New York, N.Y.)*, 288(5463):113–6, apr 2000.

[29] Roger M Nix. Adsorption of molecules on surfaces. *http://www.chem.qmul.ac.uk/surfaces/scc/scat2.htm*.

[30] Thermo, Thermo Scientific, and Crosslinking Technical Handbook. Crosslinking technical handbook. *Ebooks*, pages 1–48, 2009.

[31] Laurence D. Barron. *Molecular Light Scattering and Optical Activity*. Cambridge University Press, Cambridge, 2004.

[32] Hyperhpysics. Circular polarization. *http://hyperphysics.phy-astr.gsu.edu/hbase/phyopt/polclas.html#c3*, June(14th), 2018.

[33] Nina Berova, Koji Nakanishi, and Robert Woody. *Circular dichroism: principles and applications*. John Wiley & Sons, 2000.

[34] N Berova, P L Polavarapu, K Nakanishi, and R W Woody. *Comprehensive Chiroptical Spectroscopy: Applications in Stereochemical Analysis of Synthetic Compounds, Natural Products, and Biomolecules*. Number v. 2 in Comprehensive Chiroptical Spectroscopy. Wiley, 2012.

[35] Gerald D Fasman. *Circular dichroism and the conformational analysis of biomolecules*. Springer Science & Business Media, 2013.

[36] Wikipedia Commons Benjah-bmm27. L-alanine aminoacid. *https://commons.wikimedia.org/wiki/File:L-alanine-3D-balls.png*.

[37] Wikipedia Commons Benjah-bmm27. Alpha-D-glucose sugar. *https://commons.wikimedia.org/wiki/File:Alpha-D-glucose-3D-balls.png*.

[38] Jynto and Wikipedia Commons Benjah-bmm27. Adenosine-monophosphate-dianion. *https://commons.wikimedia.org/wiki/File:Adenosine-monophosphate-dianion-3D-balls.png*.

[39] Wikipedia Commons Zephyris. DNA structure. *https:// commons.wikimedia.org/ wiki/ File:DNA_Structure%2BKey%2BLabelled.png*.

[40] Department of Biology. Alpha helix and Beta sheet protein structure. *Penn State University. https://www.proprofs.com/flashcards/story.php?title=chapter-5-summer-assignment*.

[41] A. J. Miles and B. A. Wallace. Circular dichroism spectroscopy of membrane proteins. *Chemical Society Reviews*, 45(18):4859–4872, 2016.

[42] Mario Hentschel, Martin Schäferling, Xiaoyang Duan, Harald Giessen, and Na Liu. Chiral plasmonics. *Science Advances*, 3(5):e1602735, may 2017.

[43] Mario Hentschel, Martin Schäferling, Bernd Metzger, and Harald Giessen. Plasmonic diastereomers: Adding up chiral centers. *Nano Letters*, 13(2):600–606, 2013.

[44] Mario Hentschel, Martin Schäferling, Thomas Weiss, Na Liu, and Harald Giessen. Three-dimensional chiral plasmonic oligomers - SI. *Nano Letters*, 12(5):2542–2547, 2012.

[45] Jatish Kumar, K. George Thomas, and Luis M. Liz-Marzán. Nanoscale chirality in metal and semiconductor nanoparticles. *Chem. Commun.*, 52(85):12555–12569, 2016.

[46] Yang Zhao, Amir N. Askarpour, Liuyang Sun, Jinwei Shi, Xiaoqin Li, and Andrea Alù. Chirality detection of enantiomers using twisted optical metamaterials. *Nature Communications*, 8:14180, 2017.

[47] Ben M. Maoz, Yulia Chaikin, Alexander B. Tesler, Omri Bar Elli, Zhiyuan Fan, Alexander O. Govorov, and Gil Markovich. Amplification of chiroptical activity of chiral biomolecules by surface plasmons. *Nano Letters*, 13(3):1203–1209, 2013.

[48] Alexander O Govorov, Zhiyuan Fan, Pedro Hernandez, Joseph M Slocik, and Rajesh R Naik. Theory of Circular Dichroism of Nanomaterials Comprising Chiral Molecules and Nanocrystals: Plasmon Enhancement, Dipole Interactions, and Dielectric Effects. *Nano Letters*, 10(4):1374–1382, apr 2010.

[49] Alexander O Govorov and Zhiyuan Fan. Theory of Chiral Plasmonic Nanostructures Comprising Metal Nanocrystals and Chiral Molecular Media. *ChemPhysChem*, 13(10):2551–2560, jul 2012.

[50] a Ramos, H Morgan, N G Green, and A Castellanos. Ac electrokinetics: a review of forces in microelectrode structures. *Journal of Physics D: Applied Physics*, 31(18):2338–2353, 1999.

[51] Justus Chukwunonso Ndukaife, Avanish Mishra, Urcan Guler, Agbai George Agwu Nnanna, Steven T. Wereley, and Alexandra Boltasseva. Photothermal heating enabled by plasmonic nanostructures for electrokinetic manipulation and sorting of particles. *ACS Nano*, 8(9):9035–9043, 2014.

[52] A. Castellanos, A. Ramos, A. González, N. G. Green, and H. Morgan. Electrohydrodynamics and dielectrophoresis in microsystems: Scaling laws. *Journal of Physics D: Applied Physics*, 36(20):2584–2597, 2003.

[53] Martin Z. Bazant, Katsuyo Thornton, and Armand Ajdari. Diffuse-charge dynamics in electrochemical systems. *Physical Review E - Statistical Physics, Plasmas, Fluids, and Related Interdisciplinary Topics*, 70(2):24, 2004.

[54] Abhijit Biswas, Ilker S. Bayer, Alexandru S. Biris, Tao Wang, Enkeleda Dervishi, and Franz Faupel. Advances in top-down and bottom-up surface nanofabrication: Techniques, applications & future prospects. *Advances in Colloid and Interface Science*, 170(1-2):2–27, 2012.

[55] George M. Whitesides. The origins and the future of microfluidics. *Nature*, 442(7101):368–373, 2006.

[56] John A. Rogers and Ralph G. Nuzzo. Recent progress in soft lithography. *Materials Today*, 8(2):50–56, 2005.

[57] J. Cooper McDonald, David C Duffy, Janelle R Anderson, Daniel T Chiu, Hongkai Wu, Olivier J. A. Schueller, and George M. Whitesides. Fabrication of microfluidic systems in poly(dimethylsiloxane). *Electrophoresis*, 21(1):27–40, jan 2000.

[58] J C Love and Et Al. *Self-Assembled Monolayers of Thiolates on Methals as a Form of Nanotechnology*, volume 4. 2005.

[59] Jochen R. Brandt, Francesco Salerno, and Matthew J. Fuchter. The added value of small-molecule chirality in technological applications. *Nature Reviews Chemistry*, 1(6):0045, jun 2017.

[60] Theodore J. Leitereg, Dante G. Guadagni, Jean Harris, Thomas R. Mon, and Roy Teranishi. Chemical and Sensory Data Supporting the Difference between the Odors of the Enantiomeric Carvones. *Journal of Agricultural and Food Chemistry*, 19(4):785–787, 1971.

[61] Ronald Bentley. *Reviews in Cell Biology and Molecular Medicine*. Wiley-VCH Verlag GmbH & Co. KGaA, Weinheim, Germany, sep 2006.

[62] Naveen Chhabra, MadanL Aseri, and Deepak Padmanabhan. A review of drug isomerism and its significance. *International Journal of Applied and Basic Medical Research*, 3(1):16, 2013.

[63] T. H. Maugh. Catalysts That Break Nature's Monopoly: Chiral complexes can approach the specificity of enzymes for synthesis of optically active compounds, and can act on a wider variety of substrates. *Science*, 221(4608):351–354, jul 1983.

[64] Srdjan S. Aćimović, Maria a. Ortega, Vanesa Sanz, Johann Berthelot, Jose L. Garcia-Cordero, Jan Renger, Sebastian J. Maerkl, Mark P. Kreuzer, and Romain Quidant. LSPR Chip for Parallel, Rapid, and Sensitive Detection of Cancer Markers in Serum. *Nano Letters*, 14(5):2636–2641, may 2014.

[65] Ozlem Yavas, Mikael Svedendahl, Paulina Dobosz, Vanesa Sanz, and Romain Quidant. On-a-chip Biosensing Based on All-Dielectric Nanoresonators. *Nano Letters*, 17(7):4421–4426, jul 2017.

[66] a V Kabashin, P Evans, S Pastkovsky, W Hendren, G a Wurtz, R Atkinson, R Pollard, V a Podolskiy, and a V Zayats. Plasmonic nanorod metamaterials for biosensing. *Nature materials*, 8(11):867–71, nov 2009.

[67] Mikael Svedendahl, Ruggero Verre, and Mikael Käll. Refractometric biosensing based on optical phase flips in sparse and short-range-ordered nanoplasmonic layers. *Light: Science & Applications*, 3(11):e220, nov 2014.

[68] V. G. Kravets, F. Schedin, R. Jalil, L. Britnell, R. V. Gorbachev, D. Ansell, B. Thackray, K. S. Novoselov, a. K. Geim, a. V. Kabashin, and a. N. Grigorenko. Singular phase nano-optics in plasmonic metamaterials for label-free single-molecule detection. *Nature Materials*, 12(2):1–6, jan 2013.

[69] Peter Zijlstra, Pedro M. R. Paulo, and Michel Orrit. Optical detection of single non-absorbing molecules using the surface plasmon resonance of a gold nanorod. *Nature Nanotechnology*, 7(6):379–382, 2012.

[70] Si Chen, Mikael Svedendahl, Richard P. Van Duyne, and Mikael Käll. Plasmon-Enhanced Colorimetric ELISA with Single Molecule Sensitivity. *Nano Letters*, 11(4):1826–1830, apr 2011.

[71] Robin Ogier, Yurui Fang, Mikael Svedendahl, Peter Johansson, and Mikael Käll. Macroscopic Layers of Chiral Plasmonic Nanoparticle Oligomers from Colloidal Lithography. *ACS Photonics*, 1(10):1074–1081, oct 2014.

[72] Robin Ogier, Yurui Fang, Mikael Käll, and Mikael Svedendahl. Near-Complete Photon Spin Selectivity in a Metasurface of Anisotropic Plasmonic Antennas. *Physical Review X*, 5(4):041019, 2015.

[73] Mario Hentschel, Martin Schäferling, Thomas Weiss, Na Liu, and Harald Giessen. Three-dimensional chiral plasmonic oligomers. *Nano Letters*, 12(5):2542–2547, 2012.

[74] Ruggero Verre, Lei Shao, Nils Odebo Länk, Pawel Karpinski, Andrew B. Yankovich, Tomasz J. Antosiewicz, Eva Olsson, and Mikael Käll. Metasurfaces and Colloidal Suspensions Composed of 3D Chiral Si Nanoresonators. *Advanced Materials*, 29(29):1–6, 2017.

[75] Makoto Kuwata-Gonokami, Nobuyoshi Saito, Yusuke Ino, Martti Kauranen, Konstantins Jefimovs, Tuomas Vallius, Jari Turunen, and Yuri Svirko. Giant optical activity in quasi-two-dimensional planar nanostructures. *Physical review letters*, 95(22):227401, 2005.

[76] A S Schwanecke, A Krasavin, D M Bagnall, A Potts, A V Zayats, and N I Zheludev. Broken Time Reversal of Light Interaction with Planar Chiral Nanostructures. (December):1–4, 2003.

[77] Nanfang Yu, Francesco Aieta, Patrice Genevet, Mikhail a. Kats, Zeno Gaburro, and Federico Capasso. A broadband, background-free quarter-wave plate based on plasmonic metasurfaces. *Nano Letters*, 12(12):6328–6333, 2012.

[78] Y. Zhao, M.A. Belkin, and A. Alù. Twisted optical metamaterials for planarized ultrathin broadband circular polarizers. *Nature Communications*, 3(1):870, jan 2012.

[79] Yiqiao Tang and Adam E. Cohen. Enhanced enantioselectivity in excitation of chiral molecules by superchiral light. *Science*, 332(6027):333–336, 2011.

[80] Yiqiao Tang and Adam E Cohen. Optical Chirality and Its Interaction with Matter. *Physical Review Letters*, 104(16):163901, apr 2010.

[81] Daniel M Lipkin. Existence of a New Conservation Law in Electromagnetic Theory. *Journal of Mathematical Physics*, 5(5):696–700, may 1964.

[82] Nina Meinzer, Euan Hendry, and William L. Barnes. Probing the chiral nature of electromagnetic fields surrounding plasmonic nanostructures. *Physical Review B - Condensed Matter and Materials Physics*, 88(4):1–5, 2013.

[83] Ben M. Maoz, Yulia Chaikin, Alexander B. Tesler, Omri Bar Elli, Zhiyuan Fan, Alexander O. Govorov, and Gil Markovich. Amplification of chiroptical activity of chiral biomolecules by surface plasmons. *Nano Letters*, 13(3):1203–1209, 2013.

[84] Seojoo Lee, Seokjae Yoo, and Q-Han Park. Microscopic Origin of Surface-Enhanced Circular Dichroism. *ACS Photonics*, 4(8):2047–2052, aug 2017.

[85] M Schäferling, Xinghui Yin, and Harald Giessen. Formation of chiral fields in a symmetric environment. *Optics express*, 20(24):26326–26336, 2012.

[86] Martin Schäferling, Daniel Dregely, Mario Hentschel, and Harald Giessen. Tailoring Enhanced Optical Chirality: Design Principles for Chiral Plasmonic Nanostructures. *Physical Review X*, 2(3):031010, aug 2012.

[87] Aitzol García-Etxarri and Jennifer a. Dionne. Surface-enhanced circular dichroism spectroscopy mediated by nonchiral nanoantennas. *Physical Review B*, 87(23):235409, jun 2013.

[88] Chi-sing Ho, Aitzol Garcia-Etxarri, Yang Zhao, and Jennifer Dionne. Enhancing Enantioselective Absorption Using Dielectric Nanospheres. *ACS Photonics*, 4(2):197–203, feb 2017.

[89] Lisa V. Poulikakos, Philipp Gutsche, Kevin M. McPeak, Sven Burger, Jens Niegemann, Christian Hafner, and David J. Norris. Optical Chirality Flux as a Useful Far-Field Probe of Chiral Near Fields. *ACS Photonics*, 3(9):1619–1625, 2016.

[90] E Hendry, T Carpy, J Johnston, M Popland, R V Mikhaylovskiy, a J Lapthorn, S M Kelly, L D Barron, N Gadegaard, and M Kadodwala. plasmons offer a helping hand. *Nature nanotechnology*, 5(11):783–787, nov 2010.

[91] Nadia a. Abdulrahman, Z. Fan, Taishi Tonooka, Sharon M. Kelly, Nikolaj Gadegaard, Euan Hendry, Alexander O. Govorov, and Malcolm Kadodwala. Induced Chirality through Electromagnetic Coupling between Chiral Molecular Layers and Plasmonic Nanostructures. *Nano Letters*, 12(2):977–983, feb 2012.

[92] Fang Lu, Ye Tian, Mingzhao Liu, Dong Su, Hui Zhang, Alexander O. Govorov, and Oleg Gang. Discrete nanocubes as plasmonic reporters of molecular chirality. *Nano Letters*, 13(7):3145–3151, jul 2013.

[93] Rong Yao Wang, Peng Wang, Yineng Liu, Wenjing Zhao, Dawei Zhai, Xuhai Hong, Yinglu Ji, Xiaochun Wu, Feng Wang, Duan Zhang, Wensheng Zhang, Ruibin Liu, and Xiangdong Zhang. Experimental observation of giant chiroptical amplification of small chiral molecules by gold nanosphere clusters. *Journal of Physical Chemistry C*, 118(18):9690–9695, 2014.

[94] Martin Schäferling. *Chirality Nanophotonics*, volume 205. 2017.

[95] Hagen Klauk. *Organic electronics: materials, manufacturing, and applications*. John Wiley & Sons, 2006.

[96] Jun Ichi Takahashi, Hiroyuki Shinojima, Michiko Seyama, Yuko Ueno, Takeo Kaneko, Kensei Kobayashi, Hajime Mita, Mashahiro Adachi, Masahito Hosaka, and Masahiro Katoh. Chirality emergence in thin solid films of amino acids by polarized light from synchrotron radiation and free electron laser. *International Journal of Molecular Sciences*, 10(7):3044–3064, 2009.

[97] Eman S. Zarie, Viktor Kaidas, Dawit Gedamu, Yogendra K. Mishra, Rainer Adelung, Franz H. Furkert, Regina Scherließ, Hartwig Steckel, and Birte Groessner-Schreiber. Solvent free fabrication of micro and nanostructured drug coatings by thermal evaporation for controlled release and increased effects. *PLoS ONE*, 7(8), 2012.

[98] Yiqiao Tang and Adam E Cohen. Optical Chirality and Its Interaction with Matter. *Physical Review Letters*, 104(16):163901, apr 2010.

[99] Joseph M. Slocik, Alexander O. Govorov, and Rajesh R. Naik. Plasmonic circular dichroism of peptide-functionalized gold nanoparticles. *Nano Letters*, 11(2):701–705, 2011.

[100] Yiqiao Tang and Adam E Cohen. Enhanced Enantioselectivity in Excitation of Chiral Molecules by Superchiral light. 333(2011):332–336, 2014.

[101] Makoto Kuwata-gonokami, Nobuyoshi Saito, Yusuke Ino, Martti Kauranen, Konstantins Jefimovs, Tuomas Vallius, Jari Turunen, and Yuri Svirko. Giant Optical Activity in Quasi-Two-Dimensional Planar Nanostructures. 227401(November):1–4, 2005.

[102] K Konishi, T Sugimoto, B Bai, and Y Svirko. Effect of surface plasmon resonance on the optical activity of chiral metal nanogratings. 15(15):9575–9583, 2007.

[103] M. D. Malinsky, K. L. Kelly, G. C. Schatz, and R. P. Van Duyne. Chain length dependence and sensing capabilities of the localized surface plasmon resonance of silver nanoparticles chemically modified with alkanethiol self-assembled monolayers. *Journal of the American Chemical Society*, 123(7):1471–1482, 2001.

[104] PubChem. Cysteine. *Open chemistry database. Accesed on June 2018.https://pubchem.ncbi.nlm.nih.gov/compound/L-cysteine*.

[105] NCIt. Cysteine. *National Cancer Institute, Accesed on June 2018. https:// ncit.nci.nih.gov/ ncitbrowser/ ConceptReport.jsp?dictionary=NCI_Thesaurus&ns=NCI_Thesaurus&code=C29609*.

[106] HMDB. L-Cysteine. *Human Metabolome Database, Accesed on June 2018. http://www.hmdb.ca/metabolites/HMDB0000574*.

[107] PubChem. D-Cysteine. *Open chemistry database. Accesed on June 2018. https://pubchem.ncbi.nlm.nih.gov/compound/D-cysteine*.

[108] HMDB. D-Cysteine. *Human Metabolome Database, Accesed on June 2018. http://www.hmdb.ca/metabolites/HMDB0003417*.

[109] Michelle Duval Malinsky, K. Lance Kelly, George C. Schatz, and Richard P. Van Duyne. Nanosphere Lithography: Effect of Substrate on the Localized Surface Plasmon Resonance Spectrum of Silver Nanoparticles. *The Journal of Physical Chemistry B*, 105(12):2343–2350, 2001.

[110] Srdjan S Acimovic. Localized surface plasmon resonance for biosensing lab-on-a-chip applications. 2012.

[111] PubChem. Glutamic acid. *Open chemistry database. Accesed on June 2018.https://pubchem.ncbi.nlm.nih.gov/compound/L-glutamic_acid*.

[112] MeSH. Glutamic acid. *National Center for biotechnology Information. Accesed on June 2018.https://www.ncbi.nlm.nih.gov/mesh/68018698*.

[113] HMDB. L-Glutamic acid. *Human Metabolome Databas. Accesed on June 2018.http://www.hmdb.ca/metabolites/HMDB0000148*.

[114] PubChem. D-Glutamic acid. *Open chemistry database. Accesed on June 2018.https:https://pubchem.ncbi.nlm.nih.gov/compound/D-glutamic_acid*.

[115] HMDB. D-Glutamic acid. *Human Metabolome Databas. Accesed on June 2018.http://www.hmdb.ca/metabolites/HMDB0003339*.

[116] Ekmel Ozbay. Plasmonics: Merging Photonics and Electronics at Nanoscale Dimensions. *Science*, 311(5758):189–193, jan 2006.

[117] Mengtao Sun and Hongxing Xu. A novel application of plasmonics: Plasmon-driven surface-catalyzed reactions. *Small*, 8(18):2777–2786, 2012.

[118] Jon A. Schuller, Edward S. Barnard, Wenshan Cai, Young Chul Jun, Justin S. White, and Mark L. Brongersma. Plasmonics for extreme light concentration and manipulation. *Nature Materials*, 9(3):193–204, 2010.

[119] Nikolay I. Zheludev and Yuri S. Kivshar. From metamaterials to metadevices. *Nature Materials*, 11(11):917–924, 2012.

[120] Matthew A. Cooper. Optical biosensors in drug discovery. *Nature Reviews Drug Discovery*, 1(7):515–528, 2002.

[121] Anders Kristensen, Joel K.W. Yang, Sergey I. Bozhevolnyi, Stephan Link, Peter Nordlander, Naomi J. Halas, and N. Asger Mortensen. Plasmonic colour generation. *Nature Reviews Materials*, 2(1), 2016.

[122] S. Chen, M. Svedendahl, M. Käll, L. Gunnarsson, and A. Dmitriev. Ultra-high sensitivity made simple: Nanoplasmonic label-free biosensing with an extremely low limit-of-detection for bacterial and cancer diagnostics. *Nanotechnology*, 20(43), 2009.

[123] Martin D. Baaske, Matthew R. Foreman, and Frank Vollmer. Single-molecule nucleic acid interactions monitored on a label-free microcavity biosensor platform. *Nature Nanotechnology*, 9(11):933–939, 2014.

[124] Eugene Kim, Martin D. Baaske, Isabel Schuldes, Peter S. Wilsch, and Frank Vollmer. Label-free optical detection of single enzyme-reactant reactions and associated conformational changes. *Science Advances*, 3(3), 2017.

[125] Todd Thorsen, Sebastian J. Maerkl, and Stephen R. Quake. Microfluidic large-scale integration. *Science*, 298(5593):580–584, 2002.

[126] Demetri Psaltis, Stephen R. Quake, and Changhuei Yang. Developing optofluidic technology through the fusion of microfluidics and optics. *Nature*, 442(7101):381–6, jul 2006.

[127] Giorgio Volpe, Monika Noack, Srdjan S. Aćimović, Carsten Reinhardt, and Romain Quidant. Near-field mapping of plasmonic antennas by multiphoton absorption in poly(methyl methacrylate). *Nano Letters*, 12(9):4864–4868, 2012.

[128] Srdjan S. Acimovic, Hana Šípová, Gustav Emilsson, Andreas B. Dahlin, Tomasz J. Antosiewicz, and Mikael Käll. Superior LSPR substrates based on electromagnetic decoupling for on-a-chip high-throughput label-free biosensing. *Light: Science and Applications*, 6(8):1–8, 2017.

[129] A. Hatch, E. Garcia, and P. Yager. Diffusion-Based Analysis of Molecular Interactions in Microfluidic Devices. *Proceedings of the IEEE*, 92(1):126–139, 2004.

[130] Paul E. Sheehan and Lloyd J. Whitman. Detection limits for nanoscale biosensors. *Nano Letters*, 5(4):803–807, 2005.

[131] Jon S. Donner, Guillaume Baffou, David McCloskey, and Romain Quidant. Plasmon-assisted optofluidics. *ACS Nano*, 5(7):5457–5462, 2011.

[132] Brian J. Roxworthy, Abdul M. Bhuiya, Surya P. Vanka, and Kimani C. Toussaint. Understanding and controlling plasmon-induced convection. *Nature Communications*, 5:1–8, 2014.

[133] A. V. Delgado, F. González-Caballero, R. J. Hunter, L. K. Koopal, and J. Lyklema. Measurement and interpretation of electrokinetic phenomena. *Journal of Colloid and Interface Science*, 309(2):194–224, 2007.

[134] Chih Chang Chang and Ruey Jen Yang. Electrokinetic mixing in microfluidic systems. *Microfluidics and Nanofluidics*, 3(5):501–525, 2007.

[135] Martin Z. Bazant and Todd M. Squires. Induced-Charge Electrokinetic Phenomena: Theory and Microfluidic Applications. *Physical Review Letters*, 92(6):1–4, 2004.

[136] Wee Yang Ng, Shireen Goh, Yee Cheong Lam, Chun Yang, and Isabel Rodríguez. DC-biased AC-electroosmotic and AC-electrothermal flow mixing in microchannels. *Lab Chip*, 9(6):802–809, 2009.

[137] Justus C. Ndukaife, Alexander V. Kildishev, Agbai George Agwu Nnanna, Vladimir M. Shalaev, Steven T. Wereley, and Alexandra Boltasseva. Long-range and rapid transport of individual nano-objects by a hybrid electrothermoplasmonic nanotweezer. *Nature Nanotechnology*, 11(1):53–59, nov 2015.

[138] Maurizio Righini, A. Zelenina, and Romain Quidant. Parallel and selective trapping in a patterned plasmonic landscape. *2007 IEEE/LEOS International Conference on Optical MEMS and Nanophotonics, OMENS*, pages 61–62, 2007.

[139] H. M K Wong, M. Righini, J. C. Gates, P. G R Smith, V. Pruneri, and R. Quidant. On-a-chip surface plasmon tweezers. *Applied Physics Letters*, 99(6):10–13, 2011.

[140] J. Berthelot, S. S. Aćimović, M. L. Juan, M. P. Kreuzer, J. Renger, and R. Quidant. Three-dimensional manipulation with scanning near-field optical nanotweezers. *Nature Nanotechnology*, 9(4):295–299, 2014.

[141] Dong Qin, Younan Xia, and George M. Whitesides. Soft lithography for micro- and nanoscale patterning. *Nature Protocols*, 5(3):491–502, 2010.

[142] Guillaume Baffou, Romain Quidant, and F. Javier García De Abajo. Nanoscale control of optical heating in complex plasmonic systems. *ACS Nano*, 4(2):709–716, 2010.

[143] J. C. Ndukaife, V. M. Shalaev, and A. Boltasseva. Plasmonics–turning loss into gain. *Science*, 351(6271):334–335, 2016.

[144] J Crocker and D Grier. Methods of Digital Video Microscopy for Colloidal Studies. *Journal of Colloid and Interface Science*, 179(1):298–310, 1996.

[145] P B Johnson and R W Christy. Optical Constants of the Noble Metals. *Physical Review B*, 1318(1970), 1972.

[146] Phenylalanine index of refraction. https:// comptox.epa.gov/ dashboard/ DTXSID9023463Phenylalanie Index of refraction. *Accesed on June 2018*.

[147] Maxim L Nesterov, Xinghui Yin, Martin Schäferling, Harald Giessen, and Thomas Weiss. The role of plasmon-generated near-fields for enhanced circular dichroism spectroscopy Supporting information. *Nano Letters*, pages 1–9, 2013.

Appendix A

Chiro-plasmonic sensor parameters and modeling

A.1 Racemic gammadion sensor

The sensor design consists on mirrored gammadion organized in alternated positions in a squared matrix. The unit cell consists of 4 gammadions spaced 350*nm* and the unit cells were spaced 700*nm*. Total matrix extension is 120*um*. The gammadion overall size is 275*nm* and the arms width is 75*nm*. Figure A.1 show a layout of the gammadion matrix design.

A.2 Simulations

The gammadions were modelled having the side length of 275*nm*, with arm widths of 75*nm*, and a height of 50*nm*. The corners and edges of the gammadion were significantly rounded in order to avoid edge effects. The gold permittivity was taken

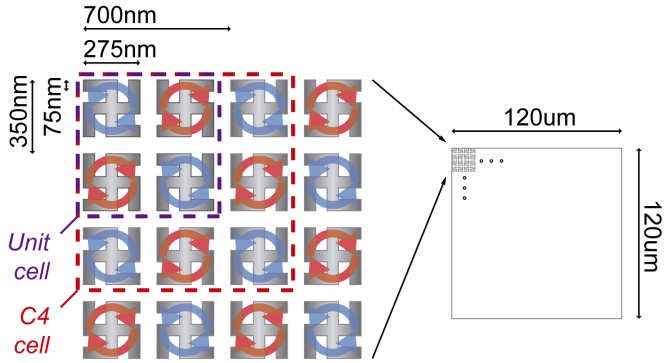

Fig. A.1 Gammadion matrix design of the fabricated sensors. The unit and C4 cell (highlighted in the layout) are showing $C4$ the symmetry of the matrix.

from experimental data[145]. The substrate refractive index was set to $n_s = 1.5$, the ambient $n_a = 1.0$ and the molecular coating $n_c = 1.6$[146].

Chiral media can be modelled as:

$$\begin{cases} \mathbf{D} = \varepsilon_0 \varepsilon_r \mathbf{E} + i\kappa \mathbf{H} \\ \mathbf{B} = \frac{\mathbf{H}}{\mu} + i\kappa \mathbf{E}, \end{cases} \tag{A.1}$$

where $\mathbf{D}$ is the electric displacement field, $\mathbf{E}$ is the electric field, ε_0 and ε_r are the vacuum and relative permittivites, respectively, κ is the chiral parameter, μ is the permeability $\mathbf{H}$ is the magnetic field and $\mathbf{B}$ is the magnetic flux density. The real and imaginary parts of κ are linked to ORD and CD, respectively. The chiral parameter is typically wavelength dependent, with the maximum response in the UV spectral range. In the visible, however, κ is weak and varies slowly with the wavelength. Therefore, we modelled the coating with a constant κ over the simulated wavelengths, typically with values $\kappa = \pm(5 + 0.05i) \cdot 10^{-5}$,as the real part of κ is expected to be about two orders of magnitude larger than the imaginary part in the visible spectral range, given a resonance in the UV[147]. Following Nesterov et al[147], we then calculated the CD of the chiral coating with and without the plasmonic nanostructures, with the ratio defining the CD enhancement. For a thick layer, the average enhancement is ~ 180 as illustrated in Fig. 3.7 of the main text.

However not all molecules contribute equally, since molecules far from the sensors are unaffected by the inclusion of the nanostructures. As an example, the molecules in the gaps of the gammadion arms can be enhanced more, about 1000 times, and the molecules in these regions contribute with $1/3$ of the total CD for a thick ($150nm$) coating. Another $1/3$ of the signal stem from molecules in the near vicinity ($\sim 10nm$) of the gold - on top or next to the nanostructures, while 90% of the total CD signals are retrieved from a 30 nm layer, see Fig.A.2.

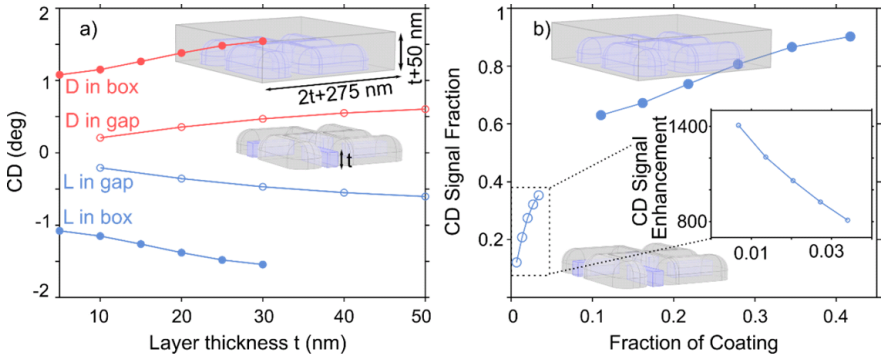

Fig. A.2 CD signals from chiral media in specific locations on the sensors. a) The CD signals from D and L molecules in the gaps and in the near surrounding of the gammadions calculated at $765nm$. b) The CD signal fractions from the locations in a) normalized to the signal from a $150nm$ thick layer of molecules.

Acknowledge

I want to acknowledge for the numerical simulations presented in this appendix to Mikael Svedendahl.

Appendix B

Electrothermoplasmonics characterization and modeling

B.1 ETP flow demonstration frames

ETP flows were recorded by using $5\mu m$ silica beads as tracers in static and flow conditions at a frame rate of $14Hz$ (see figure B.1 frames, left-top). The video sequences were first background subtracted by means of a temporal median filter to enhance the particle visibility. Then, in order to highlight individual bead trajectories, a temporal minimum projection was performed over a sliding window of either 15 or 10 consecutive frames, for static and flow conditions respectively (figure B.1 frames, right-top). In the static flow video the beads exhibit quasi-linear trajectories toward the center of the plasmonic structure. Whereas, for the external flow condition, the beads approach the plasmonic structure with straight trajectories, then bend towards the center of the structure and finally are pushed up and forward along a narrower straight line.

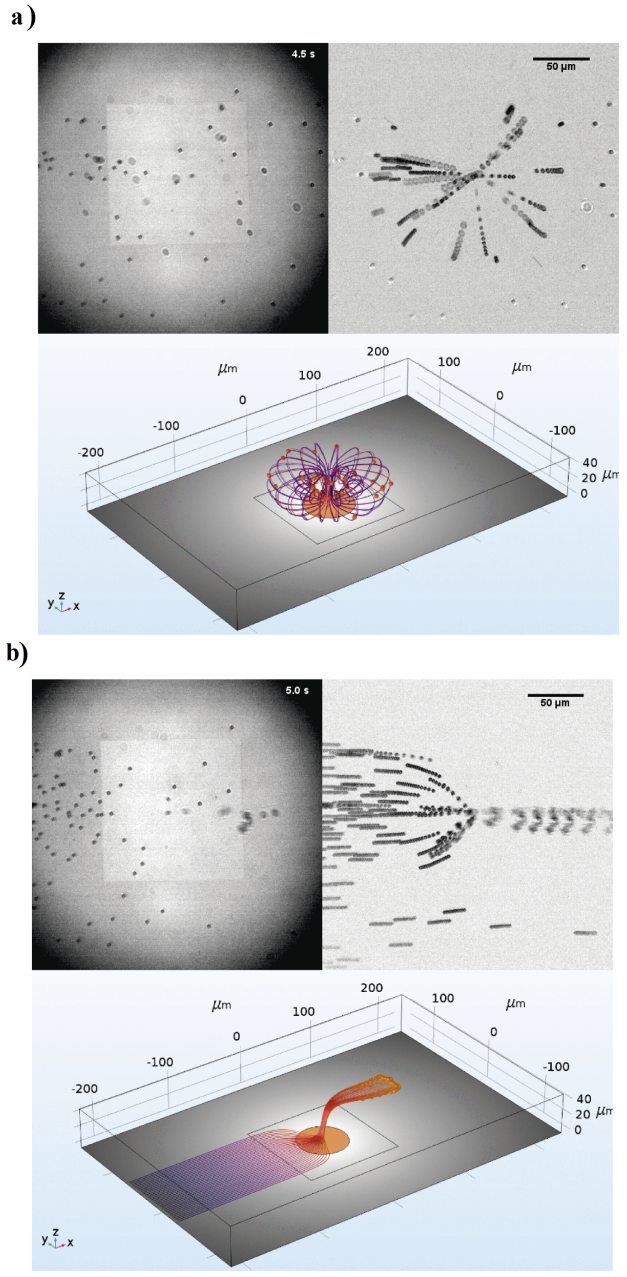

Fig. B.1 Frames of demonstration videos for static (a) and flow (b) cases, respectively. For every case, on the left-top the real acquisition image is presented and on the right-top the treated image. The bottom corresponds to an animation of the numerical simulations.

B.2 Numerical modeling parameters

In the following table we show the physical and geometrical parameters used in the generation of the numerical simulations.

Name	Expression	Value	Description
R_{ext}	$10(\mu m)$	$1 \cdot 10^5\ m$	Exterior simulation domain radius
h_{ext}	$10(\mu m)$	$1 \cdot 10^5\ m$	Exterior upper simulation domain height
l_{plasm}	$160(nm)$	$1.6 \cdot 10^7\ m$	Plasmonic nanostructure length
w_{plasm}	$75(nm)$	$7.5 \cdot 10^8\ m$	Plasmonic nanostructure width
h_{plasm}	$65(nm)$	$6.5 \cdot 10^8\ m$	Plasmonic nanostructure height
$period_{array}$	$400(nm)$	$4 \cdot 10^7\ m$	Array period
l_{array}	$120(\mu m)$	$1.2 \cdot 10^4\ m$	Array length
w_{array}	$120(\mu m)$	$1.2 \cdot 10^4\ m$	Array width
$N_{l_{array}}$	$l_{array}/period_{array}$	300	Number of nanostructures length
$N_{w_{array}}$	$w_{array}/period_{array}$	300	Number of nanostructures width
P_{laser}	$30(mW)$	$0.03\ W$	Laser power
R_{laser}	$30(\mu m)$	$3 \cdot 10^5\ m$	Laser beam radius
SD_{laser}	$15(\mu m)$	$1.5 \cdot 10^5\ m$	Standard deviation laser beam
A_{laser}	$pi * R_{laser}^2$	$2.8274 \cdot 10^9\ m^2$	Laser section
$l_{channel}$	$15(mm)$	$0.015\ m$	Channel length
$factor$	15	15	Geometry size factor
$l_{sim_{channel}}$	$factor * R_{laser}$	$4.5 \cdot 10^4\ m$	Simulated channel length

$w_{channel}$	$290(\mu m)$	$2.9 \cdot 10^4\ m$	Channel width
$h_{channel}$	$50(\mu m)$	$5 \cdot 10^5\ m$	Channel height
h_{Au}	$75(nm)$	$7.5 \cdot 10^8\ m$	Au layer thickness
h_{Ti}	$2(nm)$	$2 \cdot 10^9\ m$	Titanium layer thickness
h_{ITO}	$100(nm)$	$1 \cdot 10^7\ m$	ITO layer thickness
h_{glass}	$1.1(mm)$	$0.0011\ m$	Glass thickness
$A_{channel}$	$w_{channel} * h_{channel}$	$1.45 \cdot 10^8\ m^2$	Channel section area
$discharge$	$18 \cdot 10^3(mm^3/s)$	$1.8 \cdot 10^{11}\ m^3/s$	Discharge
Avg_{vel}	$discharge/A_{channel}$	$0.0012414\ m/s$	Average inlet velocity
T_0	$20(degC)$	$293.15\ K$	Initial temperature
$deltaT_{array_{peak}}$	$5(K]$	$5\ K$	Array temperature
$freqEac$	$100(kHz)$	$1E5\ Hz$	Applied AC electric field frequency
$omegaEac$	$2 * pi * freqEac/[rad/s]$	$628318 rad/s$	Applied AC electric field angular frequency
V_{peak}	$75(V]/2$	$37.5\ V$	Electric potential peak value
E_{ac}	$V_{peak}/h_{channel}$	$7.5E5\ V/m$	Electric ac field peak value
$beta$	$207 \cdot 10^6(K^-1)$	$2.07 \cdot 10^4\ 1/K$	Thermal expansion coefficient of water at 20 ºC
$alpha$	$-0.004(K^-1)$	$-0.004\ 1/K$	Permittivity Temperature Coefficient
$gamma$	$0.02(K^-1)$	$0.02\ 1/K$	Conductivity Temperature Coefficient
$tvid$	$0.1(s)$	$0.1\ s$	Animation time
rho_{part}	$2.2(g/cm^3)$	$2200\ kg/m^3$	Density of silica tracking particles
rad_{part}	$2.5(\mu m)$	$2.5 \cdot 10^6\ m$	Radius of silica tracking particles

vol_{part}	$4 * pi * rad_{part}^3/3$	$6.545 \cdot 10^{17}\ m^3$	Volume of silica tracking particles
$mass_{part}$	$rho_{part} * vol_{part}$	$1.4399 \cdot 10^{13}\ kg$	Mass of silica tracking particles
$grav_{part}$	$rho_{part} * vol_{part} * g_{const}$	$1.4121 \cdot 10^{12}\ N$	Weight of silica tracking particles
$Reynolds$	4*comp1.mat1. def.rho(T_0[1/K]) *discharge[kg/m^3] /(2*comp1. mat1.def. eta(T_0[1/K])[Pa*s] *($h_{channel}$ +$w_{channel}$))	0.10486	Channel Reynolds number

Table B.1 Modeling paremeters used in numerical simulations.

Acknowledge

I want to acknowledge for the material presented in this appendix; to Judith Medina for recording the videos, to Jaime Ortega for processing the videos to give the frames a dynamic view and to Emilio Ruiz-Reina for the numerical simulations of the ETP effect.